The University Of Sheffield.

Experimental and numerical techniques for characterising catheter-induced blood vessel damage: towards tools for improvement of intravascular catheter design

By:
Christopher Noble

A thesis submitted in partial fulfilment of the requirements for the degree of Doctor of Philosophy

The University of Sheffield
Faculty of Engineering
Department of Mechanical Engineering

Submission Date

November 2016

Experimental and numerical techniques for characterising catheter-induced blood vessel damage: towards tools for improvement of intravascular catheter design

Christopher Noble

Abstract

Cardiovascular diseases are a significant health risk worldwide, being the largest contributor to deaths in most developed and developing countries. For physical testing of new medical devices, diseased tissue specimens are desirable. However, these are difficult to obtain in quantity. The first phase of the work therefore focused on emulating effects of disease on artery mechanical response, using enzyme and chemical treatment of healthy tissue. Porcine aorta was partially digested by elastase and collagenase treatments to remove constituent proteins, and exposed to low concentration glutaraldehdye to partially cross-link proteins. Uniaxial tension testing and controlled peel testing were then performed in the artery axial and circumferential directions to assess the changes in mechanical and failure behaviour. The treatments successfully altered the wall tensile and peeling response with effects varying by the loading type and direction. Multiphoton microscopy was also performed to allow visualisation of the changes to fibre structure and density. Finally, tensile test results were fitted to the Gasser-Ogden-Holzapfel constitutive model and a continuum damage model, and the fitted curves were best matched with the circumferential direction results. The latter phase of the work focused on development of methods for characterising and simulating catheter-induced dissection processes. An experimental procedure was developed, wherein a catheter was forced between layers of arterial media, propagating a dissection, while reaction force was measured. The various approaches utilised to model this process within FEA are presented and the subsequent difficulties explored. The inherent complexity of the process being modelled resulted in difficulty drawing out the underlying problems. To rectify this, the experiment was simplified such that a metal wedge with a rounded front was used to dissect the tissue. This was successfully modelled and insights from this were considered with regard to numerical difficulties in the catheter dissection model.

Dedications

There are many people who without their help, support and guidance, this would not have been possible.

Firstly I would like to thank my primary supervisor Dr. Zeike Taylor for his consistent support and assistance. His knowledge, guidance and patience allowed me to foster independence as a researcher whilst helping my progress, keeping things moving when obstacles arose. I would also like to thank my secondary supervisor Prof. Roger Lewis who provided additional support, guidance and an extra set of eyes for catching my mistakes.

I am grateful to all members of the UNITISS project I collaborated with and all members of Philips Research Eindhoven who aided with my research and made my stay memorable. I am particularly thankful to Prof. Steve Franklin, Dr. Ruud Voncken and Dr. Olaf van der Sluis for helping me get settled and their help even after my secondment had ended.

For access to their laboratories, equipment and knowledge, I would also like to thank Prof. Sheila MacNeil and Dr. Nicola Green.

CISTIB was an excellent place to conduct my research, providing a warm and welcoming environment. Special thanks to Edward Cramphorn and Nishant Ravikumar whose friendship over the past 8 years has has helped me through the struggles of both my undergraduate and PhD studies, providing a helping hand and welcomed distractions.

Finally I would like to thank my wife Katie to whom my gratitude is beyond words, and my family for their encouragement, support and always being there when needed.

Acknowledgements

This work was supported by the Engineering and Physical Sciences Research Council (Doctoral Training Grant) and the European Commission Framework Programme 7, Understanding Interactions of Human Tissue with Medical Devices (UNITISS, FP7-PEOPLE-2011-IAPP/286174).

This content of this thesis was partially adapted from the following publications with all necessary permissions acquired:

1. C. Noble, N. Smulders, N. H. Green, R. Lewis, M. J. Carré, S. E. Franklin, S. MacNeil, and Z. A. Taylor, "Creating a model of diseased artery damage and failure from healthy porcine aorta," J. Mech. Behav. Biomed. Mater., vol. 60, pp. 378–393, Jul. 2016.

2. C. Noble, N. Smulders, R. Lewis, M. J. Carré, S. E. Franklin, S. MacNeil, and Z. A. Taylor, "Controlled peel testing of a model tissue for diseased aorta," J. Biomech., vol. 49, no. 15, pp. 3667–3675, Nov. 2016.

3. C. Noble, O. van der Sluis, R. Voncken, O. Burke, S. E. Franklin, R. Lewis, Z. A. Taylor, "Simulation of arterial dissection by a penetrating external body using cohesive zone modelling," J. Mech. Behav. Biomed. Mater., Submitted

Contents

List of Figures

List of Tables

List of Symbols

Ω_0	Model domain in the initial configuration
Ω	Model domain in the current configuration
$\mathbf{X}$	The coordinate of a material point in Ω_0 (m)
$\mathbf{x}$	The coordinate of a material point in Ω (m)
χ	The motion mapping $\mathbf{X}$ to $\mathbf{x}$ (m)
$\mathbf{F}$	Deformation gradient
J	Jacobian or volume ratio
Ψ	Strain energy density function ($\mathrm{J/m^3}$)
$\mathbf{C}$	Right Cauchy-Green deformation tensor
$\mathbf{I}$	2nd order identity tensor
$\mathbf{H}_i$	General structural tensor for fibre family i
μ	Shear modulus (kPa)
$\lambda_1, \lambda_2, \lambda_3$	Full principal stretches
E_i	Strain in the direction of mean fibre orientation for fibre family i
θ	Mean collagen fibre angle ($^\circ$)
$\mathbf{a}_i$	Unit vector describing mean collagen fibre orientation for fibre family i
κ	Statistical parameter describing the degree of collagen fibre dispersion
k_1	Stress like parameter within GOH model (kPa)
k_2	GOH model fibre material parameter
$\sigma_1, \sigma_2, \sigma_3$	Principal Cauchy stresses (MPa)
p	Lagrange multiplier
D^k	Reduction factor
Ξ_t^k	Damage criterion ($\mathrm{J^{1/2}m^{-3/2}}$)
Ξ_{min}^k	Damage initiation parameter ($\mathrm{J^{1/2}m^{-3/2}}$)
Ξ_{max}^k	Damage completion parameter ($\mathrm{J^{1/2}m^{-3/2}}$)
β^k	Damage profile control parameter
f	Measured uniaxial tensile reaction force
T	Dog-bone sample thickness (mm)
W	Dog-bone sample width (mm)
$\mathbf{x}$	Vector of model parameters
w_1, w_2	Optimisation procedure weighting parameters
$\sigma_1^{\exp}$	Experimentally measured first principal Cauchy stress (MPa)

σ_1^{mod}	Model-predicted first principal Cauchy stress (MPa)
L	Length of tissue to be dissected (mm)
G_c	Critical energy release rate (J/m^2)
l	Length of tissue at full separation (mm)
F	Mean peeling force per unit width (mN/mm)
W_{ext}	Externally applied work per unit width (J/m)
$W_{elastic}$	Stored energy per unit width (J/m)
G_c^a	Measured critical energy release rate in axial direction (J/m^2)
G_c^c	Measured critical energy release rate in circumferential direction (J/m^2)
F_c^a	Mean peeling force per unit width in axial direction (mN/mm)
F_c^a	Mean peeling force per unit width in circumferential direction (mN/mm)
U_D	End of the deformation region when the catheter begins to dissection the tissue (mm)
U_R	End of the rupturing region when the catheter begins to perforate through the bottom of the tissue (mm)
F_R	Reaction force on the catheter (N)
F_{Fric}	Frictional component of the reaction force on the catheter (N)
$\bar{I}_1$	Isochoric first invariant
t	Traction within the cohesive zone law (MPa)
δ	Separation of faces within the cohesive zone law (mm)
t_c	Maximum traction within the cohesive zone law (MPa)
δ_c	Critical traction within the cohesive zone law (mm)
U_I	End of initial stretching where tissue begins to split (mm)
U_T	End of transition region where damage was initiating (mm)
U_P	End of plateau region wherein tissue was splitting and dissection is propagating (mm)
μ_p	Shear moduli in the Ogden constitutive model (kPa)
α_p	Dimensionless Ogden constitutive model parameter
K	Bulk modulus (kPa)
L_P	Length of tissue dissected by the wedge at U_P (mm)
L_P^1, L_P^2	Upper and lower values of L_P (mm)
U_{max}	Maximum value of displacement in wedge test data (mm)
$\mathbf{F}^{exp}$	Vector of experimental reaction forces on the wedge in the initial stretching region (N)
$\mathbf{F}^{comp}$	Vector of model-computed reaction forces (N)
F_{sep}^{exp}	Mean experimental force just prior to separation (N)
F_{max}^{comp}	Maximum force within the "separation" FE model (N)
$\boldsymbol{P}$	First Piola Kirchoff stress tensor (Pa)
$W_{elastic}^1$	$W_{elastic}$ value calculated for L_P^1 (J/m)

$W^2_{elastic}$	$W_{elastic}$ value calculated for L^2_P (J/m)
G^1_c	G_c value calculated for L^1_P (J/m^2)
G^2_c	G_c value calculated for L^2_P (J/m^2)

List of Abbreviations

20hC	Control samples incubated for 20 hours
CDM	Continuum Damage Model
CID	Catheter Induced Dissection
CVD	Cardiovascular Disease
CZ	Cohesive Zone
FE	Finite Element
GOH	Gasser-Ogden-Holzapfel
LDL	Low Density Lipoproteins
PCI	Percutaneous Coronary Intervention
SHG	Second Harmonic Generation
TPM	Two Photon Microscopy

Chapter 1

Introduction

1.1 Cardiovascular disease

Cardiovascular disease (CVD) is a general term for conditions affecting the heart or blood vessels. It's usually associated with a build-up of fatty deposits inside the arteries – known as atherosclerosis – and an increased risk of blood clots. It can also be associated with damage to arteries in organs such as the heart, brain, eyes and kidneys. CVD has the highest mortality risk in the world; atherosclerosis alone accounts for approximately 28% of all deaths [5]. This places a large toll on healthcare resources and productivity. In 2006, the healthcare cost for CVD in the EU was estimated at just under €110 billion (approximately 10% of the total healthcare expenditure) and that from production losses in the economy at €41 billion. Including additional costs, the total cost to the EU economy was estimated at €192 billion a year [6]. Additionally, it is predicted that CVD occurrence will continue to increase. Heidenreich et al. predicted that by 2030 40.5% of the population of the USA will have some form of CVD [7]. They also predicted that health care costs will increase from $273 billion in 2010 to $818 billion in 2030, while the costs due to lost productivity were estimated to increase from $172 billion to $276 billion. Therefore the total cost to the USA from CVD in 2030 is estimated at over $1 trillion.

CVD often results in changes to the arterial wall structure including stiffening, ballooning, and thickening. The type of alteration varies by disease, however, often the changes in structure greatly impact the ability of the artery to function. It is then that disease often causes discomfort and is diagnosed and treated. In recent years there has been a trend toward to minimally invasive procedures rather than open surgery. Such procedures involve small incisions to the patient compared to large openings required for access in open surgery. For instance, treating a blocked coronary artery with open surgery involves opening the patient's chest, stopping their heart and using a heart-lung machine to temporarily replace the function of those organs while the blockage is bypassed. By contrast, the minimally invasive alternative involves making a small incision in the leg to gain access to the major artery. A catheter is then fed to the blocked coronary artery and the treatment deployed to widen the artery without needing to stop the patient's heart. The damage to the patient and procedure complexity are considerably reduced in the minimally invasive procedure and thus the cost of both the procedure and patient recovery are much lower. In CVD many minimally invasive procedures are performed via an intra-vascular catheter.

Improvement of treatment methods and medical device technologies may aid in alleviating the burden on health care systems. However, the design of new medical devices requires greater understanding of arterial wall mechanical properties, to reduce complications, disease recurrence and medical device failure.

1.1.1 Human artery structure

Human arteries are highly complex, exhibiting anisotropy and inhomogeneity, and containing active and passive components [8]. Moreover, the prominence of these features varies with anatomical location. Figure 1.1 shows a map of the major arteries, generally arteries nearest the heart are thicker and more elastic, to smooth the large pressure waves from the heart. Medium arteries are thinner but have more active smooth muscle cell components. The relaxation and contraction of which widens or narrows the artery inner radius respectively. Smaller arteries and arterioles are thinnest and have thinner walls reflecting the far lower blood pressure [9]. Nevertheless most arteries share a common structure and components (figure 1.2).

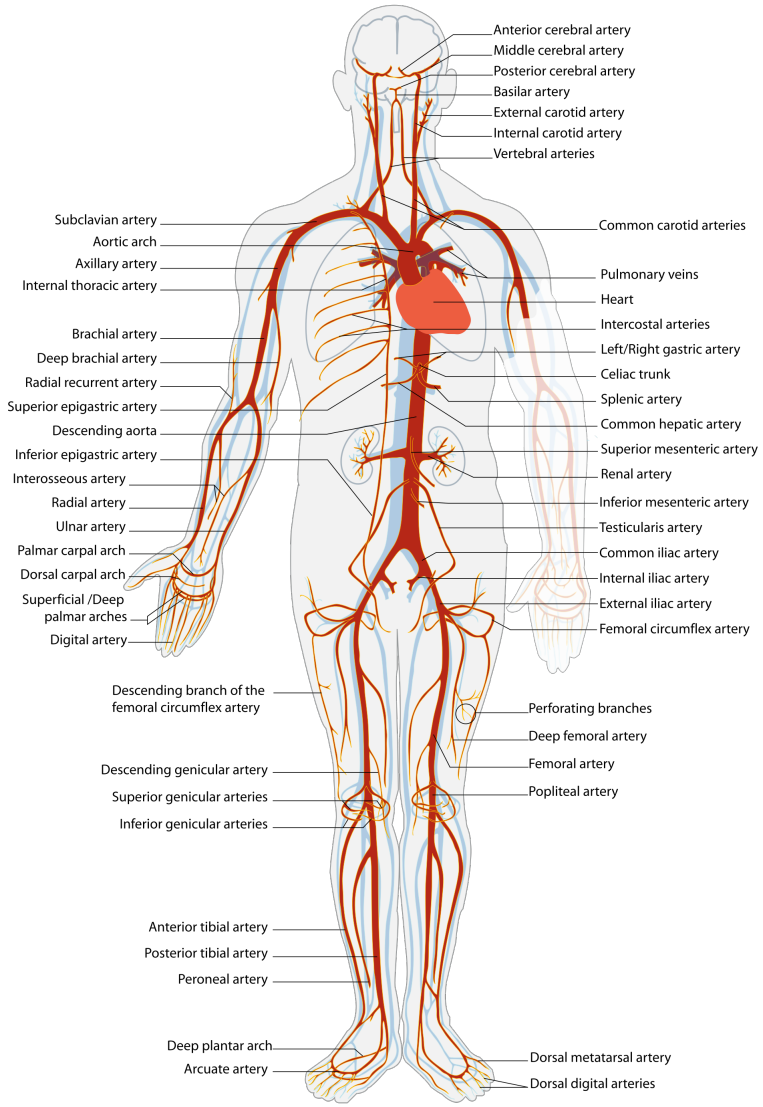

Figure 1.1: An arterial map detailing all major arteries in the human body [1].

Arteries like many soft tissues gain their mechanical strength from collagen and elastin fibres. It is generally accepted that in the two stage mechanical response seen in many soft tissues the initial compliance at low strain is a result of the

elastin stretching [10]. The collagen fibres are initially crimped and unfurl as the tissue is stretched until the collagen fibres are straightened. The tissue stiffening at high strains is then a result of the stiffer collagen fibres bearing the load. The most internal layer is the intima, which is composed of a single layer of endothelial cells and the internal elastic lamina. The endothelial cells are thin flat cells that interact directly with the blood and act as a barrier between the blood and the rest of the arterial wall, and maintain biological and chemical stability, such as controlling blood clotting. Further outwards within the intima, the internal elastic lamina serves as an attachment layer for the endothelial cells, providing mechanical strength and acting as an intermediary between the intimal and medial layers. The internal elastic lamina is composed of smooth muscle cells as well as collagen and elastin bundles. The media is the middle layer and provides the majority of the resistance of the arterial wall to the blood pressure. It is composed primarily of smooth muscle cells and elastin fibres arranged in lamina sheets around the artery wall. Additional mechanical strength is provided by collagen fibres, highly aligned with the circumferential direction. Elastin provides mechanical strength at low vessel strain to allow smoothing of systolic blood pressure peaks while collagen fibres are recruited at high strain to prevent over-inflation. The final outermost layer is the adventitia, which is primarily composed of collagen fibres that are less aligned than in the media. This fibre organisation provides resistance to over-inflation, as well as increasing the wall toughness. The adventitia attaches to surrounding connective tissue and contains small vessels and capillaries to supply blood to the smooth muscle cells of the media [11]. Similar to internal elastic lamina, the media and adventitia are joined by an external elastic lamina.

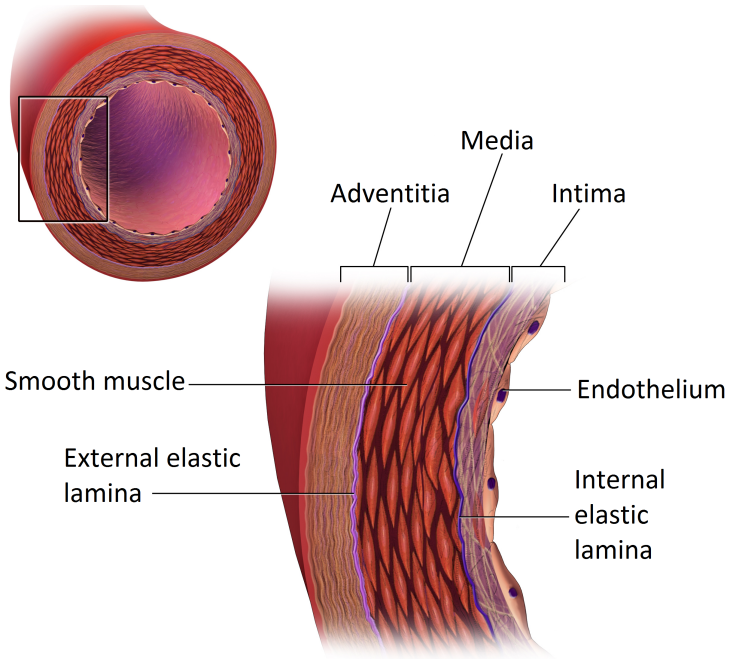

Figure 1.2: The microscopic anatomy of the arterial wall [2].

1.1.2 Arterial wall diseases

CVD encompasses a large range of diseases with varying pathological features and outcomes for the individual. The most prominent form of CVD is coronary heart disease often caused by a narrowing of the coronary arteries by fatty deposits in the artery wall, a condition known as atherosclerosis. Coronary heart disease can lead to angina, heart attacks and heart failure resulting from a lack of oxygenated blood to the heart. Strokes, an additional form of CVD, are a result of a lack of oxygenated blood to the brain. This is commonly caused in two ways: a blockage in the artery such as a blood clot either formed locally or from an upstream location; or the blood vessel rupturing, which is most commonly a result of an aneurysm (or ballooning of the vessel wall) bursting. Additionally CVD can occur in the aorta, the largest vessel in figure 1.1, with aneurysm being the most common form. Peripheral arteries in the arms and legs also suffer from CVD but are less fatal than in the major arteries. Blockages from atherosclerosis or from blood clots can lead to numbness in arms or legs and persistent ulcers. Blood clots may also break off and block arteries feeding major organs. Here two prevalent and highly investigated varieties of CVD with differing pathology and remodelling are explored, and in later sections, descriptions of the respective catheter-based procedures than can be utilised to treat them.

Atherosclerosis

Atherosclerosis is the narrowing of the artery inner radius as a result of fatty deposits accumulating between the intima and media of the wall. The deposits form as low density lipoproteins (LDLs), fat particles bound with small proteins, and pass through the endothelial layer and into the intima. Here they are ingested by white blood cells which continue to consume LDLs until they eventually burst [12]. The remnants are engulfed by further white blood cells, creating a snowball effect. The narrowed artery impedes blood flow to downstream tissue, which can eventually lead to insufficient oxygen supply and heart failure. Alternatively, the blockage can rupture; in less severe cases this exposes clot-inducing proteins leading to blood clots that further occludes the vessel or break off and occlude downstream vessels. However, the rupture can also be massive, resulting in large quantities of plaque and clot-inducing proteins being released, rapidly clotting the vessel and almost certainly leading to heart failure [13].

Intercranial aneurysm

Aneurysms most commonly form on the abdominal aorta and in the vessels feeding the brain (intercranial aneurysms). While the conditions share high level similarities, the means by which they initiate, develop, and are subsequently treated differ. According to a recent estimate, 3.2% of the population harbour intracranial aneurysms [14].

These are most common on artery branches because of the weaker wall and unusual flow patterns. Initiation and causes are still unknown but properties of blood flow such as wall shear stress and wall pressure are strongly linked, alongside genetic and biochemical factors [15, 16]. If the aneurysm ruptures, the downstream tissue will be starved of oxygenated blood, possibly leading to tissue death. Further blood will fill the space within the skull, leading to elevated pressure on the brain tissue. This in turn may cause damage to, and possible spasming of nearby vessels, further reducing the oxygen supply to surrounding tissue and likely the individual will suffer a stroke and possible brain damage.

1.2 Endovascular surgery

As mentioned, minimally invasive procedures reduce the cost and complexity for treating many diseases and are correspondingly preferred over open surgery. Endovascular surgery is one variety of minimally invasive procedure that is utilised to treat most types of CVD and in particular atherosclerosis and intercranial aneurysm. Here, an incision is made in the leg to gain access to the femoral artery from where a catheter will be introduced. However, first a guide wire is inserted into the artery. This is highly flexible and so can be guided to the treatment area through the vasculature with ease. The catheter is then fed along the guide wire to the treatment area where treatment is administered.

In atherosclerosis it is common for a balloon and stent to be deployed from the catheter to widen the artery lumen. This procedure is known as percutaneous coronary intervention (PCI). At the blockage, the balloon is inflated to push back the plaque. The stent expands with the balloon and can not contract back to its original position and so acts to hold back the plaque (figure 1.3).

For intercranial aneurysm one common treatment method is to detach coils into the body of the aneurysm while passing an electric current through them. The current initiates blood clotting within the aneurysm such that blood clots in the aneurysm body. This blood clot occludes blood flow into the aneurysm, and is aimed at lowering pressure on the aneurysm dome and thereby preventing expansion of the aneurysm and rupture [17] (figure 1.4).

Catheter-based procedures are often preferred to surgical intervention because of lower patient recovery time and decreased expense [18, 19]. Increasing prevalence drives the need to reduce complications and correspondingly the cost of treatment. A key means of achieving this is development of catheters that are less damaging to vascular tissues.

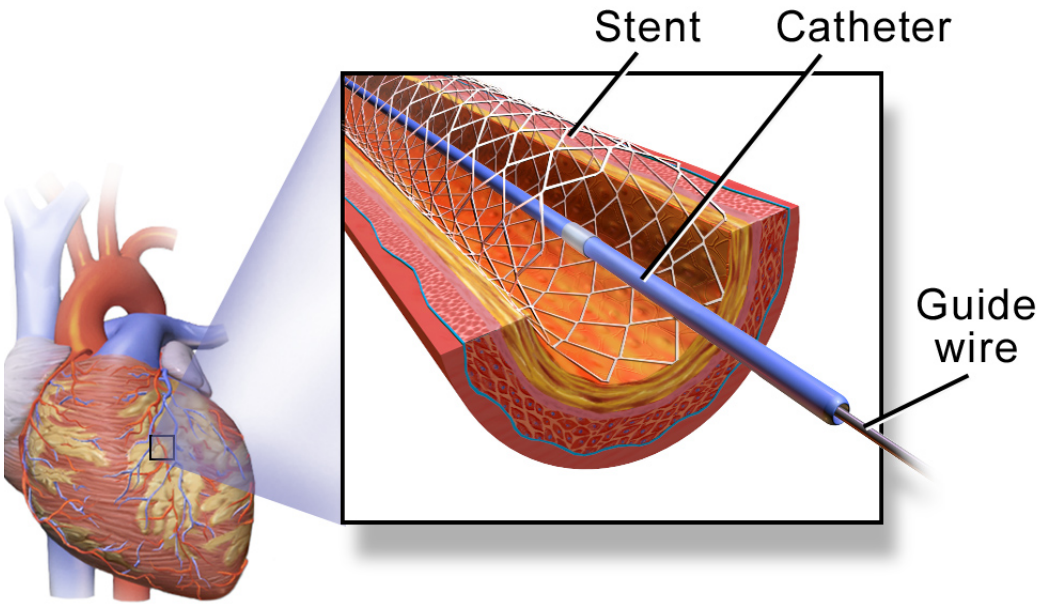

Figure 1.3: A deployed stent after angioplasty. The catheter and guide wire can be clearly seen [2].

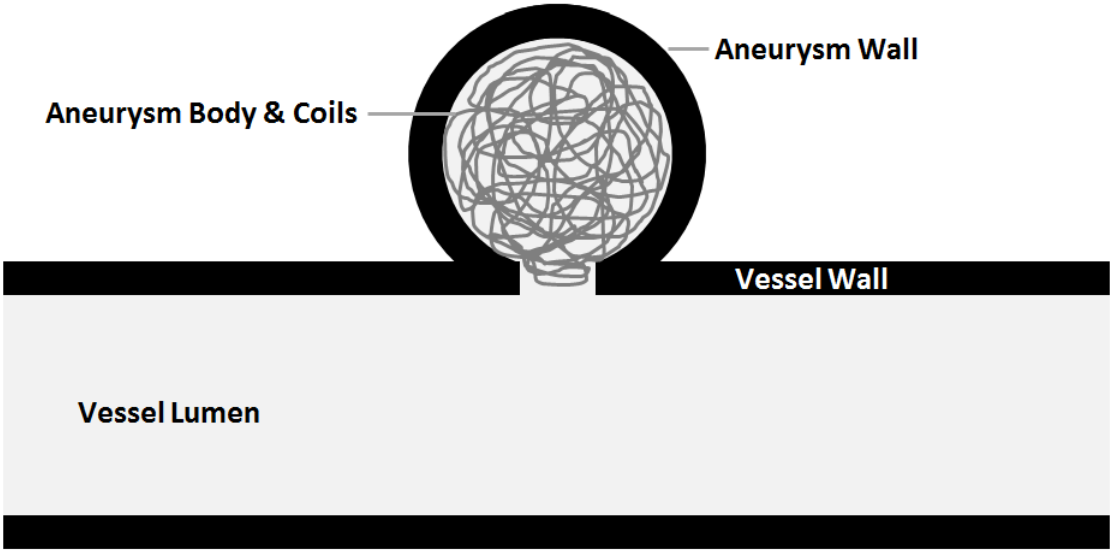

Figure 1.4: Depiction of an idealised coiled aneurysm. Coils are deployed to fill the body of the aneurysm.

1.2.1 Complications

Endovascular surgery has many unique complications that if left untreated can have severe consequences for the patient. Damage to the vessel wall by a catheter as it moves from the entry site to the treatment area is of particular interest in this work.

Damage by the catheter

When the catheter is moving through the blood vessel the shaft will rub against the vessel wall, which can activate or even damage the endothelial cell layer. Damage can be minimal, such as disrupting the glycocalyx, a layer of glycolipids and glycoproteins

which acts as an interface between the endothelial cell and the blood, or even shearing and separation of the endothelial layer itself. Though, as the glycocalyx acts to prevent thrombus formation and cell adhesion to the vessel wall, even minor disruption may have undesirable consequences [20]. Furthermore, frictional forces can also lead to vasoconstriction and spasming of the wall, increasing the likelihood of damage [21].

If damage is large enough, blood vessel function may be severely impeded, an example being perforation of the vessel by the catheter, potentially resulting in internal bleeding. In major blood vessels, such as the aorta, this will most likely be fatal. An additional example is dissection, or mechanical separation of the media of the arterial wall. This is almost always initiated by trauma, either directly to the vessel wall, e.g. a catheter induced dissection (CID) from piercing or tearing the intimal layer of the vessel during an endovascular procedure [22], or indirectly via external trauma, for instance from motor vehicle crashes [23]. Depending on the direction of blood flow, the circulatory pressure will either press the tissue flap to the wall or act to propagate the dissection (figure 1.5). The former often results in the dissection remaining benign, whereas the latter can eventually progress to create a large tissue flap that blocks downstream blood flow in the true lumen and encourages flow into the newly formed *false* lumen between the flap and remaining artery wall.

The media of the arterial wall is most prone to dissection, as a result of its organisation into lamella units, stacked on top of one another [24]. These lamellae are primarily composed of fibres of rubber-like elastin and stiffer collagen, and smooth muscle cells. These constituents, moreover, are oriented predominantly within planes tangential to the vessel axis, and with a bias towards circumferential directions over axial [25]. This organisation in turn imparts the highest mechanical strength in circumferential directions, somewhat lower strength in axial directions, and significantly lower strength in radial directions [26, 27]. The structure can be seen in figure 1.6.

1.3 Investigating damage

The increasing usage of endovascular treatment methods and the high prevalence of cardiovascular diseases necessitates tools for modifying and improving endovascular device designs. For instance, to reduce the incidence of CID more knowledge is needed about the mechanics underlying its initiation and propagation, and correspondingly about the interactions between catheters and tissues during endovascular surgery. Both experimental (e.g. mechanical testing of *ex vivo* specimens) and computational (e.g. finite element analyses of propagation scenarios) approaches may be useful for this purpose.

Computational approaches often rely upon the finite element (FE) method to

model complex device-vessel wall interaction. The FE method is a numerical solution method for partial differential equations, such as those that govern continuum solid and fluid mechanics problems. It consists in discretising the continuum equations to form a linear system whose solution is a close approximation of the continuous solution. This is achieved in practice by decomposing the problem domain into a mesh of geometrically simple elements, interconnected at nodal points, over which field variable values are approximated by correspondingly simple functions, like low-order polynomials. The resulting discrete equations are well-suited to computer solution.

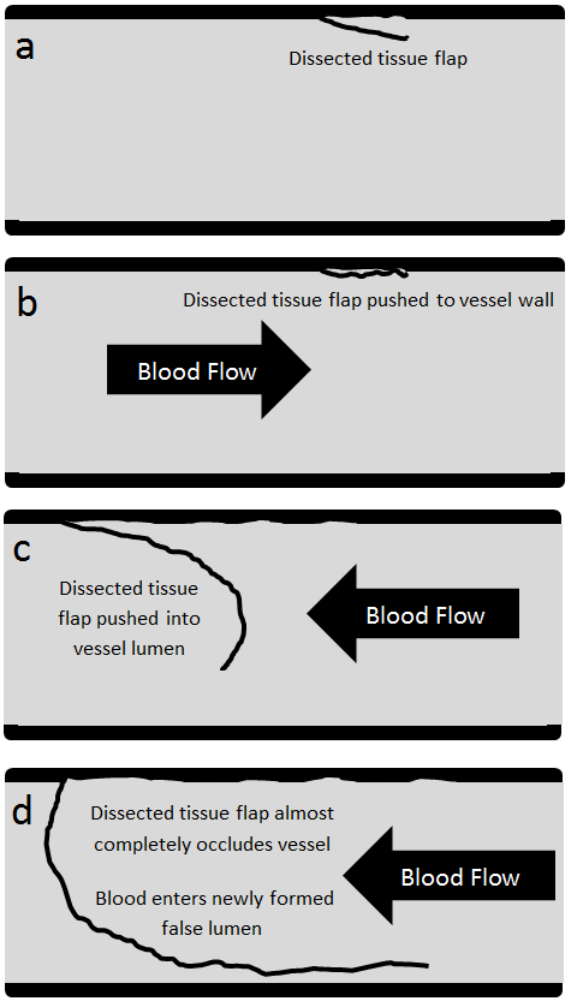

Figure 1.5: Schematic illustrating formation of benign or propagating dissections depending on blood flow direction. a: initial dissection with tissue flap extending in to vessel lumen. b: tissue flap pushed back onto vessel wall by blood flow, creating a benign scenario. c: further tissue peeled from the vessel wall by blood flow, causing the tissue flap eventually to obscure a large portion of the vessel lumen. d: tissue is peeled further still, the blood flow pushes the tissue into a concave shape that traps the blood and promotes further dissection. The space between the wall and the flap is now a false lumen.

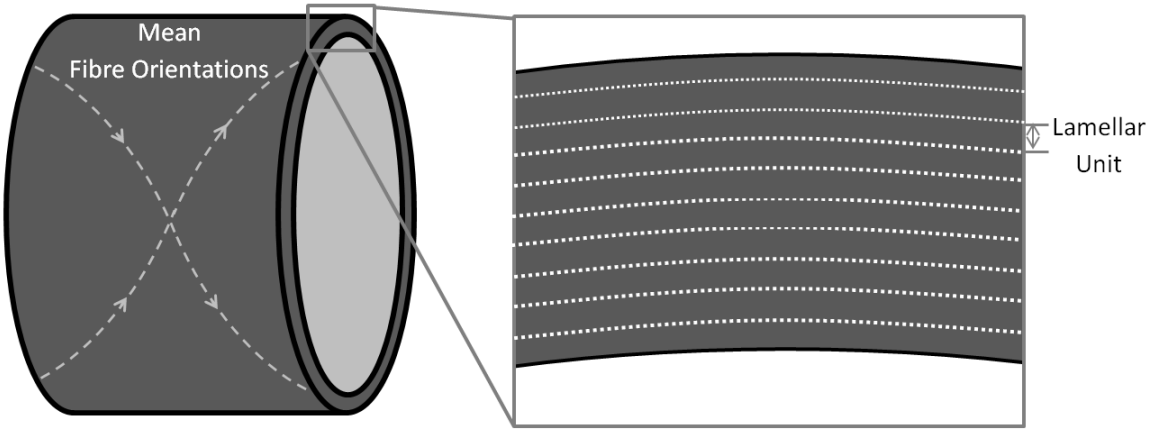

Figure 1.6: Idealised representation of the organisation of the aortic media. The intima and adventitia (not depicted) adjoin this layer on its inside and outside, respectively.. Families of fibres are oriented predominately into helices around the vessel wall, as shown on the left, with mean orientations closer to circumferential, rather than axial directions. The lamellae are stacked upon one another with interconnecting fibres providing some radial resistance.

1.4 Thesis aims and objectives

The main objective of this thesis is to develop new experimental and computational techniques for characterising catheter-induced blood vessel damage, and which may correspondingly be used as tools in the improvement of catheter design. Two high-level objectives to that end have been formulated:

1. Provide a means of creating a diseased tissue model from healthy porcine aorta, with the goal to reduce the cost of associated research and medical device design.

2. To investigate dissection propagation by an endovascular catheter and the underlying mechanisms involved.

1.4.1 Creating a diseased tissue model

Improvement of medical device designs (such as endovascular catheters) requires significant *in vitro* experimentation and testing with vascular tissue. Ideally, diseased tissue, properly reflecting the *in vivo* conditions experienced by these devices, should be used. However, obtaining diseased human tissue in quantity is difficult (both practically and ethically) and costly. By contrast, porcine arteries are considered waste tissue by abattoirs and so are readily available. The first objective thus is aimed at developing and verifying procedures for modifying the properties of porcine tissue such that they resemble those of diseased tissue, meaning in turn that they can be used as a cheap and abundant model of the latter in the context of medical device physical testing.

The variation of mechanical properties between healthy porcine tissue and diseased human tissue is a result of differences in the structure, concentrations and properties of the arterial wall constituents (identified in section 1.1.1). Regional variations in the structural arrangement of these components produces similar variations in the regional anisotropic behaviour. Disease and ageing, however, alter the respective compositions, leading to often undesirable changes in function. Ageing has been shown to cause a loss of medial elastin followed by an increase in the stiffer collagen fibres, further stiffened by additional cross-linking, to compensate [28, 29, 30, 31]. This results in the elastin-collagen interaction altering and the stiffer collagen fibres being recruited at smaller deformations, leading to an observed stiffening of the arterial wall. Whilst in aneurysm formation, the characteristic ballooning is also widely attributed to loss of elastin and a resulting loss of stiffness in the artery [32, 33]. In atherosclerosis, changes in elastin and collagen structure again weaken the medial and intimal layers [34, 35, 36]. Genetic diseases can also have large effects on collagen and elastin fibres leading to greatly reduced stiffness and toughness in blood vessel walls [37]. For instance, Marfan syndrome is caused by a mutation to the fibrillin-1 glycoprotein which in turn affects elastin protein structure in the thoracic aorta, resulting in a weakened arterial wall [38]. These changes are often complex and multifaceted. Correspondingly, alterations such as the loss of elastin may increase or decrease stiffness depending on a variety of co-factors.

In this work enzyme and chemical treatments were used to alter the mechanical response of healthy porcine aorta with the aim to emulate diseased tissue mechanical properties. Previous studies had employed similar methods and utilised various mechanical testing procedures to evaluate the associated changes. Uniaxial tensile testing has been performed following elastase and collagenase treatment to investigate whether collagen is solely responsible for the softening behaviour of arterial walls [39]. They found that removing collagen removed the softening behaviour of tissue whilst removing elastin resulted in continuous softening behaviour. Additionally, [40] evaluated the uniaxial mechanical response of the elastin or collagen fibres in isolation from one another by applying the same enzyme treatments to aortic wall. They observed that completely removing collagen resulted in a linear mechanical response that like before had no softening behaviour. While removal of all elastin resulted in a non-linear anisotropic response that again showed continuous softening.

Biaxial testing has also been utilised to evaluate the changes in mechanical response, Chow et al. investigated the changes in mechanical behaviour of arterial wall following progressive elastase treatment [41]. Distinct mechanical responses were identified for each level of tissue degradation with tissue initially becoming more compliant but then stiffening until full elastin loss where tissue is far stiffer than the controls. Gundiah et al. also performed biaxial testing but following elastase and collagenase treatment at two different levels of degradation [42]. Collagenase

treated samples showed a decreased non-linearity compared to controls whereas elastin treatment resulted in significantly stiffer tissue response.

Finally pressure-inflation testing had also been performed following enzyme treatment. Kochova et al. applied collagenase and elastase treatments and found that the former altered the stiffness of the arterial wall and while the latter altered the wall geometry, it did not effect the mechanical response [43]. In another study elastase treatment resulted in the tissue being more ductile at low strains and stiffer at high strains [44].

Compared to these works the key novelty in chapter 2 was testing samples to the point of failure following enzyme treatment. Only one previous study had tested tissue to failure following enzyme digestion but only after collagenase treatment [45]. Uniaxial tensile testing was applied like here, however, strain was measured directly from the tensile test machine arms and stress calculated from the unloaded cross-sectional area reducing the accuracy of the data. Furthermore, in that study no constitutive modelling was employed to allow description and comparison of the overall tissue elastic response unlike in chapter 2.

Additionally, in chapter 3 controlled peel testing was performed to investigate the effect of the enzyme and chemical treatments on the arterial dissection behaviour. While the dissection behaviour had been investigated by both peel testing and liquid infusion tests [46, 47, 48, 49], no work has investigated the effect of removing and cross-linking constituent proteins on the dissection response.

1.4.2 Catheter-induced dissection (CID)

Catheter induced dissections (CIDs) are a rare but commonly fatal complication of intravascular catheterisation. Data on CID occurrence is sparse, however, major complications such as coronary artery dissection that extends to the aortic root has been reported to occur in 9 out of 43143 cardiac catheterisations (approximately 0.02%) [50]. However, this increased to 0.2% if patients were undergoing treatment for myocardial infarction. Another study [51] found the same type of dissection in 15 of 12031 percutaneous coronary intervention (PCI) procedures (approximately 0.12%). Data for this type of dissection are most prevalent because of its high mortality rate, however for coronary artery dissection alone, or CID of other arteries, data are sparser. In addition, it is difficult to provide context for these figures in terms of total complications, as CID are often included as part of other categories such as vascular trauma [52]. However, in [53] the overall complication rate for PCI was estimated at 2.7% for the period 2003-2006, from which it may be loosely inferred that coronary CID extending to the aortic root occurs in 5% of PCI procedures. Furthermore, the mortality rate is relatively high: 67% of deaths from coronary catheterisation procedures reported in [54] were from CID of the coronary arteries, while [55] reported that 25% of aortic CIDs that require surgical intervention lead to

death of the patient.

Unfortunately it is difficult to ascertain how CIDs are initiated or propagated. This is because, commonly, catheterisation procedures are observed via three dimensional rotational angiography, and the dissection can only be detected by its effect on the blood flow. Thus, visualising the blood vessel wall and the damage to it is very difficult. Furthermore, the spatial resolution of such imaging modalities is relatively low, meaning it is difficult to identify the dissection until its effect on the blood flow is pronounced. As a result there is little information in the literature on mechanisms by which CIDs in arteries are initiated or propagated. Therefore, means by which a CID is propagated can only be speculated. In chapter 4 a scenario was postulated in which the dissection has been initiated (the means by which were left for future investigations) and the catheter is positioned at the dissection front. The endovascular surgeon operating the catheter feels resistance to their attempts to guide the catheter to its destination as the catheter pushes against the dissection front. Assuming it is a bend in the vessel, they apply force to the catheter to propel it around this assumed bend. This inadvertently pushes the catheter into the created dissection front, driving the catheter between the layers of the media, and opening the dissection further. A corresponding experimental configuration was then devised to explore this scenario.

Arterial dissection has been well investigated both by *ex vivo* testing in a laboratory, and simulations with the FE method. The first *ex vivo* arterial wall dissection was performed via liquid infusion into the artery media [47, 49, 56]. This was aimed at replicating blood flow-driven propagation of the dissection. Later, controlled peeling of the media was employed to gain further understanding of the force displacement behaviour, and in particular the latter's anisotropy [46, 48]. This methodology was then utilised on diseased arteries and aneurysms to assess disease-associated changes [57, 58].

CZ approaches have been used in various forms to model dissection of arterial layers during peel testing [59, 60], similar to those presented in chapter 3. However, dissection driven by an external body, i.e. a catheter, is fundamentally different from a peeling configuration. In the case of peeling, tissue at the crack front experiences almost pure tension perpendicular to the direction of crack propagation, and newly exposed fracture surfaces are free. Conversely, when dissection is driven by an external body, tissue at the crack front experiences a complex combination of tension, as it is forced around the penetrating object, and compression, from the direct loading of the object. Moreover, the newly formed surfaces, rather than being free, are subject to a complex interaction with the external object.

Comparable configurations exist during, for example, needle insertion and cutting. Among other approaches, CZ models have been used by various authors to simulate the tissue rupture processes in such scenarios, also. Needle insertion of muscle tissue

has been investigated with parameters extracted from separate experimental data [61], however no direct experimental validation was presented in turn. This was partially addressed by Forsell and Gasser when modelling cardiac tissue penetration and failure as a result of perforation by a pacemaker wire [62]. However, it was not clear how the governing critical energy release rate G_c was calculated from the experimental data, making it difficult to assess the fidelity of their FE model with respect to the latter. Finally, Oldfield et al. utilised an experimental-computational approach to estimate G_c during needle insertion into a gelatine soft tissue phantom [63]. This approach yielded good agreement between experimental and computational force-displacement profiles at four different insertion rates and was more comprehensive than the previous studies mentioned. However, gelatine is a homogeneous isotropic material that does not exhibit the stochastic breaking of fibres/fibrils seen in perforation and damage of most soft tissues [64], and so it is still unclear how well the CZ formalism carries over to real soft tissues in this context. A final, and important aspect that was superficially assessed, at best, in the foregoing studies is the fidelity with which the complex catheter-tissue interactions, especially near the crack tip, can be captured with CZ finite element formulations. As mentioned, this phenomenon is one of the key features that differentiate dissection by means of a penetrating external body, from simpler peeling configurations.

Though no previous authors appear to have studied penetration of arterial tissue using cohesive rupture modelling approaches, much less CID specifically, the foregoing studies suggest this is a promising approach. Such models are therefore investigated for this purpose in chapters 4 and 5, with an emphasis on clarifying the points of ambiguity that were identified. Specifically, CZ formalism is employed to model the dissection process as a catheter, and later a metal wedge, is forced between adjacent arterial tissue layers. An experimental configuration is first described, and corresponding results are presented and discussed. CZ theory is then described and applied within a FE model of the experimental configuration. Finally, numerical issues related both to the above interaction phenomena and to the constitutive description of the tissue are reported and discussed.

1.5 Thesis Overview and Structure

The thesis structure can be seen in figure 1.7, the described objectives are pursued in chapters 2-5. Conclusions and consideration of future directions are subsequently presented.

The development of a diseased tissue model for use in testing of medical devices is presented in **chapter 2**. Porcine aorta was treated with collagenase, elastase or glutaraldehyde to alter its mechanical response. It was then subjected to uniaxial tension until failure, while the force and displacement were recorded. The force-displacement

response for the arterial samples from each treatment type was compared to that of the controls. Finally, a damage constitutive model was fit to the experimental data to give further basis for comparison.

This work is then extended in **chapter 3** by performing controlled peel tests on similarly treated porcine aorta. This afforded insight into the effects of the treatments on dissection failure modes, which are the modes of interest in subsequent modelling chapters. As in chapter 2 the force-displacement response of the treated samples was compared to that of the control samples. The fracture energy was also calculated for the mean tissue response for each treatment type as a measure of resistance to dissection, and to provide a further means of comparison.

Chapter 4 describes a novel approach to modelling the propagation of a CID. A CZ-based FE model of a dissection scenario was developed, in which a catheter is driven between layers of an aortic wall. Experimental measurements of the reaction forces experienced by a catheter in these conditions were also acquired, for comparison. While the model performance was promising, numerical difficulties and uncertainty regarding the conditions at the catheter-tissue interface suggested the results were unreliable. To resolve these issues, a physically simpler dissection scenario was subsequently developed in chapter 5.

In **Chapter 5**, following the uncertainties in chapter 4, the effectiveness of CZ models when an external body is driving the dissection (such as CID) was evaluated. The FE model and experimental procedure were simplified to allow the underlying mechanisms to be more easily extracted. The critical energy release rate, calculated directly from the experimental data, was placed in the FE CZ model and the force-displacement response was compared between the FE model and the experiment. Finally, the sensitivity of FE model force-displacement on the cohesive zone model parameters was evaluated and limitations of the CZ model are presented.

As noted, the main contributions described in this thesis have been published in peer-reviewed journal articles. Specifically, chapter 2 draws heavily on the work presented in [65]; chapter 3 is based on the developments in [66]; and chapter 5 relates closely to the results in [67].

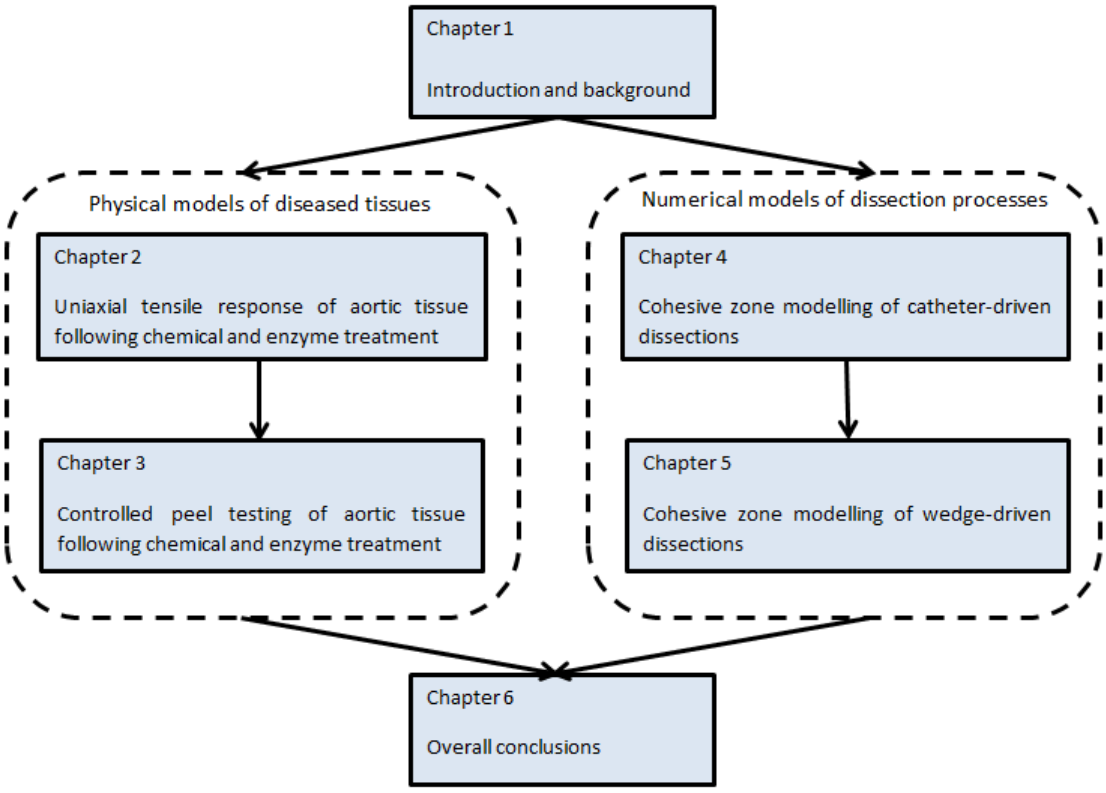

Figure 1.7: Flowchart depicting the thesis structure.

Chapter 2

Creating a model of diseased artery damage and failure from healthy porcine aorta

2.1 Introduction

Improvement of medical device designs (such as endovascular catheters) requires significant *in vitro* experimentation and testing with vascular tissue. Ideally, diseased tissue, properly reflecting the *in vivo* conditions experienced by these devices, should be used. However, obtaining diseased human tissue in quantity is difficult (both practically and ethically) and costly. By contrast, porcine arteries are considered waste tissue by abattoirs and so are readily available. The first objective thus is aimed at developing and verifying procedures for modifying the properties of porcine tissue such that they resemble those of diseased tissue, meaning in turn that they can be used as a cheap and abundant model of the latter in the context of medical device physical testing.

The variation of mechanical properties between healthy porcine tissue and diseased human tissue is a result of differences in the structure, concentrations and properties of the arterial wall constituents (identified in section 1.1.1). Regional variations in the structural arrangement of these components produces similar variations in the regional anisotropic behaviour. Disease and ageing, however, alter the respective compositions, leading to often undesirable changes in function. Ageing has been shown to cause a loss of medial elastin followed by an increase in the stiffer collagen fibres, further stiffened by additional cross-linking, to compensate [28, 29, 30, 31]. This results in the elastin-collagen interaction altering and the stiffer collagen fibres being recruited at smaller deformations, leading to an observed stiffening of the arterial wall. Whilst in aneurysm formation, the characteristic ballooning is also widely attributed to loss of elastin and a resulting loss of stiffness in the artery [32, 33]. In atherosclerosis, changes in elastin and collagen structure again weaken the medial and intimal layers [34, 35, 36]. Genetic diseases can also have large effects on collagen and elastin fibres leading to greatly reduced stiffness and toughness in blood vessel walls [37]. For instance, Marfan syndrome is caused by a mutation to the fibrillin-1 glycoprotein which in turn affects elastin protein structure in the thoracic aorta, resulting in a weakened arterial wall [38]. These changes are often complex and multifaceted. Correspondingly, alterations such as the loss of elastin may increase or decrease stiffness depending on a variety of co-factors.

In this work enzyme and chemical treatments were used to alter the mechanical response of healthy porcine aorta with the aim to emulate diseased tissue mechanical properties. Previous studies had employed similar methods and utilised various mechanical testing procedures to evaluate the associated changes. Uniaxial tensile testing has been performed following elastase and collagenase treatment to investigate whether collagen is solely responsible for the softening behaviour of arterial walls [39]. They found that removing collagen removed the softening behaviour of tissue whilst removing elastin resulted in continuous softening behaviour. Additionally, [40] evaluated the uniaxial mechanical response of the elastin or collagen fibres in

isolation from one another by applying the same enzyme treatments to aortic wall. They observed that completely removing collagen resulted in a linear mechanical response that like before had no softening behaviour. While removal of all elastin resulted in a non-linear anisotropic response that again showed continuous softening.

Biaxial testing has also been utilised to evaluate the changes in mechanical response, Chow et al. investigated the changes in mechanical behaviour of arterial wall following progressive elastase treatment [41]. Distinct mechanical responses were identified for each level of tissue degradation with tissue initially becoming more compliant but then stiffening until full elastin loss where tissue is far stiffer than the controls. Gundiah et al. also performed biaxial testing but following elastase and collagenase treatment at two different levels of degradation [42]. Collagenase treated samples showed a decreased non-linearity compared to controls whereas elastin treatment resulted in significantly stiffer tissue response.

Finally pressure-inflation testing had also been performed following enzyme treatment. Kochova et al. applied collagenase and elastase treatments and found that the former altered the stiffness of the arterial wall and while the latter altered the wall geometry it did not effect the mechanical response [43]. In another study elastase treatment resulted in the tissue being more ductile at low strains and stiffer at high strains [44].

Compared to these works the key novelty here was testing samples to the point of failure following enzyme treatment. Only one previous study had tested tissue to failure following enzyme digestion but only after collagenase treatment [45]. Uniaxial tensile testing was applied like here, however, strain was measured directly from the tensile test machine arms and stress calculated from the unloaded cross-sectional area reducing the accuracy of the data. Furthermore, in that study no constitutive modelling was employed to allow description and comparison of the overall tissue elastic response unlike in this study.

As in the work mentioned previously, enzymatic digestion was applied to porcine aortic media samples, to degrade the constituent proteins. Low concentration glutaraldehyde treatment was also utilised, as an alternative method to mimic cross-linking and stiffening seen in processes like glycation [68, 69]. Treated tissue was then stretched in uniaxial tension to failure in both the vessel axial and circumferential directions. Constitutive models were then employed to allow description and comparison of the overall tissue response under loading. This allowed the gradual changes in the mechanical response to be related to the structural alterations associated with the different treatment types. The well-known Gasser-Ogden-Holzapfel (GOH) model was utilised for the elastic component of the tissue response (prior to damage). This model compromises an isotropic neo-Hookean term, accounting for the elastin fibres and ground substance, and an exponential term for each of the two collagen fibre families [70]. The damage and failure behaviour were captured using the continuum

damage model (CDM) described in [71], which has previously been shown to capture well the failure behaviour of arterial tissue when combined with the GOH model [72].

2.2 Methods

2.2.1 Mechanical Testing

Sample Preparation

Porcine aorta was chosen as the experimental model due to (i) its availability, allowing many tests to be performed, and (ii) its thickness, allowing the media and intima, the layers most affected by disease processes, to be easily tested in isolation. The region proximal to the heart of the upper thoracic aorta was chosen to ensure sufficient thickness. However, arterial wall properties vary along the artery and even when this is minimised by selecting a short region to cut samples from, variation will occur and may generate some spread in results in later sections. No ethical considerations were required. Many other animals can also supply aorta as readily as pigs [73, 74], however porcine tissue has one of the closest associations with human tissue and has been successfully transplanted to humans [75]. Alternatively synthetic tissue[1] could be utilised as a model for healthy artery, however, currently no synthetic diseased artery has been produced.

Control tissue was tested within 24 hours of the slaughter of the animal and treated tissue within 48 hours, the latter owing to the additional incubation time associated with the treatments. All tissue was stored in a refrigerator when not undergoing treatment.

The aorta from was initially cut into 40×15 mm pieces aligned in axial and circumferential directions. As mentioned the adventitia is least affected by disease processes and thus was removed by making an incision midway through the arterial through-thickness and carefully peeled manually to separate the unwanted tissue. As removal of the adventitia could not be verified, more tissue was discarded than necessary to ensure complete removal of the adventitia. The remaining tissue was carefully cut into a dog bone shape with approximately 5 mm gauge width and 10 mm length and stored in solution.

Treatments were applied to remove or alter constituent proteins because as mentioned in section 2.1 many disease processes are associated with loss or alteration of these proteins. Collagenase and elastase will digest and partially remove collagen and elastin respectively while gltaraldehyde will cross-link the proteins. All non-control samples were treated with their respective solutions as described in table 2.1. All treatments were diluted in saline solution with antibiotics (Penicillin and Streptomycin) and fungicide to prevent growth of micro-organisms. To ensure the

[1] such as that produced by SynDaver http://syndaver.com/shop/syntissue/arterial-tissue

accompanying incubation process had no effect on sample mechanical properties, an additional group of controls were incubated for 20 hours and tested. Following treatment, all samples were washed thoroughly with saline solution to remove trace elements of chemical and enzymes.

Table 2.1: Enzyme, glutaraldehyde and control treatment concentrations and durations.

Treatment	Solution	Temp.	Duration	N(axial)	N(circ)
Control (Fresh)	-	-	Fresh	16	16
20 hour Control (20hC)	-	37°C	20 hours	10	14
Collagenase (Roche)	0.05 U/ml	37°C	20 hours	10	11
Elastase (Sigma Aldrich)	0.2 U/ml	37°C	20 hours	13	11
Glutaraldehyde	0.1%	4°C	20 hours	14	14

Test Protocol

Specimens were prepared for tensile testing by carefully adhering two pairs of small black markers to the gauge region, using tweezers and super-glue. These allowed measurement, via optical means, of the stretches in the first and second principal directions [76]. Representative sample geometry and marker placement is shown in figure 2.1. Test specimens were placed back in saline solution for around 5 seconds to moisten them after placing the markers, and placed in grips mounted to a Tinius Olsen 5 kN tensile machine. The grips had serrated edges which prevented slippage; thus, the addition of sand paper was not necessary for this study. Approximately 50% of samples were discarded with the most common reasons being poor or patchy digestion of samples and samples not breaking in the gauge region. In this work more physiologically relevant test conditions such as a saline bath at 37°C were not available thus samples were tested in open air. Samples were prevented from drying out by moistening before the test and reducing the test duration to a minimum. Additionally any samples that were drying out were manually rehydrated by pipetting saline solution onto the sample between preconditioning and the final recorded test to failure. However, it is likely that sample drying occurred and may have altered tensile properties. A humidifier may prevent drying from occurring during open air testing however such a device was not available at the time of testing. Additionally, it has been shown that distortion by refraction could reduce the accuracy of the marker position recording and thus care must be taken when using this or a saline bath [77]. Preconditioning was performed by applying 10 displacement loading cycles of 15 mm at 0.1 Hz with a final, 11th, loading cycle constituting the recorded experiment. The test was filmed using a Fujifilm Finepix Z90 digital camera. Accuracy and effects such as image distortion by the lens were investigated prior to use, and found to be insignificant. TrackMate plug-in within Fiji software[2] was utilised with

[2]**http://fiji.sc/TrackMate**

the recording to register and track the paired markers to ascertain stretch in each principal direction. The recording equipment was also utilised with Fiji to measure the tissue initial width and thickness, by photographing the unloaded tissue with a ruler adjacent for scale. The whole test configuration can be seen in figure 2.1.

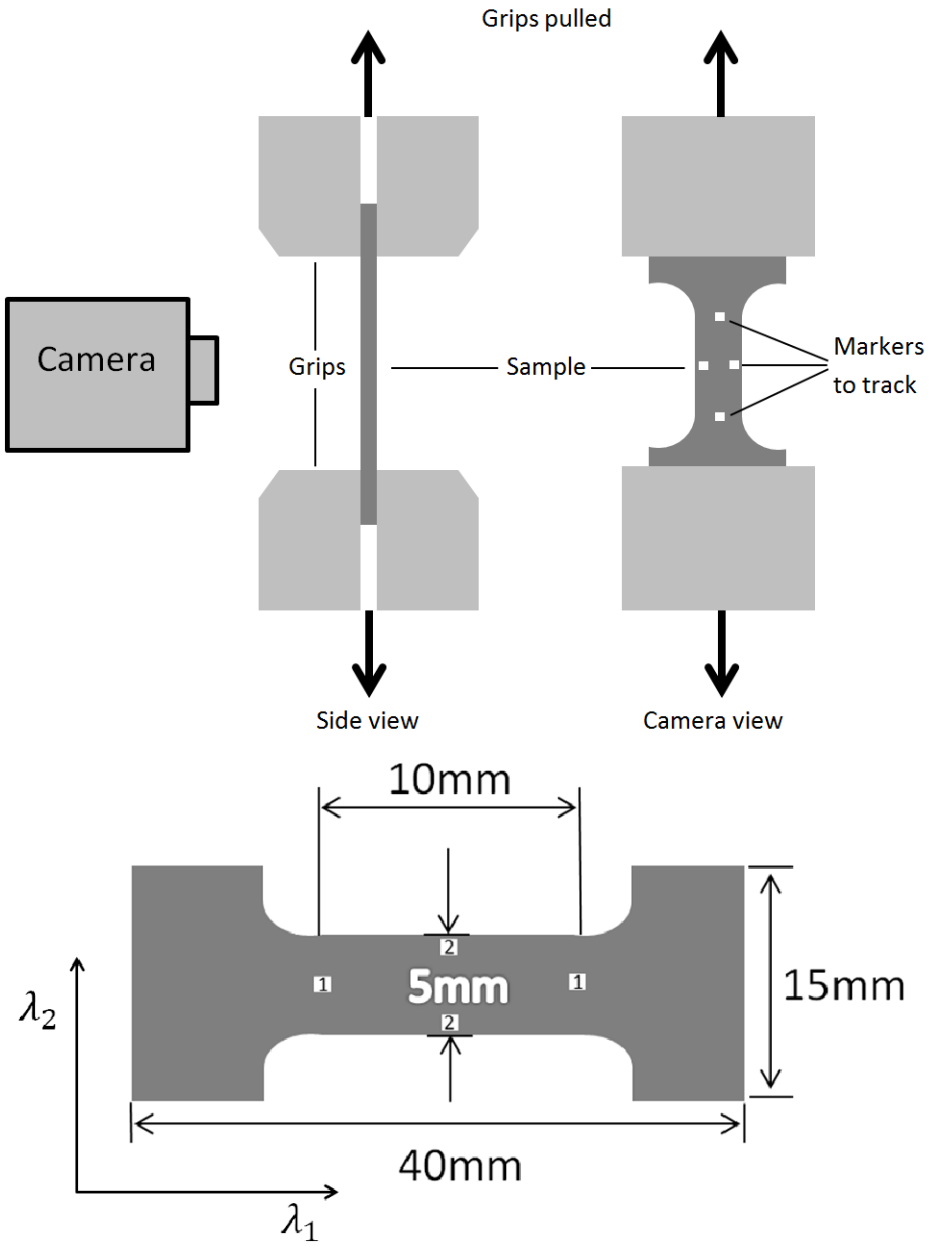

Figure 2.1: Top. Schematic of test apparatus from the side and the front (camera view). Bottom. Sample geometry with marker positions indicated (white squares). Marker labels indicate the principal stretch direction characterised with that label.

2.2.2 Constitutive Modelling

Motivated by the nonlinearity and anisotropy of arterial walls [78, 79], we have utilised the GOH model to describe the elastic behaviour [70]. This has been used frequently to capture the response of arterial walls in uniaxial tension [80, 39, 40].

Weakening of the material, as it is deformed beyond its elastic range, and ultimate failure is incorporated into the model by means of a continuum damage model (CDM) [71]. The CDM components scales the stress according to the level of damage the tissue has undergone. It becomes active only after damage initiation conditions have been met.

Kinematics

A deformable body in a stress free state is said to be in its reference configuration Ω_0 and when loaded deforms to its current configuration Ω. The motion χ transforms a given point $\mathbf{X} \in \Omega_0$ to a position $\mathbf{x} = \chi(\mathbf{X}) \in \Omega$. From this the deformation gradient $\mathbf{F} = \partial\chi(\mathbf{X})/\mathbf{X}$ with $J = \det(\mathbf{F}) > 0$, the local volume ratio or Jacobian.

Elastic Response

The strain energy function Ψ of the GOH model comprises an isotropic Neo-Hookean term Ψ^m, accounting for elastin fibres and ground matrix, and anisotropic exponential terms Ψ^f, for each of two families of collagen fibres:

$$\Psi(\mathbf{C}, \mathbf{H}_i) = \Psi^m(\mathbf{C}) + \sum_{i=1,2} \Psi_i^f(\mathbf{C}, \mathbf{H}_i(\mathbf{a}_i, \kappa)), \tag{2.1}$$

with

$$\Psi^m(\mathbf{C}) = \frac{\mu}{2}(\lambda_1^2 + \lambda_2^2 + \lambda_3^2 - 3) \tag{2.2}$$

and

$$\Psi_i^f(\mathbf{C}, \mathbf{H}_i) = \frac{k_1}{2k_2}[\exp(k_2 E_i^2) - 1], \; i = 1, 2 \tag{2.3}$$

where

$$E_i = \mathbf{H}_i : \mathbf{C} - 1, \quad \mathbf{H}_i = \kappa\mathbf{I} + (1 - 3\kappa)(\mathbf{a}_i \otimes \mathbf{a}_i). \tag{2.4}$$

The principal stretches are given as λ_1, λ_2 and λ_3, with directions of the first two indicated in figure 2.1, and the mean collagen fibre direction θ, figure 2.2, in the reference configuration is characterised by unit vectors $\mathbf{a}_i$. Here $\mathbf{a}_1 = [\sin(\theta)\ \cos(\theta)\ 0]$ and $\mathbf{a}_2 = [-\sin(\theta)\ \cos(\theta)\ 0]$ when λ_1 is in the axial direction and $\mathbf{a}_1 = [\cos(\theta)\ \sin(\theta)\ 0]$ and $\mathbf{a}_2 = [-\cos(\theta)\ \sin(\theta)\ 0]$ when λ_1 is in the circumferential direction.

The degree of fibre dispersion is captured by a statistical parameter $\kappa \in [0, \frac{1}{3}]$, where $\kappa = 0$ denotes complete alignment of fibres, while $\kappa = \frac{1}{3}$ implies full dispersion, resulting in isotropy. Additional parameters are μ, the shear modulus, k_1, a stress-like parameter and k_2, a dimensionless parameter. The second order tensors $\mathbf{C}$ and $\mathbf{I}$ are the right Cauchy-Green deformation tensor and the identity, tensor respectively. Additionally, the second order tensor $\mathbf{H}_i(\mathbf{a}_i, \kappa)$ is a general structural tensor for fibre family i. Finally the scalar parameter E_i characterises the strain in the direction of the mean fibre orientation for the i^{th} fibre family.

A fundamental hypothesis of the model is that the collagen fibres do not provide resistance to compressive stresses and simply buckle under compressive loading. This is represented within the model by allowing the $(1-3\kappa)(\mathbf{a}_i \otimes \mathbf{a}_i)$ component of $\mathbf{H}_i$ to be active only when $\mathbf{C} : (\mathbf{a}_i \otimes \mathbf{a}_i) > 1$.

The principal Cauchy stresses may be computed from the strain energy function according to [81]:

$$\sigma_a = -p + \lambda_a \frac{\partial \Psi}{\partial \lambda_a}, \quad a = 1, 2, 3 \tag{2.5}$$

where p is a Lagrange multiplier with the physical interpretation of the hydrostatic pressure. To evaluate σ_1, p must be eliminated from (2.5) using known constraints. First, $\lambda_1^{-1}\lambda_2^{-1} = \lambda_3$ assuming incompressibility. Then, further assuming the collagen fibres have no component in the radial direction so $a_{i3} = 0$. First and fourth invariants of $\mathbf{C}$ and $\mathbf{a}_i \otimes \mathbf{a}_i$ may then be defined as $I_1 = \lambda_1^2 + \lambda_2^2 + \lambda_1^{-2}\lambda_2^{-2}$ and $I_{i4} = a_{i1}^2\lambda_1^2 + a_{i2}^2\lambda_2^2$.

Using these definitions, equation (2.4) may be rewritten as $E_i = \kappa I_1 + (1-3\kappa)I_{i4} - 1$, which yields an expression in terms of the principal stretches:

$$E_i = \kappa(\lambda_1^2 + \lambda_2^2 + \lambda_1^{-2}\lambda_2^{-2}) + (1-3\kappa)(a_{i1}^2\lambda_1^2 + a_{i2}^2\lambda_2^2), \quad i = 1, 2 \tag{2.6}$$

allowing the derivative of (2.5) to be evaluated for Ψ_i^f and Ψ^m. In uniaxial extension in the 1-direction, this will have $\sigma_2 = 0$, allowing p to be obtained from (2.5) as:

$$p = \sigma_2 = \lambda_2 \frac{\partial \Psi(\lambda_1, \lambda_2, \mathbf{a}_1, \mathbf{a}_2)}{\partial \lambda_2}. \tag{2.7}$$

The required first principal stress then becomes:

$$\sigma_1 = \lambda_1 \frac{\partial \Psi(\lambda_1, \lambda_2, \mathbf{a}_1, \mathbf{a}_2)}{\partial \lambda_1} - \lambda_2 \frac{\partial \Psi(\lambda_1, \lambda_2, \mathbf{a}_1, \mathbf{a}_2)}{\partial \lambda_2}, \tag{2.8}$$

wherein the required derivatives are easily evaluated.

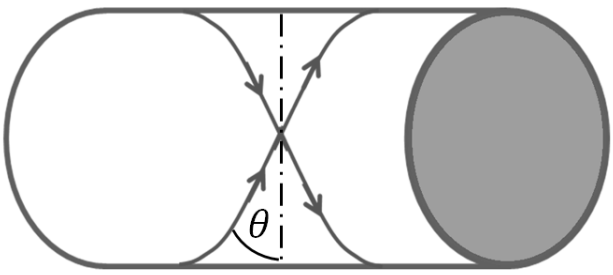

Figure 2.2: Representation of the mean collagen fibre angle θ in the GOH model. The model assumes that two collagen fibre families, with mean orientations indicated by the two arrowed lines, symmetrically encircle the blood vessel wall in a helicoidal manner. In this work, θ is defined with respect to the circumferential direction.

Damage Model

The CDM is incorporated by augmenting (2.1) as:

$$\Psi(\mathbf{C}, \mathbf{H}_i, D^m, D^f) = (1 - D^m)\Psi^m(\mathbf{C}) + (1 - D^f)\sum_{i=1,2}\Psi_i^f(\mathbf{C}, \mathbf{H}_i(\mathbf{a}_i, \kappa)), \tag{2.9}$$

Here $(1 - D^m)$ and $(1 - D^f)$ are known as the reduction factors, with $D^m \in [0, 1]$ and $D^f \in [0, 1]$ being normalised scalars for the matrix and fibre families, respectively, referred to hereafter as damage multipliers [82]. Using (2.9) with standard constitutive continuum mechanical arguments, (2.8) becomes for the damage case:

$$\sigma_1 = (1 - D^m)\sigma_1^m + (1 - D^f)\sum_{i=1,2}\sigma_{i1}^f \tag{2.10}$$

Evolution of the damage multipliers D^m and D^f are characterised by their respective damage criterion Ξ_t^m and Ξ_t^f:

$$\Xi_t^m = \max_{s\in(-\infty,t)}\sqrt{2\Psi^m(\mathbf{C}(s))} \tag{2.11}$$

$$\Xi_t^f = \max_{s\in(-\infty,t)}\sqrt{2\sum_{i=1,2}\Psi_i^f(\mathbf{C}(s))} \tag{2.12}$$

where $\mathbf{C}(s)$ is the right Cauchy-Green tensor at time s.

The damage evolution is characterised by (2.13) with $\xi = (\Xi_t^k - \Xi_{\min}^k)/(\Xi_{\max}^k - \Xi_{\min}^k)$, for $k = m, f$ [83]:

$$D^k(\Xi_t^k) = \begin{cases} 0 & if\ \Xi_t^k < \Xi_{\min}^k \\ \xi^2[1 - \beta^k(\xi^2 - 1)] & if\ \Xi_{\min}^k \leq \Xi_t^k \leq \Xi_{\max}^k \\ 1 & if\ \Xi_t^k > \Xi_{\max}^k \end{cases} \tag{2.13}$$

$\Xi_{\min}^k$ and $\Xi_{\max}^k$ denote critical values of the damage criteria at which, respectively, damage is initiated and completed. $\beta^k \in [-1.0, 1.0]$ is a dimensionless variable that controls the damage profile. The behaviour encapsulated in (2.13) is depicted in figure 2.3.

Curve Fitting

As described in [80], for the uniaxial tension test configuration, the first principal stress may be computed from:

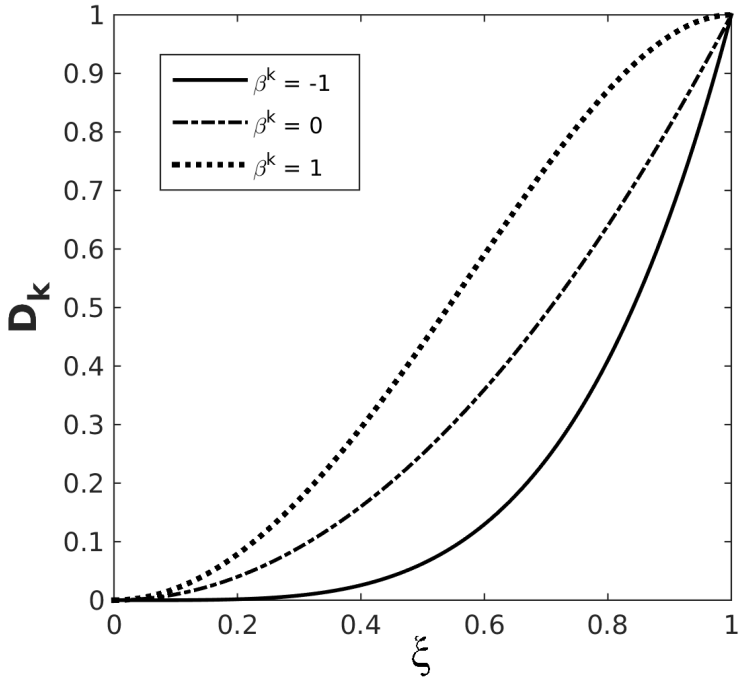

Figure 2.3: The relationship between D^k and ξ in (2.13) for $\beta^k = 1, 0$ and -1. $\xi = 0$ is the point of damage initiation and $\xi = 1$ is the point of complete failure of the material. The plot is limited to $0 \leqslant \xi \leqslant 1$ as this is restricted by equation 2.13.

$$\sigma_1 = \frac{f}{TW}\lambda_1 \tag{2.14}$$

Here f is the measured reaction force, W and T are the initial width and thickness, respectively, and λ_1 is the uniaxial stretch. Fitting of the GOH and CDM parameters to the experimental data was performed using the optimisation toolbox within MATLAB. The fitting procedure was formulated as the optimisation problem described in (2.15):

$$\mathbf{x} = \underset{\mathbf{x}}{\arg\min} \left\{ w_1 ||\sigma_1^{exp} - \sigma_1^{mod}||_2^{axial} + w_2 ||\sigma_1^{exp} - \sigma_1^{mod}||_2^{circ} \right\} \tag{2.15}$$

Here $\mathbf{x}$ is a vector of model parameters, σ_1^{exp} are experimentally measured first principal Cauchy stresses (vector of values, measured over the course of the experiment), computed using (2.14), and σ_1^{mod} are the corresponding model-predicted stresses, computed using (2.10). w_1 and w_2, are weighting parameters, manually tuned to achieve best fit, $||\cdot||_2$ denotes the 2-norm and "axial" and "circ" pertain to data derived from axial and circumferential specimens, respectively.

To improve optimisation time and robustness, GOH model parameters were found separately from damage parameters. This was done by fitting to the experimental

data up to the estimated point of damage initiation, identified through inspection of experimental data. CDM parameters were then optimised over the whole data set with the previously found GOH parameters.

To reduce the computational cost and robustness of the optimisation procedure, several parameters were either assigned literature values or deduced by inspection. Initial tests found that if κ is included in the optimisation procedure then the best fit to data from any treatment type will always have $\kappa \approx 0.3$ which is not representative. Therefore, to ease computational cost κ was set to the value in [26]. However, cross-linking was represented in 2.3 by κ and fixing this results in any differences resulting from cross-linking to be accounted for by other parameters. The shear modulus μ was fixed at 3 kPa (based on initial tests and values found in previous studies [80]), as initial tests revealed that altering it had little effect on the overall behaviour at the large stretches seen here, where the exponential fibre terms dominate. Correspondingly, the matrix component of the CDM was also omitted thereafter. Prior experiments showed that removing this component of the CDM had little effect on results because of the relatively small influence of 2.2 on the GOH model behaviour at large strains where 2.3 dominates. Fibre damage parameters $\Xi^f_{\min}$ and $\Xi^f_{\max}$ were estimated according to: $\Xi^f_{\min} = \sqrt{2\sum_{i=1,2}\Psi^f_i(\lambda^I_1)}$ and $\Xi^f_{\max} = \sqrt{2\sum_{i=1,2}\Psi^f_i(\lambda^F_1)}$, where λ^I_1 and λ^F_1 are stretches at which damage initiated and at which complete failure of the specimens occurred, respectively. These stretches were estimated by direct inspection of the experimental curves. Therefore, the remaining constitutive parameters estimated during the fitting procedures are as summarised in table 2.2.

Table 2.2: The constitutive parameters being found during each optimisation. θ is the collagen fibre angle.

Elastic (GOH) parameters	Damage parameter
k_1	β^f
k_2	
θ	

There are multiple ways in which model parameter fitting to the experimental data can be approached. A possible solution is to fit to each data set independently, then average the parameters for the constitutive model to give the overall behaviour in each direction. This method is computationally costly and as Roberson and Cook have shown, averaged constitutive parameters are not guaranteed to represent average behaviour [84]. In this work, therefore, the model was fit to averaged curves only, and to both directions simultaneously (as described by (2.15)). However, while this approach is less expensive, the fitted parameters are restricted to the average curves and are not representative of the whole data.

A particle swarm optimisation procedure was utilised [85]. This global optimisation method operates by selecting multiple starting points, known as particles. This

is advantageous as it reduces optimum solution dependence on the starting parameters, which is otherwise a common occurrence when fitting hyperelastic constitutive models [86]. The movement of each particle is governed by simple mathematical formulae describing the particle's position and velocity. Each particle's movement is influenced by its local best known position, but also by the progress of other particles, as they find better positions elsewhere in the search space. This moves the swarm to the best solution whilst not being reliant on the gradient of the search space, unlike the commonly used nonlinear least squares algorithm. This allows it to find an approximate minimum despite the irregular search space that is present here. An alternative approach for removing dependence on starting parameters is to use a multi-start algorithm with a non-linear optimiser such as non-linear least squares [87]. Here multiple least squares optimisation procedures are run independently with different starting points. This can be thought of as a single particle governed by more complex rules that attempts to find a minima from different starting points with no information on prior attempts from other starting points. This was tested and compared to a particle swarm optimisation and particle swarm was found to be more accurate. Once the particle swarm optimisation has concluded, a least squares optimisation algorithm is called, beginning at the best known location from the swarm, to further refine the solution. Finally, upper and lower bounds were imposed on the model parameters to limit the search space of the optimiser and ensure physical plausibility.

2.3 Results

2.3.1 Mechanical Tests

The observed stress responses up to fracture of the tested specimens are shown in figures 2.4 and 2.5. Overall large variation in results are present, however statistically significant differences, assessed via the Student's unpaired t-test [4], in fracture behaviour can be seen (table 2.3). A summary of salient features of these responses for the various categories of specimens follows:

Circumferential versus axial specimens. Circumferential specimens displayed higher fracture stress ($p<0.05$ for all samples) while axial specimens have higher fracture stretches ($p<0.05$ for all samples). An additional trend seen in both control samples and glutaraldehyde samples is the fragmented response under loading in the axial direction: the curves show some flattening and dips associated with minor localised failure before final fracture.

Control versus 20 hour control (20hC) specimens. Samples from both groups show similar behaviour with minor changes in fracture stress and stretch that are not significantly different ($p \not< 0.05$).

Control versus collagenase specimens. Collagenase circumferential results are

Table 2.3: Fracture stress and stretch values (mean ± standard deviation), and results of Student's unpaired t-test between control and treated samples [4]. Data shown for fresh porcine aorta samples (control), samples incubated in saline solution at 37° C for 20 hours (20 hour control), collagenase treated samples, elastase treated samples and glutaraldehyde treated samples.

(a) Axial specimens.

Fracture Stress (MPa)				
Control	Control 20 hours	Collagenase	Elastase	Glutaraldehyde
1.3 ± 0.41	1.33 ± 0.45	0.79 ± 0.37	1.48 ± 0.72	1.17 ± 0.477
-	n.s.	$p<0.05$	n.s.	n.s.
Stretch in 1st Principal Direction at Fracture				
Control	Control 20 hours	Collagenase	Elastase	Glutaraldehyde
1.84 ± 0.18	1.83 ± 0.24	2.10 ± 0.26	2.09 ± 0.29	1.77 ± 0.29
-	n.s.	$p<0.05$	$p<0.05$	n.s.

(b) Circumferential specimens.

Fracture Stress (MPa)				
Control	Control 20 hours	Collagenase	Elastase	Glutaraldehyde
2.7 ± 0.61	2.96 ± 0.68	2.36 ± 1.01	4.35 ± 1.03	2.95 ± 0.74
-	n.s.	n.s.	$p<0.05$	n.s.
Stretch in 1st Principal Direction at Fracture				
Control	Control 20 hours	Collagenase	Elastase	Glutaraldehyde
1.6 ± 0.09	1.62 ± 0.09	1.73 ± 0.16	1.72 ± 0.09	1.63 ± 0.10
-	n.s.	$p<0.05$	$p<0.05$	n.s.

more scattered, with less well defined peaks and some evidence of localised failure before the final fracture. Furthermore, the stretch at which fracture occurs is greater ($p<0.05$), the curves showing an overall shift to the right. However, the fracture stress is only marginally lower (no statistical significance). In the axial direction, the collagenase specimens are far less stiff, with a lower fracture stress ($p<0.05$) and higher fracture stretch ($p<0.05$).

Control versus elastase specimens. Elastase treated samples show an increase in fracture stress and stretch in both directions. However, in the axial direction, only the stretch is significantly different ($p<0.05$), whilst in the circumferential direction both the fracture stress and stretch are significant ($p<0.05$). The highest fracture stretches (approximately 2.8) across all treatments can be seen here in the axial direction.

Control versus glutaraldehyde specimens. Glutaraldehyde samples in the circumferential direction show a higher spread in fracture stress, but similar fracture stretches, with differences less stark than in the collagenase treated samples. While in the axial direction, the fracture stress and stretch are similar to the control samples, but the already fragmented fracture behaviour is now further exaggerated, with damage initiating earlier.

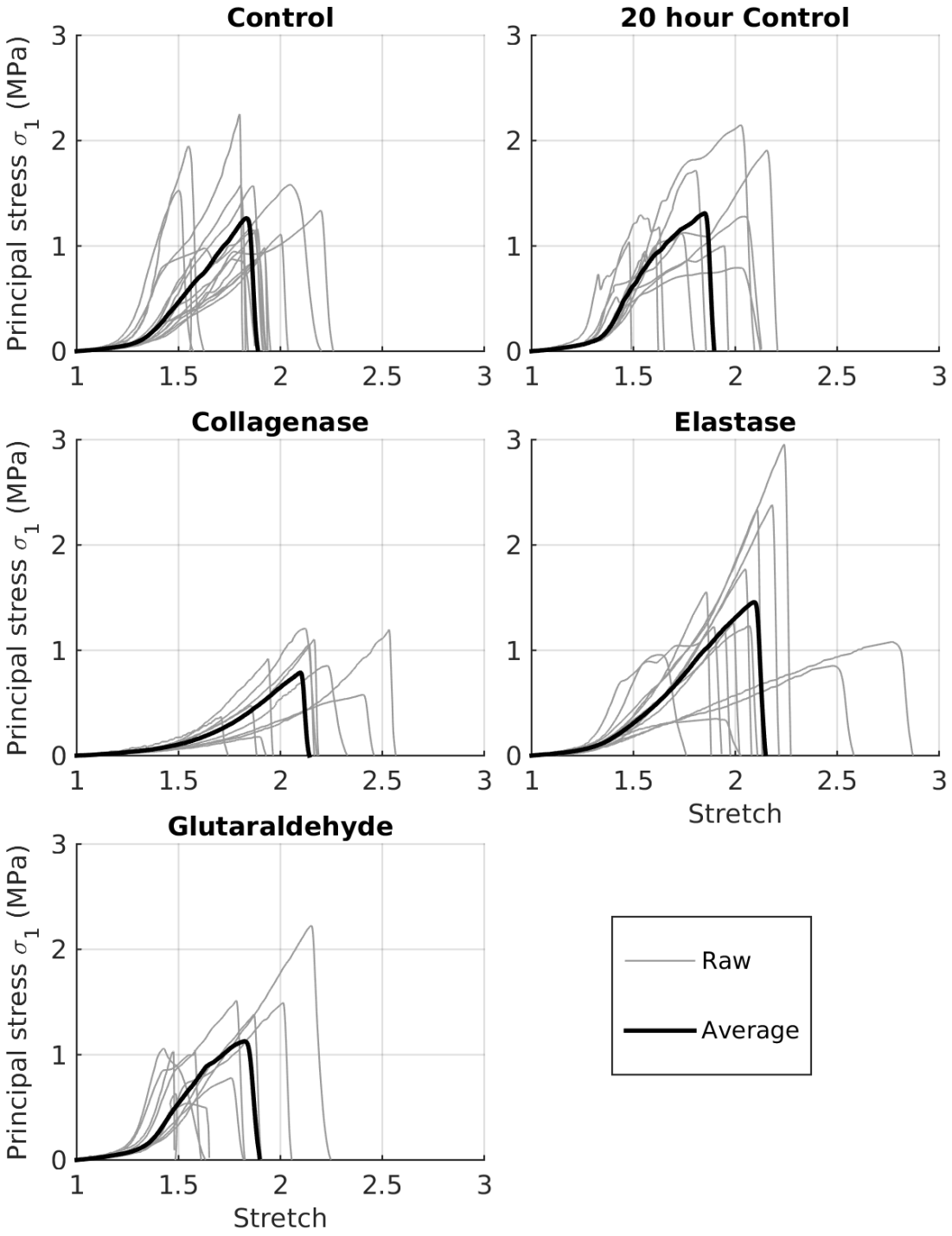

Figure 2.4: *Axial specimens.* First principal Cauchy stress versus stretch for the fresh porcine aorta samples (control), samples incubated in saline solution at 37° C for 20 hours (20 hour control), collagenase treated samples, elastase treated samples and glutaraldehyde treated samples. Raw experimental curves overlaid with averaged curves in all cases.

Reliability of data. While every effort was made to ensure the data was accurately and reliably recorded there are inevitably sources of error. As previously mentioned, tests were conducted in open air and some sample drying may have occurred despite efforts to minimise this. Additionally, while samples were digested in the same

controlled conditions, it is likely that the magnitude of enzyme digestion will have varied between samples and within samples also and will have been difficult to detect and quantify. Finally, there will have been variations in the mechanical response between animals and at different locations along the descending thoracic aorta. Therefore, results must be interpreted with caution, specifically the fracture behaviour must be considered for the test conditions here when comparing to other data. However, the relatively large sample size and identical test conditions between the groups results in the comparisons between samples being valid.

2.3.2 Curve Fitting

The resulting GOH parameters are given in table 2.4a. Glutaraldehyde treated samples yielded the highest k_1, with collagenase values significantly lower than all others. All treatments resulted in substantially lower k_2 values than for the controls, with elastase specimens yielding the lowest. Finally the collagen fibre angle is lowest for collagenase but highest for elastase samples, though the difference is small: $< 4^{o}$.

Table 2.4: GOH and CDM parameters estimated from experimental data.

(a) Fitted GOH model parameters.

Sample	k_1(kPa)	k_2	θ (Degrees)
Control	143	4.45	40.8
Collagenase	66.0	2.23	37.3
Elastase	222	1.77	38.7
Glutaraldehyde	283	2.54	41.1

(b) Damage parameters found by identification, alongside fitted β_f parameter.

	Axial			Circumferential		
Sample	$\Xi^f_{\min}$	$\Xi^f_{\max}$	β^f	$\Xi^f_{\min}$	$\Xi^f_{\max}$	β^f
Control	233	897	0.84	585	659	0.08
Collagenase	229	599	-0.03	530	823	0.71
Elastase	351	970	0.70	835	944	-0.75
Glutaraldehyde	296	995	0.82	680	797	-1

(c) Correlation coefficients (r^2) for the whole fitted curves compared to the experimental data.

Sample	r^2 axial	r^2 circumferential
Control	0.85	1.00
Collagenase	0.90	0.99
Elastase	0.86	0.99
Glutaraldehyde	0.90	0.98

The damage parameters were also sought from the averaged curves, but $\Xi^f_{\min}$ and $\Xi^f_{\max}$ were found to be different in the axial and circumferential directions (table 2.4b). Additionally trial experiments showed that fitting β^f to both directions

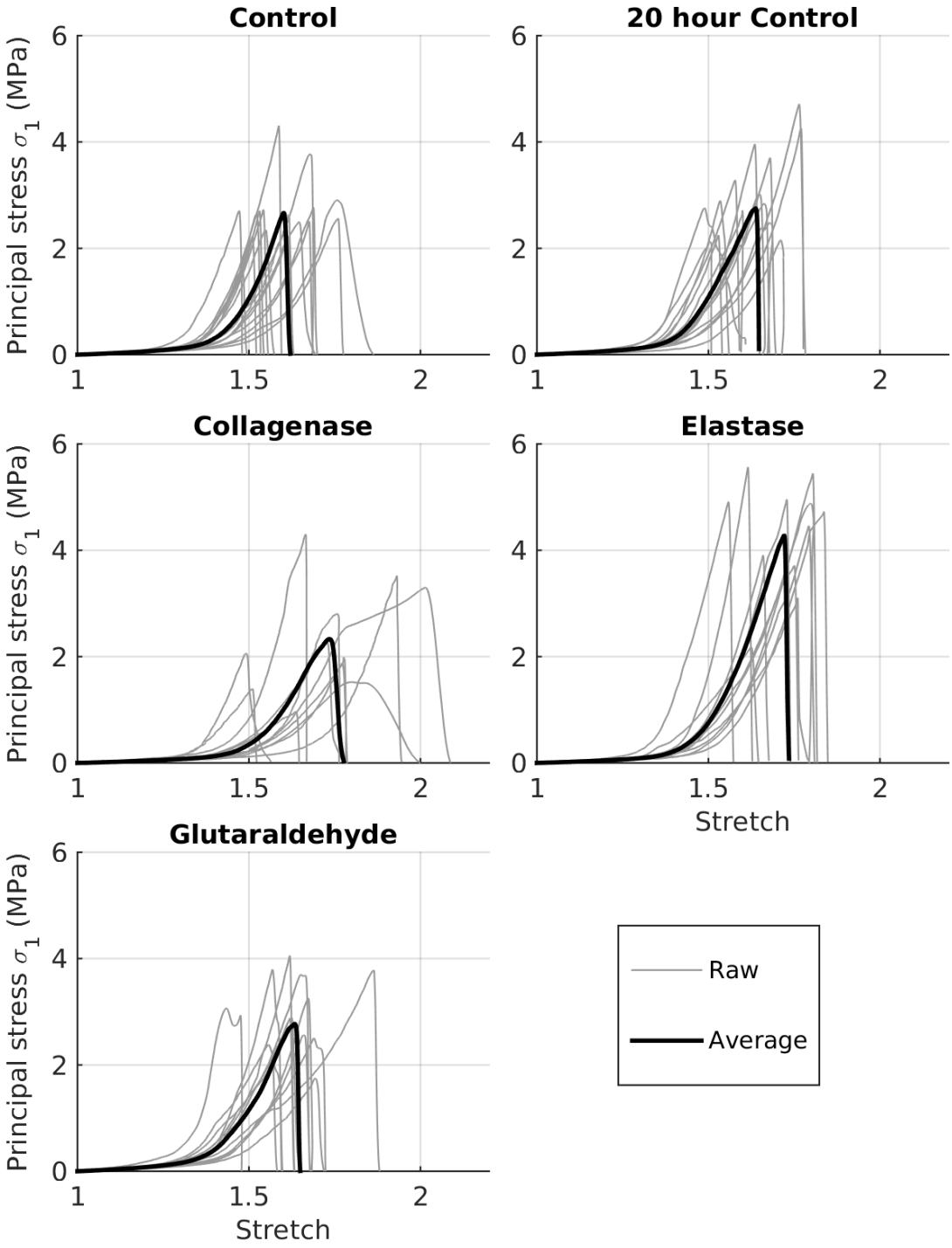

Figure 2.5: *Circumferential specimens.* First principal Cauchy stress versus stretch for the fresh porcine aorta samples (control), samples incubated in saline solution at 37° C for 20 hours (20 hour control), collagenase treated samples, elastase treated samples and glutaraldehyde treated samples. Raw experimental curves overlaid with averaged curves in all cases.

simultaneously produced poor fits and so the damage parameters were fit to each direction separately. This may reflect differing fracture behaviour in the axial and circumferential directions. Collagen fibres are closely aligned with the circumferential direction, thus, when a sample is pulled to failure the collagen fibres have reached

their tensile limit and snap. By contrast in the axial direction the collagen fibres partially align themselves to bear the load and cross-links between fibre families also play a larger role in the tensile behaviour. Thus, it is likely that at fracture fibre families are pulled apart from one another as well as whole fibres snapping, leading to more gradual fracture behaviour.

The damage parameters so obtained are given in table 2.4b. For Ξ^f_{min} and Ξ^f_{max} in the axial direction, glutaraldehyde samples produced the highest spread (highest Ξ^f_{max} but third lowest Ξ^f_{min}). Collagenase shows the lowest spread with the lowest Ξ^f_{min} and lowest Ξ^f_{max}. The optimised value of β^f is highest for control samples, but varies greatly, with collagenase samples showing the lowest.

In the circumferential direction, collagenase produced the highest spread between Ξ^f_{min} and Ξ^f_{max}, with the lowest Ξ^f_{min} and second highest Ξ^f_{max}, whilst the control samples produced the lowest spread. Interestingly, Ξ^f_{min} for elastase is greater than Ξ^f_{max} for all other samples. β^f is lowest for glutaraldehyde and highest for collagenase. The collagenase experimental data and the fitted curve show the slowest progression to failure, which coincides with the highest spread between damage terms, Ξ^f_{min} and Ξ^f_{max}.

The overall quality of the fits is assessed by the coefficient of determination r^2 measure (table 2.4c). The fits in the circumferential direction were all of high quality, with $r^2 \geq 0.97$, but especially in the control samples where, in figure 2.6, the experimental and fitted data are almost indistinguishable. Poorer fits were obtained for axial data, with control data yielding the weakest fit ($r^2 = 0.850$). The resulting model-predicted curves are shown in figure 2.6.

Comparing between directions it can be seen that the spread of the damage terms is overall higher for the axial direction. This is reflected in the curves as a more gradual progression to failure for the axial data, whereas the circumferential data show a sharper progression (figure 2.6).

2.4 Discussion

2.4.1 Mechanical Tests and Effects of Digestion

Results from uniaxial tests generally coincide with the anisotropic behaviour seen elsewhere [88, 89, 78]. The stiffer behaviour in the circumferential direction is greater because of greater alignment with the stiffer collagen fibres. This in turn leads to a greater fracture stress in the circumferential direction. The difference in fracture stretch is likely due to the high stress in the circumferential direction, such that once the tensile strength of collagen has been reached the elastin and surrounding matrix also breaks. Whereas the stress in the axial direction is far lower, the increasing slope of the curves suggests that collagen is still the major contributor to the behaviour at high stretch. The alignment of fibres could also explain the fragmented fracture

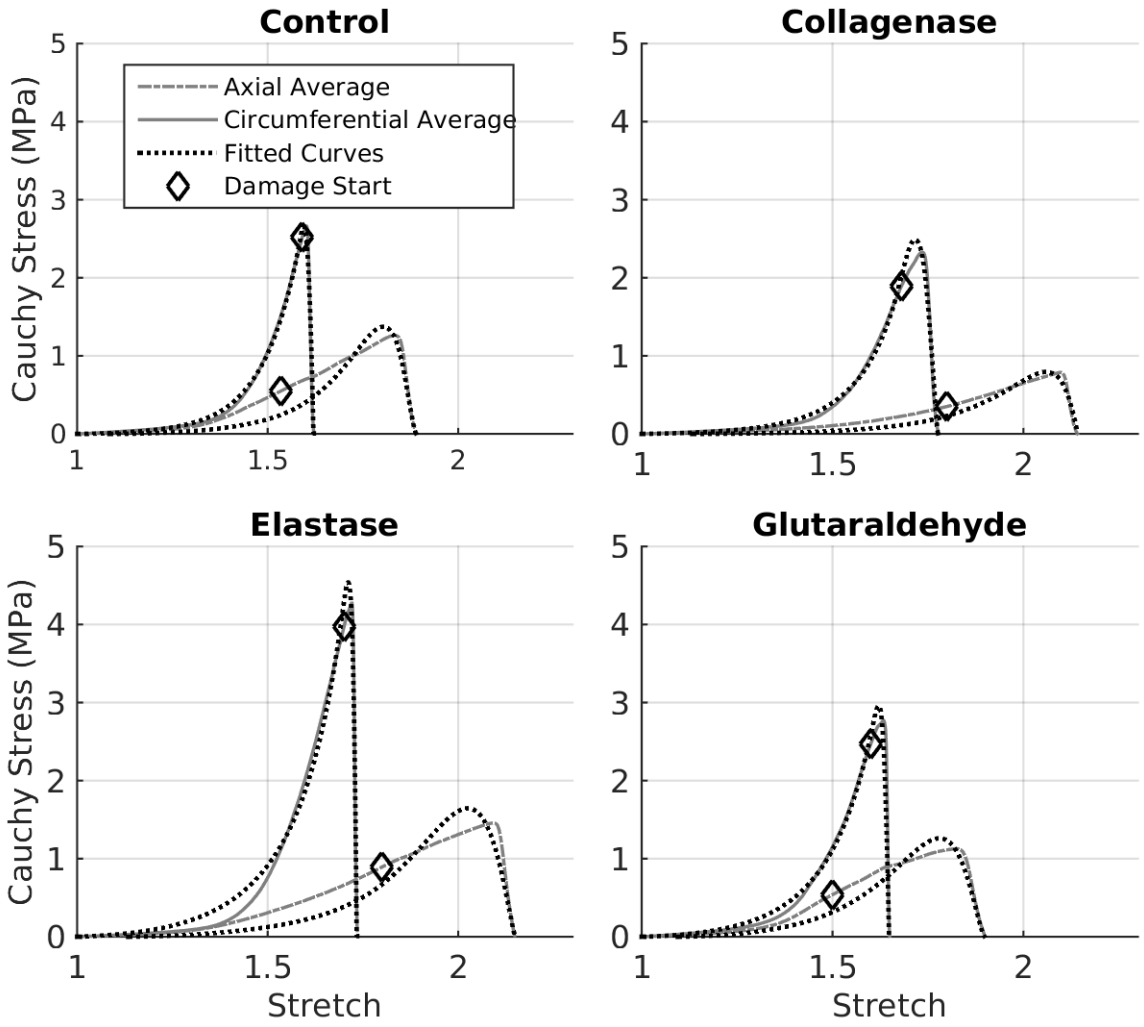

Figure 2.6: Average stretch versus Cauchy stress with curve fits overlaid. Diamonds mark the points at which damage was assumed to initiate. Non-damage parameters were fitted to the curve regions prior to these points.

behaviour seen in the axial direction, as the drops could be associated with fibres families pulling apart, rather than breaking outright .

The magnitude of the stress in the control samples is higher here than reported in other publications [90]. However, a possible explanation is that preconditioning was performed up to 15 mm and samples were extended further than this when stretched to failure. Thus the region between 15 mm displacement and failure will show greater time-dependent behaviour and it has been previously shown that loading rate affects the failure stress and stretch [91, 92, 93]. Nevertheless, all tests were performed under the same conditions and as such all comparisons between treatment types remain valid.

The variation in the curve profiles and fracture behaviour may be attributed to structural variations between individual animals and anatomical locations. The latter in particular may have had a large effect despite only selecting upper thoracic aorta proximal to the heart to ensure adequate tissue thickness. Different sections of the thoracic aorta have differing structure and properties further from the heart

due to the differing flow environments and so care must be taken to ensure arteries from similar locations are tested to avoid variation in behaviour resulting from this [26, 94]. Finally, the difference in thickness of the samples, may affect the extent of digestion. Despite the samples being incubated for 20 hours, thicker samples will require longer for the enzymes to permeate to the centre and thus thinner samples would be expected to be more digested [95].

Collagenase treatment

The effect of collagenase digestion on wall compliance varies in the literature. Dobrin and coworkers found that there was no change in axial compliance with collagenase treatment, contradicting the results of this study [96, 97]. However Gundiah et al. found collagenase treatment affected wall compliance in both directions, which supports the findings here [42]. The differences in behaviour in this study are most pronounced in the axial direction, with both the fracture stress and stretch being significantly different, whilst only the stretch is significantly different in the circumferential direction. This is an unexpected result because it has been shown the collagen fibres in the intima and media are more aligned with the circumferential direction (albeit marginally so in the intima). Differences in fracture properties would therefore be *most* expected in this direction [26].

It is perhaps explained by the relationship between elastin and collagen in the arterial wall: detachment of collagen from elastin fibres in the axial direction may lead to collagen fibres not being recruited and thus the flat, highly extensible behaviour in the axial direction. The digestion may have been insufficient to alter the fracture stress in the circumferential direction, but enough to cause collagen to detach from the elastin fibres in the axial direction. Many of the curve profiles in the circumferential direction have lost the smooth behaviour seen in the control study, and instead show a disrupted shape which may reflect disruption of the collagen fibre network.

Elastase Treatment

The behaviour resulting from elastase treatment is mostly different from that reported in other publications, where elastin digestion instead is reported to result in a loss of compliance and an immediate collagen-related stiffening [98, 39]. However, Chow et al. have shown that partial digestion of elastin tends to increase the compliance of the tissue, which would support the increased fracture stretch [41]. They describe the increased compliance region followed by a sudden stiffening as the "extensible but stiff" region, which shows varying initial compliance depending on the amount of elastin degradation and which is also supported by other studies [78, 99]. However, to the author's knowledge, no study examined the tensile behaviour of elastase treated artery up to failure, and so speculation as to the causes of this behaviour is difficult. However, it is interesting to note the behaviour of the average elastase treated sample

in the circumferential direction when compared to that of the 20hC and control samples (figure 2.7). Despite a slight shift to the right and an increase in fracture stress/stretch, the elastase curve follows a similar profile to the two control curves. A possible reason is that this is an innate response of the tissue to elastin loss/damage. Loss of elastin leads to the alteration of collagen and elastin interconnectivity such that collagen bears more of the load and the fracture stress increases. This acts to shield the remaining elastin from further damage whilst further protecting the vessel from rupture. A possible means of analysing this proposed explanation would be to use electron microscopy to view the collagen and elastin fibre interconnectivity and any associated changes before and after treatment.

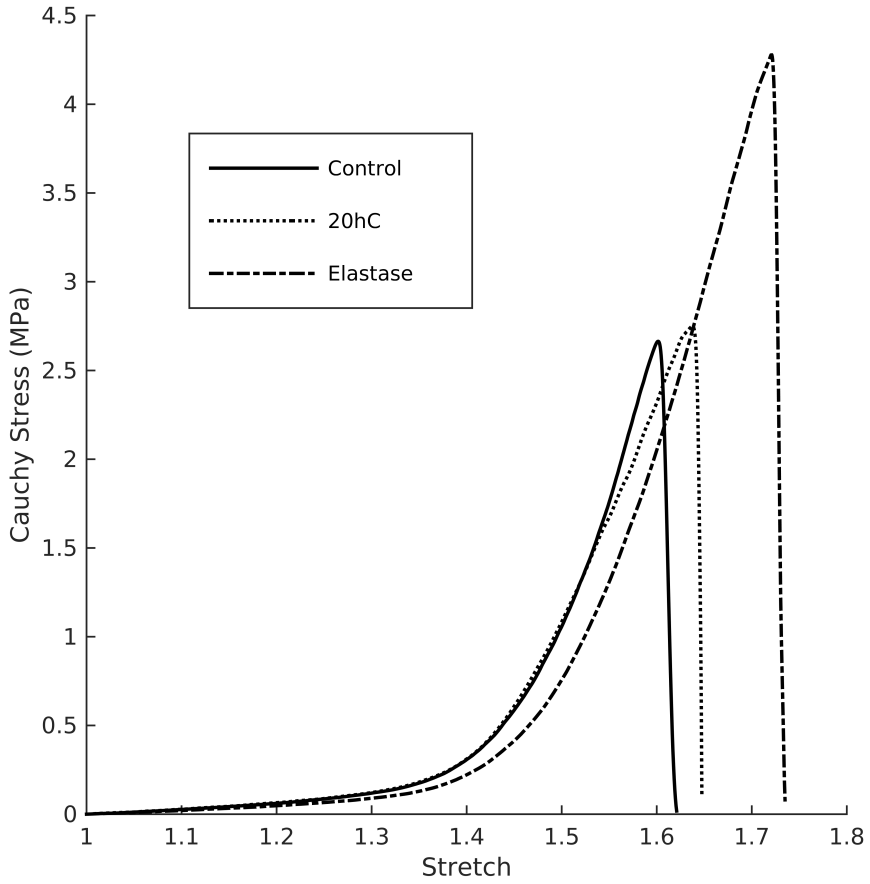

Figure 2.7: Direct comparison of control and 20hC average data with elastase average data in the circumferential direction.

Glutaraldehyde Treatment

The ability of glutaraldehyde to cross-link and stiffen proteins has been exploited for various applications and is widely used for fixing biological samples for histological examination [100, 101, 102]. This capability has been suggested elsewhere for altering mechanical properties of vascular grafts to match those of the host [103, 104]. These

studies found an increase in stiffness and tensile strength with treatment, which was not evident here despite treatment concentrations and durations being similar. Despite this, an increase in fragmented behaviour in individual curves compared to the control samples in the axial direction can be observed. It is possible that at this concentration, the treatment is most effective on cross links between existing fibre bundles, causing existing links to become more brittle, and easing the separation from one another of fibre bundles.

2.4.2 Parameter Fitting and Effects of Digestion

Quality and Reliability of the Fits

Comparison of the quality of the curve fits in circumferential and axial directions (figure 2.6) suggests that this overall model is best suited for smooth, continuous breaking. The poorer quality of the curve fits in the axial direction can be partially attributed to the fragmented and discontinuous curve profile, which is likely because of pulling against the main fibre orientation [91]. Similar effects have been observed in other failure tests such as peel testing [46].

However, an additional reason stems from the nature of the GOH model at high stretches. The GOH parameters that gave the best fit to the non-damage portion of the axial experimental curve, produce very large stress at the failure stretch. If the stress from the GOH model at the failure stretch was too high, the damage model could not reduce this stress sufficiently to produce a good fit to the experimental data. By adjusting the fitting procedure to reduce the gradient of the elastic portion of the curves, this large stress was reduced and the overall fit to the experimental data improved. This is reflected in all of the model curves for axial direction specimens: the model underestimates the stress until relatively close to the failure point, when it briefly switches to overestimation. The effects of this modification to the fitting of the GOH parameters can be seen when comparing figure 2.7 to the fitted GOH parameters in table 2.4a. Despite the very similar curve profile in the control and elastase treated samples, the fitted GOH parameters are very different. This is because there are multiple suitable candidate solutions for the circumferential direction that will yield equally good overall r^2 values to those seen here; that is, the model over fits the data. Fitting to the axial direction simultaneously reduced the number of candidate solutions and produced parameters that better represented the *overall* tissue behaviour. On the other hand, modifying the fitting procedure to achieve a better fit in the axial direction may also diminish the physical insight that can be derived from the resulting parameter values.

2.4.3 Diseased Tissue Comparison

Two of the most prevalent and widely explored arterial diseases are atherosclerosis and aneurysm. He and Roach investigated the composition and mechanical properties of abdominal aortic aneurysms [105]. They stained the aortic wall to identify collagen fibres in histology and performed uniaxial tension tests in the axial direction. It was found that elastin and smooth muscle cell volume fraction decreased by approximately an order of magnitude compared with healthy tissue, whilst collagen volume fraction nearly doubled. Their tensile test data, correspondingly, showed increased stiffness in diseased tissue and curves shifted towards lower strains. This behaviour coincides with results reported in Gundiah et al. when elastin was artificially degraded [42]. However, it was not reflected in the results of this current study, wherein curves for elastase treated samples showed a shift towards higher strains. It could be speculated that to emulate the mechanical properties of aneurysm tissue, greater elastase digestion is necessary. Additionally, subsequent glutaraldehyde treatment may further emulate the increase in collagen volume, as the remaining collagen will be heavily cross-linked by this means.

Comparing failure behaviour, Raghavan et al. performed uniaxial tension tests on ruptured and unruptured human abdominal aorta aneurysms in the axial direction [106]. The mean failure stress for unruptured aneurysms (0.95 ± 0.28 MPa) is similar to results reported here for all sample treatment types, but is closest to the values for glutaraldehyde and collagenase treated samples. However, the failure stretch in that study (1.39 ± 0.09) is far lower than for all sample treatment types here. A possible explanation for this disparity is that the tissue investigated in that study is in the late stages of the aneurysm disease process. The treatments applied here were intended to partially degrade or cross-link collagen and elastin fibres, thus greater treatment time or concentration may allow the tissue to more closely emulate later stages of the aneurysm disease process, specifically.

One of the most complete investigation into changes in arterial wall mechanics in atherosclerosis was performed by Holzapfel et al. [107]. Here, uniaxial tension results from atherosclerotic intima and media from iliac arteries were compared with those of intima, media and adventitia from non-diseased sites. The results showed a pronounced difference in the media when stretched in the circumferential direction, with steeper curves and a higher ultimate tensile stress, despite the stretch at failure being much lower. In the axial direction the difference was far less clear and there seemed to be little difference between diseased and non-diseased media. The higher fracture stress in the circumferential direction coincides well with the results seen here for elastase treated samples, however the lower fracture stretch does not. Closer approximation of this behaviour might be achieved with further elastase digestion or a combination of elastase digestion and glutaraldehyde treatment, as suggested previously.

Failure behaviour of atherosclerotic coronary artery was investigated in [108]. Axial and circumferential samples were stretched to failure and the failure stress and stretch were reported. The axial failure stress (Cauchy stress approximately 0.73 ± 0.38 MPa) was similar to the value reported in the present study for collagenase treated samples. Circumferential failure stress (Cauchy stress approximately 1.80 ± 0.78 MPa), while similarly closest to the present value for collagenase samples, was nonetheless substantially lower. Axial failure stretch was considerably smaller (1.40 ± 0.18) than for any treated samples here. Circumferential failure stretch (1.47 ± 0.25) was most like control, 20hC and glutaraldehyde sample values in this study but still much reduced. Longer treatment times may aid in reducing the circumferential fracture stress and fracture stretch in both directions. However, the true effects of the atherosclerotic plaques would likely *not* be confined to alterations in the elastin and collagen networks, and this could also explain the differences observed.

2.4.4 Limitations

Mechanical testing in this study was performed at room temperature and in open air, whilst many other studies performed tensile tests within a saline bath. It has been previously mentioned in Section 2.2.1 that this was to allow for accurate recording of sample stretch. However, methods similar to those employed by Loree et al. with a saline drip at 37°C may yield results with more physiological relevance [109].

To ensure complete removal of the adventitia an incision was made midway through the arterial through-thickness. This involved removing more tissue than was likely necessary and removal of the adventitia could not be certain. This may have effected the variation in mechanical properties between samples as more adventitia may be remaining on some samples than others where it was completely removed. Imaging techniques such as histology would aid in verifying whether this technique did indeed fully remove the adventitia and should be utilised in future studies [94].

Further physiological relevance could also be achieved with biaxial loading, which more closely reflects the *in vivo* loading conditions [110, 8, 111]. However, there are practical difficulties associated with using biaxial testing at high loads present in this study [94], and doing so may yield poor estimates of stress [112, 113]. Thus it is ill-suited to investigation of failure behaviour.

The GOH constitutive model was chosen due to its wide use for capturing arterial wall mechanics. Despite using a relatively thin layer of tissue, a gradient of enzyme penetration must persist, meaning superficial regions will be more digested than interior ones. A constitutive model that incorporates different layers may accordingly enable the depth-dependence of mechanical properties that must accompany this gradient to be captured.

Additionally, while the GOH formulation has been shown to model well the tissue response in physiological strain ranges, the exponential fibre term may not be suitable

outside this range, where it appears the collagen fibres transition from exponential to more linear behaviour [114]. A modified strain energy function that emulates the GOH response for moderate strains, but approaches linearity nearer to failure strains may thus be more widely applicable. Finally the applicability of the GOH model to arterial wall that has undergone enzymatic digestion has not been established; enzyme treatment may drastically alter fibre properties such that the underlying assumptions of the model may no longer be valid; and further investigation of this matter is required.

2.5 Conclusions

The main goal of this study was to investigate the effect of removing and altering constituent proteins of thoracic aorta on the mechanical response with respect to disease processes. To this end, porcine arteries were treated with collagenase and elastase concentrations that allow for partial breakdown of constituent proteins to emulate the mechanical property changes that accompany disease. In addition, arteries were treated with a weak glutaraldehyde solution to induce minor cross-linking, similar to that seen in some in arterial diseases. Collagenase treated samples did not show significantly different fracture stresses from controls in the circumferential direction, but in the axial direction the difference was significant. Conversely, elastase samples showed a significant increase in fracture stress in the circumferential direction, but no significant difference in the axial direction. Glutaraldehyde samples showed no significant difference in either direction. Axial direction curve profiles were, however, significantly changed by this treatment, showing more fragmented behaviour and damage initiating sooner.

To draw out quantitative comparisons to the curve profiles the commonly utilised GOH model was combined with a continuum damage model and fit to the experimental data. Both enzymatic treatments had a strong effect on fibre-related model terms, but only collagenase results suggested a strong change in fibre orientation. This model was best suited to circumferential data due to the smoother transition from damage initiation to complete failure.

Finally, as mentioned in the Introduction, disease processes are complex and multifaceted, and simple enzymatic digestion provides only an approximation of the various chemical, physical and cellular processes taking place within the arterial wall during, for example, aneurysm formation. Therein loss of elastin, and the accompanying increase in wall compliance, stimulates cellular mechanotransduction and, in turn, complex remodelling of collagen components [16]. Wall mechanics in atherosclerosis are yet more complex due to the presence of the atherosclerotic plaque which, despite efforts to capture its mechanical properties, is exceedingly difficult to incorporate into healthy arteries *ex vivo* with many studies opting to induce the

process *in vivo* [115, 116]. The physiological complexity of real disease processes notwithstanding, the aim of this chapter was to produce a physical model of diseased arteries that effectively emulates the accompanying changes in their mechanical properties only. However, as mentioned in section 2.4.3, judicious combination of any or all of these treatments could in principle be used to effect the changes observed in a particular disease.

Chapter 3

Controlled peel testing of a model tissue for diseased aorta

3.1 Introduction

Arterial dissection refers to separation of the inner layers of the arterial wall. This is almost always initiated by trauma, either directly to the vessel wall, e.g. a catheter piercing or tearing the intimal layer of the vessel during an endovascular procedure [22], or indirectly via external trauma, for instance from motor vehicle crashes [23]. Depending on the direction of blood flow, the circulatory pressure will either press the tissue flap to the wall or act to propagate the dissection (figure 1.5). The former often results in the dissection remaining benign, whereas the latter can eventually progress to create a large tissue flap that blocks downstream blood flow in the true lumen and encourages flow into the newly formed false lumen between the flap and remaining artery wall. In large arteries this is often fatal: mortality rates for aortic dissections are reported to be 50% [117].

The increasing use of endovascular treatment methods renders desirable the development of new medical devices such as endovascular catheters. Research in this area requires access to large supplies of arterial tissue - preferably diseased, to reflect the state of real patient tissues - for physical testing of designs. But, accessing human diseased tissue is costly and has numerous ethical and legal implications. In chapter 2 porcine arterial tissue, processed with a suitable combination of enzyme solutions, was proposed as a model of diseased human tissues for use in such developments. Various enzymatic treatments were explored as a means of emulating the effects of diseases on the mechanical properties. Correspondingly, the effects of collagenase, elastase and glutaraldehyde treatments on the uniaxial elastic and failure behaviour of arterial tissues were investigated. In the present chapter, these results are expanded upon by investigating the effects of these treatments on dissection resistance. More specifically, the mode 1 critical energy release rate (G_c), as a measure of the strength of the tissues, is compared before and after treatment with each of the mentioned solutions. The low cost and ready availability of porcine arterial tissue (often considered a waste product in meat preparation), and avoidance of aforementioned ethical issues, suggests tissue models produced in this way can ameliorate the cost and complexity of medical device design.

The media of the arterial wall is most prone to dissection, as a result of its organisation into lamella units, stacked on top of one another [24]. These lamellae are primarily composed of fibres of rubber-like elastin and stiffer collagen, and smooth muscle cells. These constituents, moreover, are orientated predominantly within planes tangential to the vessel axis, and with a bias towards circumferential directions over axial [25]. This organisation in turn imparts the highest mechanical strength in circumferential directions, somewhat lower strength in axial directions, and significantly lower strength in radial directions [26, 27]. This can be seen in figure 1.6.

Various diseases are associated with higher susceptibility to arterial dissection. For

individuals with Marfan's syndrome the most common cardiovascular complication is enlargement of the ascending aorta, often leading to aortic dissection [118]. This is caused by a mutation to the fibrillin-1 glycoprotein which in turn affects elastin protein structure in the thoracic aorta, resulting in a weakened arterial wall [38]. A further disease linked to increased dissection incidence is Ehlers-Danlos syndrome, which is associated with a mutation in the gene coding for collagen III. This again leads to weakened arterial walls, with rupture or dissection the most common form of death [119, 120]. It was also speculated that low collagen content related to post-partum hormonal imbalance is associated with instances of arterial dissection [121]. Additionally many cases of dissection accompany aneurysm formation and this is again linked to a change in the structure of both elastin and collagen [122, 105, 123]. Finally, there is also experimental evidence for diminution of vessel strength (specifically, aorta) associated with these diseases, which could explain this higher susceptibility [124, 46].

Enzyme digestion has been utilised previously to alter arterial mechanical properties. Treatment with collagenase or elastase was applied to reduce or remove the respective proteins, and the resulting changes in mechanical response were investigated via uniaxial, biaxial or inflation testing [43, 39, 42]. However, little investigation of the effects on failure behaviour of the tissues, such as during dissection, has been performed. Those studies that have been performed were concerned with tensile failure modes [45, 65]. In contrast, characterisation of dissection properties in *untreated* tissue has been well investigated. Dissection propagation was first investigated by infusing liquid into the media to mimic the process of blood flow initiating and propagating a dissection [125, 49, 47]. Later, Sommer et al. performed controlled peeling of the aortic media and recorded the force displacement behaviour [46]. This method has been used with tissue from complex sites like bifurcations [48], and with diseased human thoracic aortic and abdominal aortic aneurysms [57, 58].

Controlled peeling in this way clearly represents a simplification of in vivo loading regimes, and it could be argued that liquid infusion experiments more closely resemble blood flow-driven dissection, at least. In the latter configuration, while the separation of vessel layers would remain predominantly mode 1 (figure 3.1), there is likely an ambiguous mixture of rupture modes involved in any particular experiment. It is correspondingly difficult to extract meaningful and repeatable measures of tissue strength by this means. Peeling, by contrast, involves pure mode 1 rupture, and the physical meaning of the derived energy release rate G_c is correspondingly clear. The rupture process, being driven by displacements of opposing tissue flaps, is also easier to control, further improving repeatability. Therefore, as a means of quantifying resistance to dissection (i.e. separation of tissue layers), and of reliably assessing the effect on this of the different treatments, peeling tests were adopted in this work.

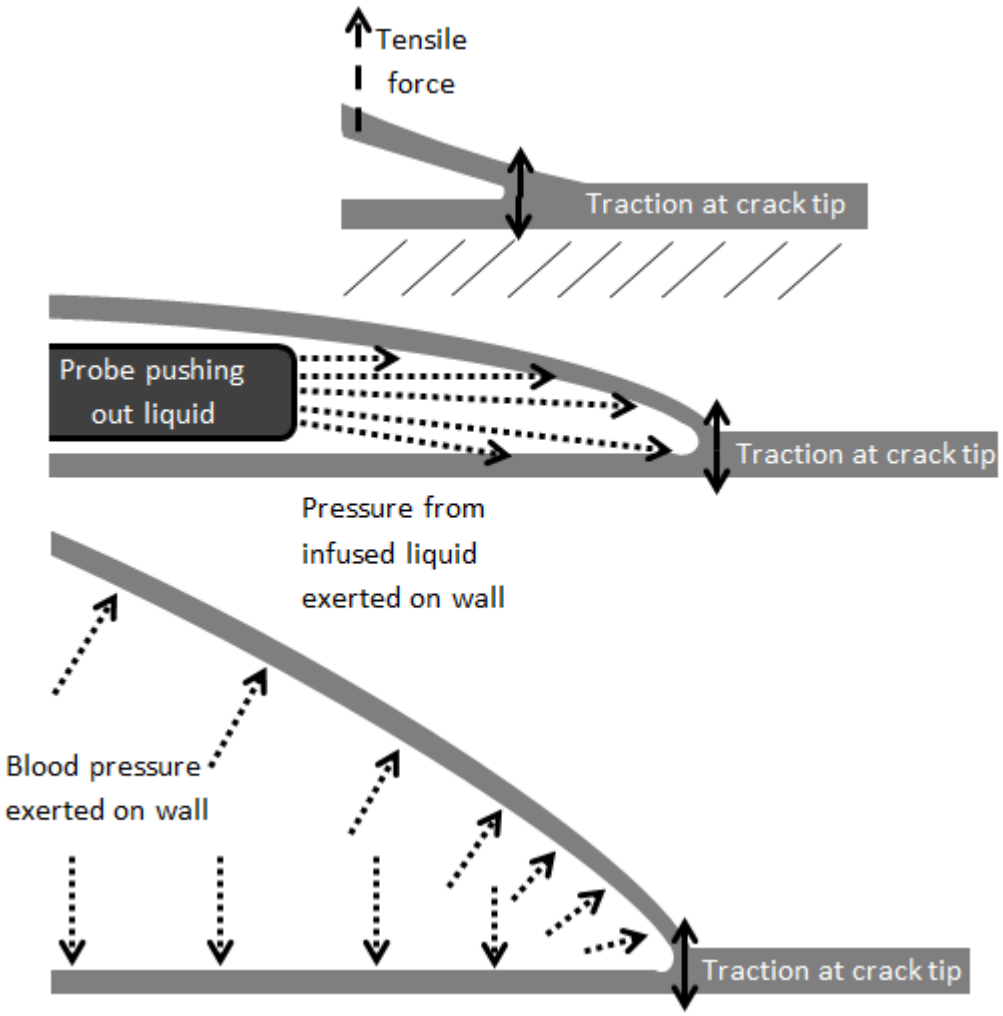

Figure 3.1: 2D schematic illustrating the similar tractions at the crack tip for peeling, liquid infusion and blood pressure propagation of the dissection.

3.2 Methods

3.2.1 Sample Preparation

Thoracic aorta from healthy pigs bred for human consumption were collected from a local butcher on the same day as slaughter and transported in a cooled environment to the laboratory. Excess connective tissue was removed and the aortas were cleaned and stored in saline solution. Each aorta was cut into 40 mm by 10 mm strips, oriented either in axial or circumferential (circ) directions (figure 3.2). Sample geometry was based on tests performed by [46]. The effect of sample geometry and edge effects have not been previously investigated and were not investigated in this study. However, [126] proposes that the resistance to peeling results from radially running collagen fibres that have a uniform density and in this work the same assumptions are made. The adventitia was carefully peeled away and discarded to ensure similar mechanical properties on either side of the tear when peeled. The intima was deemed to be too thin to have a significant influence on the mechanical

response, and was therefore not removed. Finally a tear was initiated by making a small incision through the centre of the media. As in chapter 2 samples were taken from the upper thoracic aorta proximal to the heart to have sufficient thickness. However, arteries further from the heart have different peeling properties to those closer, see table 3.4. This variation between samples is likely present even with samples from relatively similar locations along the arterial tree and may explain variation between samples seen later.

Collagenase, elastase and glutaraldehyde treatments were performed according to the protocols described previously in chapter 2, and as further summarised in table 3.1. Control and treated tissue was tested within 48 hours of the slaughter of the animal, (this period included both retrieval of tissue from the supplier and incubation according to the described protocols). After treatment all samples were washed thoroughly in saline solution and stored in saline solution plus antibiotic and anti-fungals at room temperature prior to testing.

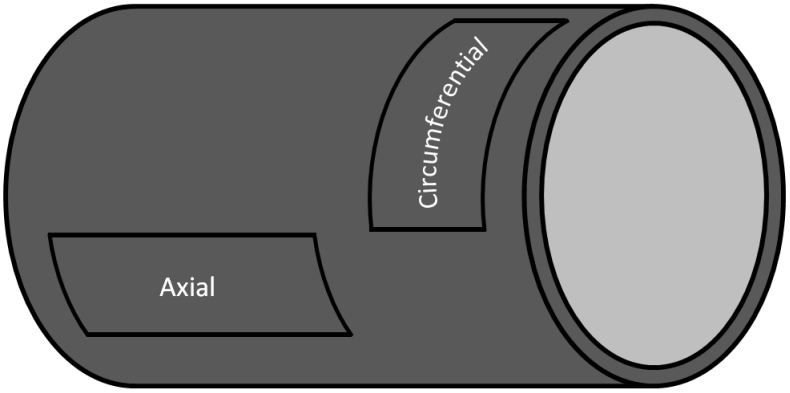

Figure 3.2: Schematic showing orientations of sample with respect to the artery wall.

Table 3.1: Enzyme, glutaraldehyde and control treatment concentrations and durations. N(axial) and N(circ) are the number of treated samples in the axial and circumferential direction respectively.

Treatment	Concentration	Temp.	Duration	N(axial)	N(circ)
Control	-	37°C	20 hours	16	16
Collagenase (Roche)	0.05 U/ml	37°C	20 hours	14	17
Elastase (Sigma Aldrich)	0.2 U/ml	37°C	20 hours	14	16
Glutaraldehyde	0.1%	4°C	20 hours	14	13

3.2.2 Test Protocol

Samples were prepared for peel testing by carefully pulling apart the flaps either side of the incision to leave 10 mm of tissue tongues for the tensile machine grips to hold. To measure sample geometry, samples were photographed using a Fujifilm Finepix Z90 digital camera with a ruler adjacent for scale (figure 3.3). Sample

width and peeled length were then estimated using ImageJ software[1]. Mean sample geometries are summarised in tables 3.2a and 3.2b. The tissue width is used to normalise the dissection force as wider samples would be expected to have a greater peeling force. This is because more tissue is peeled with a wider sample, for a given length, and thus more energy expended. The length is used to find G_c from 3.1. The standard deviations are small so while sample geometry is assumed to not affect the recorded G_c, if any variation does occur as a result of sample geometry it will be minimal. The thickness was not recorded as it has been previously shown that there was no correlation between tissue thickness and dissection force [46]. After photographing, samples were placed back in PBS solution for 5 seconds to rehydrate before mounting in the tensile test machine grips. Peel testing was performed at room temperature on a Tinius Olsen 5 kN tensile machine with a 10 N Tinius Olsen load cell. The samples were mounted such that the machine grips were as close to the start of the tear as possible. Grip surfaces were serrated to prevent slippage. Gradual loading was applied until 0.05 N force was registered, to place the sample in tension just prior to testing. The machine head was then displaced at 1 mm/s to peel the sample apart. A study by van Baardvijk and Roach [127] suggests dissection speeds may vary significantly under pulsatile blood pressure loads. The peeling speed used here, which lies near the middle of the range identified in [127], was thus selected to approximate the physiological loading rates experienced by the tissue during an intervention, whilst ensuring controlled peeling was maintained. Peeling was performed to complete separation as this guaranteed that the length of tissue peeled was similar between samples. If peeling was stopped after a certain amount of grip displacement the amount of tissue peeled would vary greatly (shown in figure 3.5). While this is not a physically accurate representation, the data in figure 3.5 shows no evidence that there are any edge effects or other phenomena at the end of the peel test. Additionally, the time during which samples were out of saline solution was minimised, to ensure they remained hydrated. If the sample broke before the two sides had completely peeled, it was discarded. Additionally, the thickness each side of the tear was not recorded but was monitored to ensure that the tear remained close to the centre of the tissue. If tissue thickness on one side of the tissue was substantially thicker than the other then the sample was also discarded. The experimental configuration is illustrated in figure 3.4.

3.2.3 Critical energy release rate

As in [46], the critical energy release rate (G_c) is utilised to quantify the peeling response. This is found in either the axial or circumferential direction as follows:

$$G_c = (W_{ext} - W_{elastic})/L \tag{3.1}$$

[1] **http://imagej.nih.gov/ij/**

Table 3.2: Mean ± standard deviation of sample dimensions.

(a) Width of tissue (mm).

	Control	Collagenase	Elatase	Glutaraldehyde
Axial	9.4 ± 1.2	9.3 ± 0.8	9.3 ± 0.7	9.9 ± 1.1
Circumferential	9.4 ± 1.2	9.7 ± 0.6	9.7 ± 0.7	10.1 ± 0.9

(b) Length of tissue to be dissected (mm).

	Control	Collagenase	Elatase	Glutaraldehyde
Axial	31.4 ± 1.4	30.1 ± 2.1	30.9 ± 1.5	30.2 ± 1.9
Circumferential	31.5 ± 2.3	29.3 ± 2.2	30.5 ± 1.4	31.9 ± 3.1

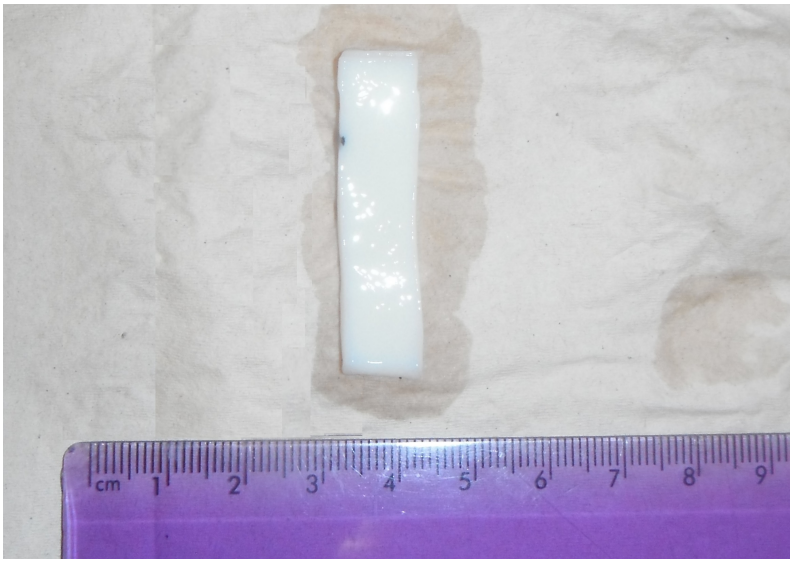

Figure 3.3: Sample before peeling. The initial tear began at the top of the specimen and extended to the black marker.

where W_{ext} and $W_{elastic}$ are the externally applied work and stored energy per unit width, and L is the length of tissue to be dissected, shown in figure 3.4. W_{ext} is computed using:

$$W_{ext} = 2Fl \tag{3.2}$$

where F is the mean peeling force (per unit width), and l is the length of the tissue in the stretched state, immediately prior to breaking. Both are illustrated in figure 3.5 (see figure 3.4 for additional explanation of l). Equation 3.2 can be understood as the tensile machine grip displacement ($2l$) multiplied by the mean peeling force. Equivalently, this can be approximated by twice the area under the steady state region of the curve in figure 3.5. Finally $W_{elastic}$ is estimated as the mean force per width times the tissue change in length, i.e:

$$W_{elastic} = F(l - L) \tag{3.3}$$

wherein linearity of the constitutive response is assumed - see discussion in [46].

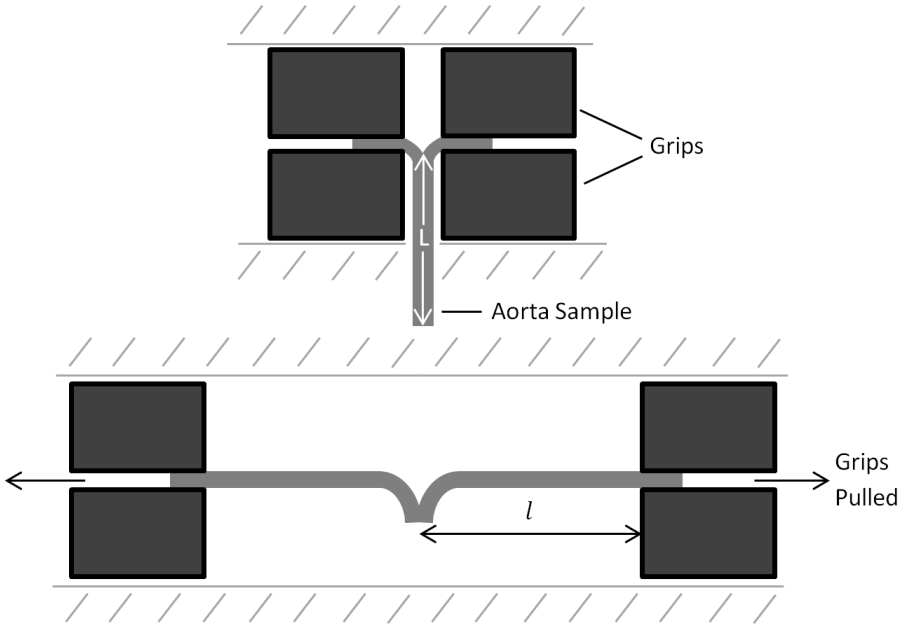

Figure 3.4: Schematic of experimental set up before loading and immediately before full separation. The top image shows the free tongues, made by the initial manual tearing, held by grips. L is the length of tissue to be dissected. In the bottom image, l is the length of the tissue at full separation.

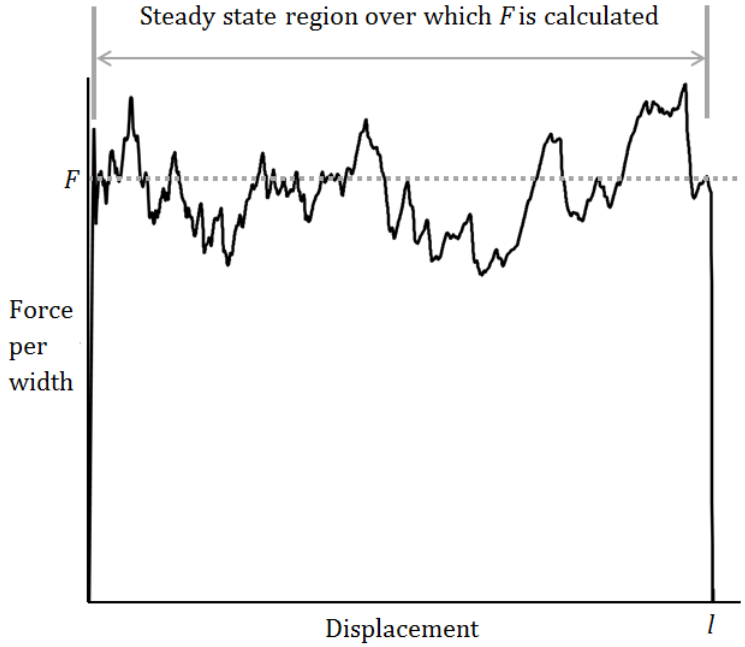

Figure 3.5: Representation of the force displacement data from a peel test, and indicating the region over which the mean peeling force F is calculated. The displacement l of the loading grips at full separation is also shown.

3.2.4 Multiphoton microscopy

To visualise the effect of enzymatic digestion on collagen and elastin fibres, two photon and second harmonic generation microscopy (TPM and SHG) was performed on a series of samples created using the same protocols as for the test specimens. It

was conducted on a Zeiss Upright LSM510 Meta Confocal Microscope with a class 4 tuneable Ti-Sapphire two-photon laser. TPM was conducted at 800 nm to visualise elastin fibres and SHG at 950 nm for collagen. Samples were imaged from the intimal side on the axial-circumferential plane at a depth of 19.5 μm from the surface.

3.3 Results

3.3.1 Controlled peel testing

Hereafter, superscipts "a" and "c" are used to denote results for axial and circumferential samples, respectively. A common pattern of behaviour can be seen across all samples with a sharp increase to a well defined, but uneven, plateau region, followed by a sudden drop off, as the sample fully separates. This can be seen in figure 3.6.

The mean force values from the plateau regions of each curve were computed and then averaged to find F^a and F^c. These are shown in table 3.3. Critical energy release rates, G_c^a and G_c^c, are shown in table 3.3. Further observations of behaviour for each treatment type are presented:

Table 3.3: Average steady state forces per unit width and critical energy release rates ± standard deviations, with associated p values compared with control results. Units for F and G_c are N/m and J/m^2, respectively. p values were calculated from G_c data using Student's unpaired t-test [4].

(a) Axial.

Value	Control	Collagenase	Elastase	Glutaraldehyde
F^a	76.7 ± 25.9	53.9 ± 12.2	69.1 ± 27.0	83.6 ± 13.7
G_c^a	183.3 ± 64.2	135.8 ± 31.2	171.8 ± 71.2	186.3 ± 33.5
p value	N/A	<0.05	n.s.	n.s.

(b) Circumferential.

Value	Control	Collagenase	Elastase	Glutaraldehyde
F^c	67.4 ± 11.7	49.3 ± 11.9	58.8 ± 17.3	91.2 ± 28.2
G_c^c	151.8 ± 27.0	108.1 ± 28.0	132.4 ± 40.0	190.1 ± 60.5
p value	N/A	<0.05	n.s.	<0.05

Control. No significant difference ($p \not< 0.05$) was found between G_c^a and G_c^c for the control samples (table 3.3). The force plateau regions for most samples (though for axial samples in particular) were quite noisy, and the spread of values between samples was relatively high. Standard deviations for F^a and F^c were therefore similarly high (with the standard deviation of F^a largest). Correspondingly, though G_c^a was larger than G_c^c, the difference was not significant.

Collagenase. G_c^a was significantly greater ($p<0.05$) than G_c^c. Comparing to the control samples, G_c^a and G_c^c were both significantly lower (table 3.3). There was little

difference in curve profiles or spread between circumferential and axial directions, as reflected in the standard deviations of F^a and F^c.

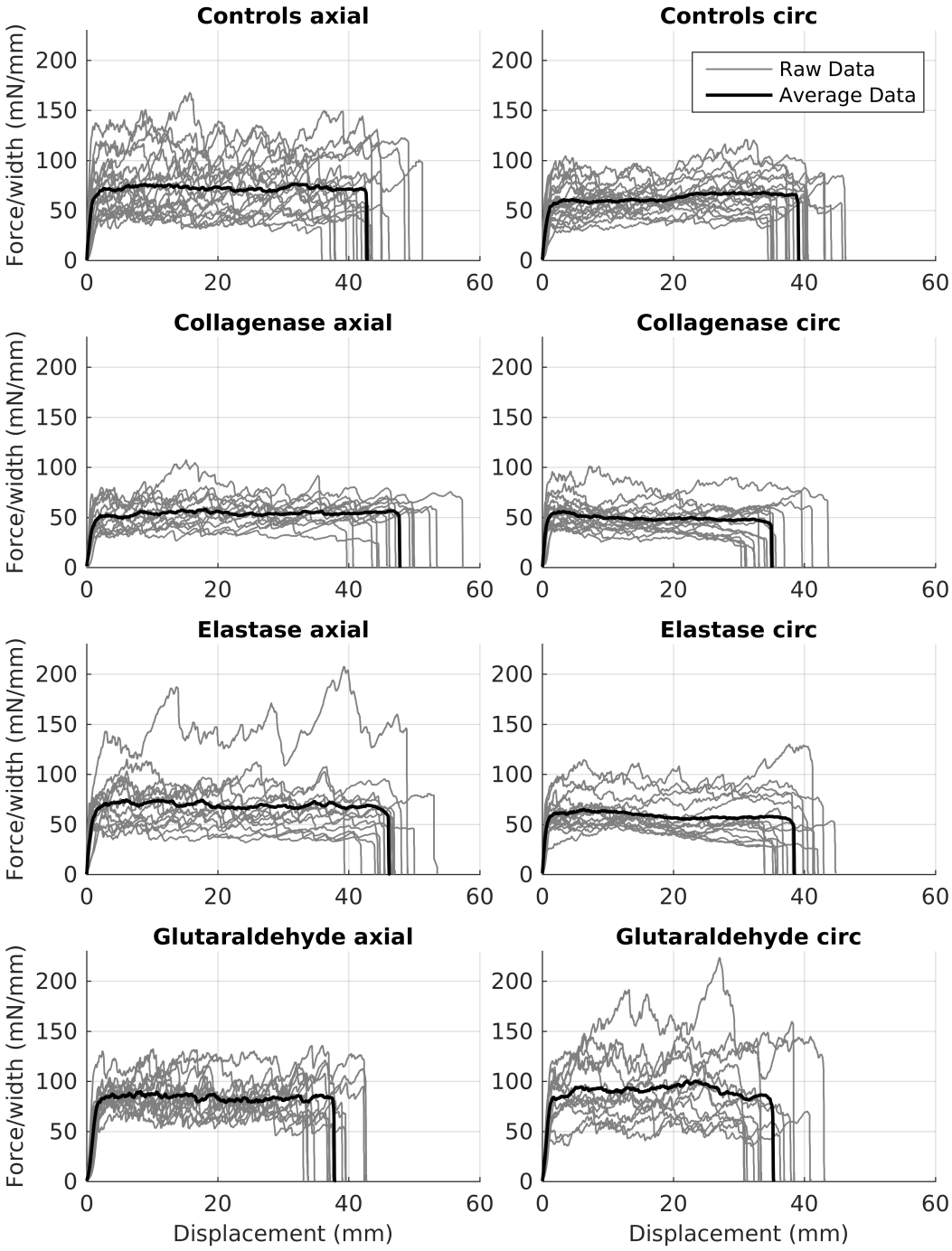

Figure 3.6: Force per unit width versus displacement for peel tests in the axial and circumferential directions.

Elastase. No significant difference was observed between G_c^a and G_c^c ($p \not< 0.05$) and both were similar to the control samples (table 3.3). The pattern of higher noise in axial results is also observed here, again also seen in the standard deviation of F^a being far greater than that of F^c.

Glutaraldehyde. G_c^a and G_c^c were also similar, with G_c^c slightly, but not significantly, higher ($p \not< 0.05$). Comparing with control samples, there was a significant increase

in G_c^c, but no significant difference in G_c^a (table 3.3). Unlike the control and elastase treated samples, the noisiness of the plateau region and spread of data were greater in the circumferential direction. This can also be seen in table 3.3, where the standard deviation of F^c is greater than that of F^a.

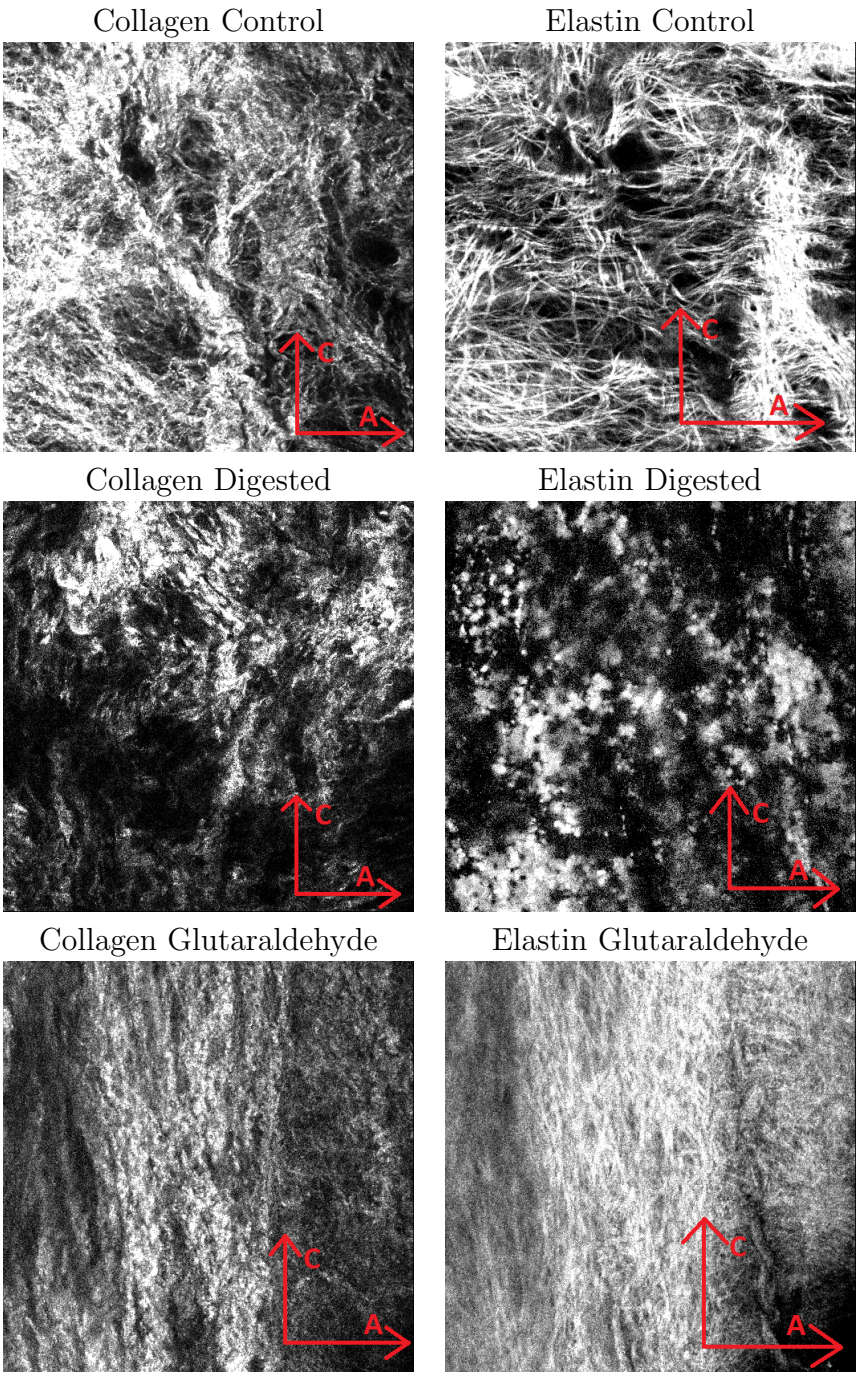

Figure 3.7: SHG images of collagen and TPM images of elastin (at depth of 19.5μm) for controls, samples with either proteins digested by their respective enzyme and each protein following glutaraldehyde treatment. Intimal side of the axial-circumferential plane is presented to demonstrate the protein loss. C and A on the images axis refer to circumferential and axial directions respectively.

3.3.2 Microscopy

Multiphoton images of the elastin and collagen in control samples and the samples after partial digestion of the respective proteins are shown in figure 3.7. It can be seen that there is a clear loss of each respective fibre after digestion with both collagenase and elastase. The remaining collagen fibres appear more wavy and less distinct, with more empty space visible and thinner fibres missing, while there appears to be little remaining structure to the elastin fibres. Finally, it appears glutaraldehyde treatment caused an increase in fibre crosslinks and fibre density for both collagen and elastin.

3.4 Discussion

The noisy force profiles yielded by all samples are similar to those described elsewhere for peel testing and other forms of arterial tearing [46, 48]. They most likely stem from the fibrous structure of the arterial wall. Separation of the neighbouring layers, correspondingly, is characterised by progressive breaking of individual fibres, or of larger fibre bundles, so that the overall failure process more closely resembles a series of discrete failure events, rather than a single continuous one. Similar effects have been observed in rubber as so-called stick-slip tearing.

Previous work has highlighted anisotropy in the peeling behaviour of arterial walls [46]. The axial direction was shown to exhibit more erratic behaviour, with the plateau region being less flat and with greater variation between samples compared to the circumferential direction. This was also seen for F^a and G_c^a in this study: both were higher and had greater standard deviations than did their circumferential counterparts. This is again thought to be related to the fibrous structure of the tissue.

Of the previous studies identified (table 3.4), the values for G_c^c in control samples of this study (151.8 ± 27 J/m^2) were closest to those of Carson and Roach [47], who reported a G_c of 159 ± 9 J/m^2 (though the orientation of their specimens was not reported). In their study, porcine thoracic aorta was used (as here) however, the tearing was propagated via liquid infusion, rather than peeling. The patterns of deformation, and corresponding modes of failure were therefore different from those in the experiments conducted here (see Section 3.1), and care must be taken in drawing comparisons. Results of other liquid infusion studies, for example, corresponded less well with the values presented here, with the possible exception of lower abdominal aorta results from [49]. The force and energy measurements in this work were generally much higher than those of previous peel test studies, with the exception of Pasta et al. [58], whose F^a and F^c values were significantly higher again. Furthermore, this range of values is not unexpected considering the variability in response of arterial walls subjected to tensile loading in the axial and circumferential directions: average

constitutive parameters (fitted to biaxial tensile test data) of control samples from two similar studies were over an order of magnitude different [42, 128]. Nevertheless the values for F_a, F_c, G_c^a and G_c^c reported here are greater than nearly all values found in other studies. One reason for this discrepancy may be the test conditions. Tests here were performed at room temperature and in open air, both of which will likely increase the dissection energy. Furthermore to prevent tissue drying and to more closely reflect *in vivo* conditions, testing was performed at 1 mm/s. However, Tong et al. showed that faster testing speeds increased the dissection energy and is further explanation for increased G_c in this study.

Table 3.4: Healthy artery peeling forces per width, F_a, F_c (N/m), and critical energy release rates, G_c^a, G_c^c (J/m^2). P, porcine and H, human. A, aorta; TA, thoracic aorta; ATA, UTA and LTA, ascending, upper and lower thoracic aorta; AA, abdominal aorta; UAA and LAA, upper and lower abdominal aorta; ICA and CCA, internal and common carotid artery; CA, coronary artery. LI, liquid infusion.

Vessel	Method	F_a	F_c	G_c^a	G_c^c	Ref.
P-UTA	LI		-	159 ± 9		[47]
H-A	LI		-	16.5		[56]
P-ATA	LI		-	43.9 ± 21.9		[49]
P-UTA	LI		-	28.4 ± 11.9		[49]
P-LTA	LI		-	29 ± 12.1		[49]
P-UAA	LI		-	18.8 ± 8.9		[49]
P-LAA	LI		-	113.4 ±40.5		[49]
H-AA	Peeling	34.8 ± 15.5	22.9 ± 2.9	76 ± 27	51 ± 6	[46]
H-ICA	Peeling	26.9 ± 7.1	-	60 ± 16	-	[48]
H-CCA	Peeling	33.7 ± 10.9	21.5 ± 4.2	75 ± 24	48 ± 10	[48]
H-ATA	Peeling	149.0 ± 7.6	126.0 ± 6.6	-		[58]
H-CA	Peeling		-	10.3 ± 5	-	[129]
P-TA	Peeling	76.7 ± 25.9	67.4 ± 11.7	183.3 ± 64.2	151.8 ± 27.0	Present

3.4.1 Collagenase

The significant drop in G_c^a and G_c^c compared to control samples implies that collagen has a large effect on peeling response. The microscopy results also show a clear loss of collagen fibres and resulting structure. This supports the literature on Ehlers-Danlos syndrome presented in the introduction, in which collagen loss was noted to correlate with higher rates of dissection. Additionally previous studies reported that collagen lies between lamellae and that toward the centre of this interlamellar space the fibres are randomly orientated [130].

The difference between G_c^a and G_c^c increased in the collagenase treated samples, which is contradictory to results from tensile tests wherein anisotropy decreased with decreasing collagen content [40]. However, the overall spread of G_c^a and G_c^c (as measured by the standard deviation) became more similar, implying that treatment reduced the variability between samples. The mechanisms by which collagenase

reduces inter-sample variation are not clear, but differences in collagen density and cross-linking likely contribute to the variation between animals and location. Digestion of collagen may correspondingly reduce this variation.

The steady state regions of the force responses are smoother for collagenase samples than for controls (in both directions), which may reflect both reduced concentration of collagen fibres and lower strength of remaining fibres. These findings are similar to those in chapter 2, where only collagenase treated samples showed a statistically significant drop in fracture stress compared to controls.

3.4.2 Elastase

Overall, there was little difference between the control and elastase treated samples, with no statistically significant differences in either G_c^a or G_c^c. However, the microscopy images show large loss of elastin and nearly all fibre structure. This suggests elastin plays a lesser role than collagen in the tissues' resistance to controlled peeling.

On the other hand, while affirming a primary organisation into tangentially oriented sheets, [25, 130, 131] noted elastin struts between lamellae and interlamellar elastin fibers that may provide some radial resistance. Moreover, MacLean et al. [27] observed breakages in these small elastin fibres following radial loading of aorta samples, suggesting they would indeed bear some of the load applied in this study. Viewed in this light, then, the present results may rather reflect either very low strength in these small fibres so that the effect of their degradation was not detectable in the experiments conducted here, or inadequate permeation of the enzyme to the centre of the samples, where these fibres reside. Whatever the true mechanism, it is clear that the elastase treatment, in contrast to its influence on tensile behaviour, had little effect on the peeling behaviour of the aorta samples.

3.4.3 Glutaraldehyde

Glutaraldehyde has been previously utilised for cross-linking collagen to increase material stiffness and tensile strength [132, 133]. In this work, glutaraldehyde was the only treatment to show increases in G_c^a and G_c^c compared to controls, though only the circumferential increases were significant ($p < 0.05$). In contrast, the tensile testing in chapter 2 found little effect of glutaraldehyde treatment on the tensile elastic and fracture properties of porcine aorta. However, microscopy images in the axial-circumferential plane showed increased crosslinking and fibre density. Therefore, this implies that partial cross-linking resulting from low concentration glutaraldehyde treatment is more effective on radial bridges between lamellae, that resist peeling forces, than in fibres in the axial or circumferential directions, that resist the uniaxial extensions seen in chapter 2.

3.4.4 Diseased tissue comparison

Few studies have investigated the effect of disease on tissue response under controlled peeling. Difficulties in finding a significant number of participants for relatively rare genetic diseases like Marfan's and Ehlers-Danlos syndrome prevent investigation into the biomechanical effects of these diseases.

However, peel tests have been performed on aneurysm tissue from ascending thoracic aorta and compared to healthy tissue from the same location [58]. They found that both F^a and F^c for aneurysm tissue were significantly lower than for healthy tissue and that the difference between F^a and F^c was decreased in aneurysm tissue, indicating a loss of anisotropy. This behaviour is most like that of the collagenase digested tissue reported here. However, aneurysms are more strongly associated with elastin loss, which were found here to have negligible effect on controlled peel testing of arterial samples.

3.4.5 Limitations

In this study it was assumed that the effect of smooth muscle cell bridges, between the lamellae, on the tissue response to controlled peeling was small, compared with those of collagen and elastin. Nevertheless it has been shown that smooth muscle cells do play a role in arterial dissection *in vivo* [134, 135]. A dedicated investigation into the effect of removing smooth muscle cell contribution (for example by means described in [136]) in controlled peeling conditions would help to clarify their role.

Previous studies performed peel tests within a saline bath, whilst in this study testing was conducted at room temperature and in open air. Peel tests took around 90 s, and specimens were exposed to air for around 4 minutes on average. Utilising a saline bath at 37°C may yield results with more physiological relevance, however since all tests were performed under the same conditions the comparisons made here are still valid.

The loading rate applied to the samples is greater than that applied in previous studies. Tong et al. investigated the effect of peeling rate on the tissue response [57]. They found approximately 30% difference in F between samples tested at 1 mm/min and 1 mm/s, a significantly smaller difference than between the findings here and results from other studies presented in table 3.4. This suggests speed alone does not account for the discrepancy, and variation between samples, as described in the opening of the Discussion, may play a greater role.

Mechanical tests (of any kind) do not allow changes in the arterial wall microstructure to be observed directly, even if some overall changes may be inferred from their results. Example images acquired with multiphoton microscopy, and in the axial-circumferential plane, were presented here, to enable qualitative assessment of structural changes. But, more detailed and systematic visual analysis using these

modalities [137], or perhaps histology [48] or electron microscopy [131] would enable microstructural changes to be assessed conclusively, and may present a link between elastin/collagen radial fibre bridging and gross mechanical properties.

To ensure complete removal of the adventitia an incision was made midway through the arterial through-thickness. This involved removing more tissue than was likely necessary and removal of the adventitia could not be certain. This may have effected the variation in mechanical properties between samples as more adventitia may be remaining on some samples than others where it was completely removed. Imaging techniques such as histology would aid in verifying whether this technique did indeed fully remove the adventitia and should be utilised in future studies [94].

Finally, in this work the samples were tested as flat rectangular pieces, while *in vivo*, the vessel is tubular and held in a pre-stressed state that is partially released by cutting the vessel open to lay it flat. The effect of this difference on the dissection propagation and on measured values such as the F and G_c are unknown, as previous work, either peel testing or liquid infusion testing, also involved flat samples. An investigation into the dissection behaviour of the artery wall in its *in vivo* configuration would help to clarify the effect of flattening the tissue in this way.

3.5 Conclusions

Applying collagenase solution to porcine thoracic aorta made the tissue less resistant to peeling in both axial and circumferential directions. However, anisotropy in the critical energy release rate was increased compared to control samples. Elastase treatment had a negligible effect on the tissue response to controlled peel testing. From these it may be inferred that collagen plays a more important role in resisting this loading mechanism. Glutaraldehyde treatment increased resistance to peeling in both directions, but more so in the circumferential direction. Anisotropy in the response was correspondingly reduced. Thus, cross-linking accompanying this treatment appears to impart greater strength in the circumferential direction.

Of the treatments considered, the effects of collagenase most closely resembled those of aneurysm formation. This is despite elastin loss being more commonly associated with this condition. Regardless of the possible difference in underlying mechanisms, collagenase treatment appears to be a viable means of altering the peeling response of aortic tissues to emulate the effects of this disease. Combined with those of chapter 2, these findings suggest that all of the described treatments are useful in creating physical models of diseased tissue.

Finally, the direct effects of genetic diseases, such as Ehlers-Danlos and Marfan's syndrome, on arterial wall constituent proteins are relatively simple to understand and emulate. However in an individual with such diseases, compensatory processes in the body will alter the mechanical response of the wall beyond the effect of simple

enzyme digestion, thus requiring insight into the change in arterial wall structure by these processes. Additionally, for more complex diseases such as aneurysms, simple enzymatic digestion provides only an approximation of the various chemical, physical and cellular processes taking place within the arterial wall. However, the treatments described here appear to approximate the changes in dissection properties reported to accompany Ehlers-Danlos and Marfan's syndrome and provide similarities in behaviour for more complex processes such as aneurysms. Furthermore, more accurate emulation of dissection properties may also be produced using a combination of any or all of these treatments.

Chapter 4

Towards a modelling framework for catheter-induced dissection: viability of cohesive zone finite element approaches

4.1 Introduction

Catheterisation is a common procedure in treatments for a variety of cardiovascular diseases. As it is a minimally invasive procedure, it puts less strain on the patient and is far less costly than other treatment methods (i.e. if viable, stenting a diseased coronary artery is preferable to a coronary artery bypass graft and opening of the chest). However complications do occur and can have severe consequences for the patient. One of the most poorly understood complications is catheter-induced dissection (CID), where a catheter initiates and propagates a tear between the blood vessel layers. Consequences of this complication depend on severity and location, however the mortality rate, as identified in chapter 1, is relatively high. A potential approach to modelling such dissection processes is investigated in this chapter as a step toward development of numerical tools for simulating the complex catheter-tissue interactions involved. Such tools may in turn be valuable in virtual design processes for new devices, aimed at mitigating catheter-induced trauma. It is then hoped the effects of enzyme treatment on dissection behaviour on CID could be evaluated by a similar means as chapter 3. CID alone is considered in this chapter as peel tests are a relatively simple scenario from which changes in dissection behaviour from enzyme digestion can be easily evaluated. Catheter tests have considerably more complexity and so assessing the effects of enzyme treatment is far more difficult when other factors associated with the contact induced failure are also involved. In addition, this is the first work to investigate catheter induced dissection and identify many of the mechanisms involved in this process.

Arterial dissection has been well investigated both by *ex vivo* testing in a laboratory, and simulations with the FE method. The first *ex vivo* arterial wall dissection was performed via liquid infusion into the artery media [47, 49, 56]. This was aimed at replicating blood flow-driven propagation of the dissection. Later, controlled peeling of the media was employed to gain further understanding of the force displacement behaviour, and in particular the latter's anisotropy [46, 48]. This methodology was then utilised on diseased arteries and aneurysms to assess disease-associated changes [57, 58].

CZ approaches have been used in various forms to model dissection of arterial layers during peel testing [59, 60], similar to those presented in chapter 3. However, dissection driven by an external body, i.e. a catheter, is fundamentally different from a peeling configuration, as detailed in figure 4.1. In the case of peeling, tissue at the crack front experiences almost pure tension perpendicular to the direction of crack propagation, and newly exposed fracture surfaces are free. Conversely, when dissection is driven by an external body, tissue at the crack front experiences a complex combination of tension, as it is forced around the penetrating object, and compression, from the direct loading of the object. Moreover, the newly formed surfaces, rather than being free, are subject to a complex interaction with the external

object.

Comparable configurations exist during, for example, needle insertion and cutting. Among other approaches, CZ models have been used by various authors to simulate the tissue rupture processes in such scenarios, also. Needle insertion of muscle tissue has been investigated with parameters extracted from separate experimental data [61], however no direct experimental validation was presented in turn. This was partially addressed by Forsell and Gasser when modelling cardiac tissue penetration and failure as a result of perforation by a pacemaker wire [62]. However, it was not clear how the governing critical energy release rate G_c was calculated from the experimental data, making it difficult to assess the fidelity of their FE model with respect to the latter. Oldfield et al. utilised an experimental-computational approach to estimate G_c during needle insertion into a gelatine soft tissue phantom [63]. This approach yielded good agreement between experimental and computational force-displacement profiles at four different insertion rates and was more comprehensive than the previous studies mentioned. However, gelatine is a homogeneous isotropic material that does not exhibit the stochastic breaking of fibres/fibrils seen in perforation and damage of most soft tissues [64], and so it is still unclear how well the CZ formalism carries over to real soft tissues in this context. Lastly, Hernández and Peña studied deep perforation of the vena cava during filter insertion [138]. They performed perforation experiments into ovine vena cava that was held in biaxial tension and then simulated this with FE and CZ elements. Then by trial and error curve fitting obtained the CZ parameters, and found good association between the experimental and numerical fracture behaviour. However, perforation was performed through the tissue rather than to split tissue layers as here and it would be expected that there would be differences between the fracture behaviour. Additionally, while vena cava has some similarity to arterial tissue the mechanical and fracture behaviour will differ. A final, and important aspect that was superficially assessed, at best, in the foregoing studies is the fidelity with which the complex catheter-tissue interactions, especially near the crack tip, can be captured with CZ finite element formulations. As mentioned, this phenomenon is one of the key features that differentiate dissection by means of a penetrating external body, from simpler peeling configurations.

Though no previous authors appear to have studied penetration of arterial tissue using cohesive rupture modelling approaches, much less CID specifically, the success in modelling other soft tissues with these approaches in the foregoing studies suggest this is a promising approach. Such models are therefore investigated for this purpose in the present chapter, with an emphasis on clarifying the points of ambiguity that were identified. Specifically, CZ formalism is employed to model the dissection process as a catheter is forced between adjacent arterial tissue layers. An experimental configuration is first described, and corresponding results are presented and discussed. CZ theory is then described and applied within a FE model of the

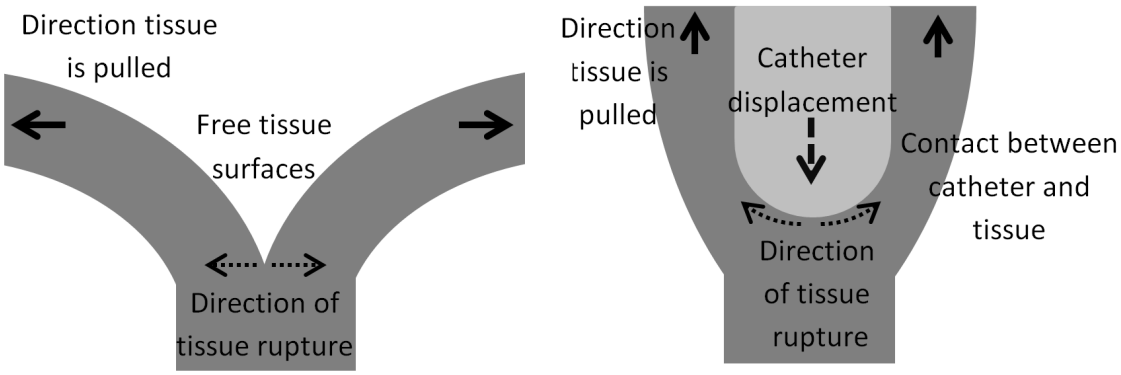

Figure 4.1: 2D schematic illustrating the differing mechanical environment at the tissue dissection front for peeling (left) and catheter driven dissection (right). Left: the direction the tissue is pulled is the same as the direction of tissue rupture due to the simple loading conditions. Right: the direction of tissue rupture is approximately perpendicular to the direction the tissue is pulled as the tissue deforms around the catheter. This will likely result in differing fracture behaviour, partly resulting from different fracture modes in each case.

experimental configuration. Poor association between experimental and numerical force-displacement data is found to be associated with the CZ response and thus an alternative formulation is presented. Finally, numerical issues related both to the above interaction phenomena and to the constitutive description of the tissue are reported and discussed.

4.2 Laboratory Testing

4.2.1 Methods

Experimental configuration

To understand the possible mechanism by which a catheter may propagate a dissection, a scenario was postulated in which the dissection has been initiated (the means by which were left for future investigations) and the catheter is positioned at the dissection front. The endovascular surgeon operating the catheter feels resistance to their attempts to guide the catheter to its destination as the catheter pushes against the dissection front. Assuming it is a bend in the vessel, they apply force to the catheter to propel it around this assumed bend. This inadvertently pushes the catheter into the created dissection front, driving the catheter between the layers of the media, and opening the dissection further. A corresponding experimental configuration was then devised to explore this scenario. A specimen of porcine aortic wall was partially dissected in a similar manner to specimens in the peel tests (chapter 3). After moistening, the newly created tissue tongues were fixed to two steel columns with super glue, as shown in figure 4.3. A catheter was positioned directly above the dissection front in the centre of the tissue. The catheter was then

displaced downwards into the specimen at 1 mm/s for 35 mm, while the reaction force (using a 20 N load cell) and displacement were recorded. This speed was chosen as a representative speed for a catheter in the above scenario as little information is present in the literature. This also allows values from chapter 3 to be used for CZ modelling as speeds are the same in both tests. The tissue was mounted such that the catheter would progress in the vessel's axial direction, corresponding to the scenario conception. The catheter was produced at Philips Research Eindhoven. The shaft was composed of PEBAX 5533 (blue in figure 4.3) and the tip of PEBAX 3533 (black in figure 4.3). The catheter geometry is shown in figure 4.2.

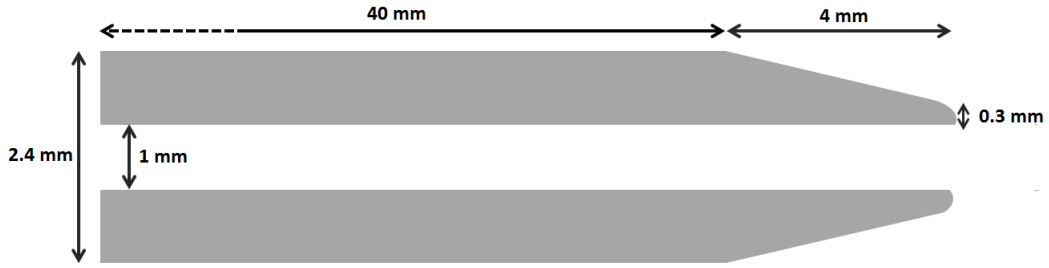

Figure 4.2: Schematic detailing catheter geometry (not to scale).

In case of errors or complications, the experiment was stopped, and data were discarded. Examples of such complications include the tissue detaching from the steel column or the catheter diverging from the axial direction. Results for six specimens were successfully recorded in this way.

Specimen preparation

Due to ethical and practical considerations, porcine thoracic aorta was chosen for the experimental model. As in chapters 2 and 3, samples were taken from the upper thoracic aorta proximal to the heart to have sufficient thickness. However, arteries further from the heart have different peeling properties to those closer, see table 3.4. This variation between samples is likely present even with samples from relatively similar locations along the arterial tree and may explain variation between samples seen later. This was transported from the supplier (Hemolab BV in Eindhoven, the Netherlands) in a cool environment to the laboratory. Excess connective and fatty tissue was removed, and the aortic wall was cut open along the axial direction and flattened out into a rectangular section. Each aorta was cut into several 40 mm long by 20 mm wide pieces, with the longest length aligned in the axial direction.The tissue was initially dissected by creating a small incision with a scalpel and then manually peeling apart, creating the two tongues to be fixed to the metal columns. Care was taken to ensure this initial dissection remained in the middle of the media, to coincide with the proposed scenario; if it progressed too far towards the adventitia or intima, the sample was discarded. The length of tissue to be dissected L was maintained at approximately 10 mm. This was chosen to provide sufficient tissue

to dissect, allowing the key stages of the process to develop (shown in figure 4.4). This also ensured catheter displacement, before full separation of the tissue halves, was not so large that the catheter reached the base of the apparatus. Additionally tissue width of 20 mm was chosen to ensure that edge effects were not present. Each sample was washed three times in saline solution and stored in saline solution in the refrigerator until tested. All samples were tested within 24 hours of the slaughter of the animal.

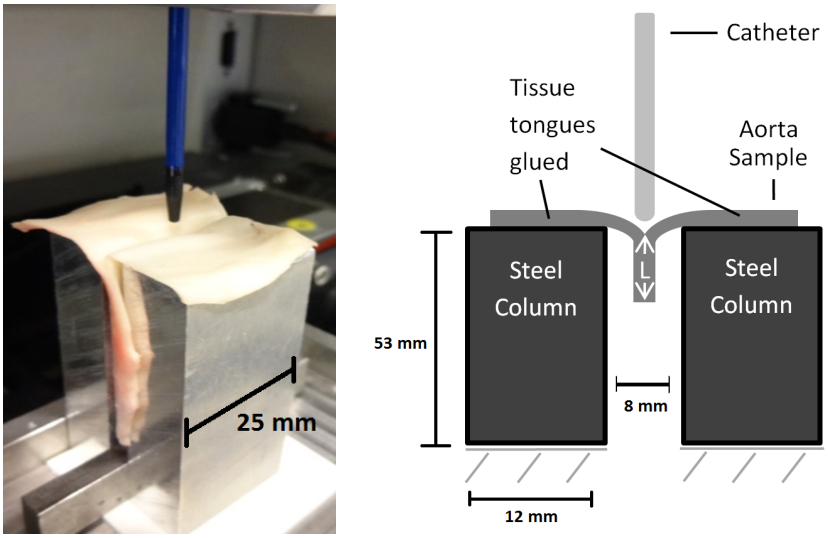

Figure 4.3: Experimental configuration for CID experiments. Left: image illustrating the catheter used, tissue fixation and steel column arrangement. Right: schematic of the experimental arrangement; tissue length $L = 10$ mm.

4.2.2 Results

The resulting force-displacement curves are shown in figure 4.4 along with their average. The shape and magnitudes of the curves are highly sporadic due to the stochastic dissection behaviour which has been noted previously in [46], and chapter 3. Despite the variation though, all curves follow approximately the same profile. The key phases in this profile are identified in figure 4.5.

From displacement 0 to U_D of the catheter, the tissue is deforming but no dissection is occurring, so that the classic increasing stiffness characteristic of fibrous tissues can be seen [139]. The measured reaction force F_R is considered to be the sum of contributions from friction F_{Fric} and the elastic resistance of the tissue F_{Def} (see figure 4.5). F_{Fric} will provide a significantly smaller contribution at this stage due to the small contact area between catheter and tissue.

The rupture and dissection initiates at U_D and finishes at U_R, when the catheter reaches the bottom of the tissue. Here the profiles of the raw data fluctuates due to individual fibre cross-links stretching and breaking. This was also seen in the plateau region of the controlled peel tests in chapter 3, however the magnitude of

the fluctuations is far larger in the present test. During rupture F_{Def} and F_{Fric} are assumed to again contribute to F_R. F_{Def} additionally acts to rupture the tissue ahead of the catheter tip.

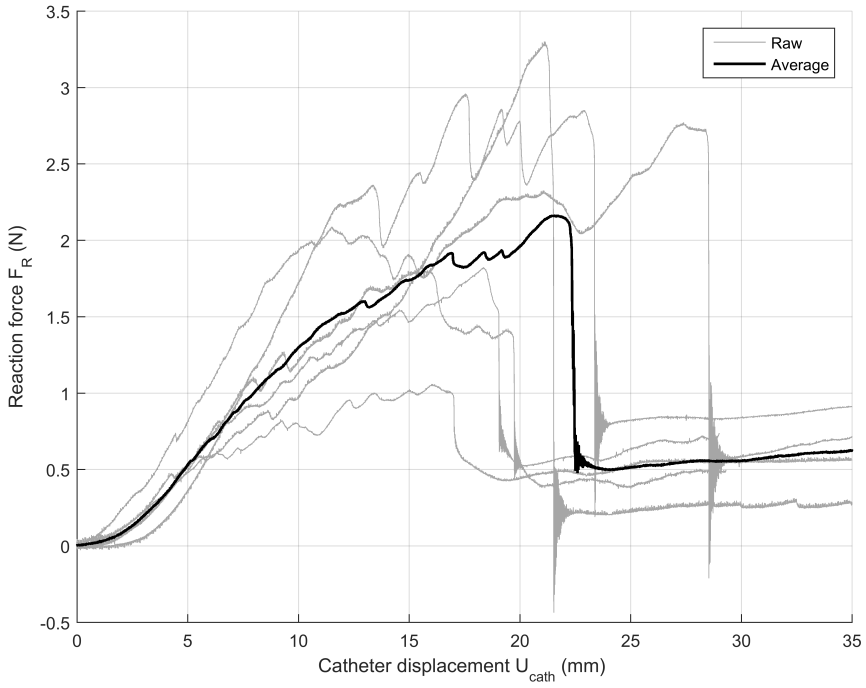

Figure 4.4: Reaction force on catheter versus displacement. Raw experimental curves (grey) are overlaid with the averaged curve (black)

Beyond U_R, the catheter has penetrated the full length of the specimen, and the shaft continues to move through the channel created during the dissection. The resulting friction-only region is relatively flat. It may be expected that F_R in this region is constant, however the average data show a small increase in F_R with increasing U_{cath}. This could be due to an increase in the coefficient of friction between the catheter and the tissue. This may reflect an increase in the friction coefficient, due to either or both of a gradual degradation of lubrication and changing interface conditions between catheter and tissue.

Figure 4.6 shows the arterial wall after perforation at three different points within the tissue. It can be seen that the damage is localised to the catheter dissection path throughout the experiment. This is likely because of the pointed shape of the catheter and the idealised conditions present here. It may be that *in vivo*, where the arterial wall is cylindrical, rather than flat, the path taken by the catheter and the resulting dissection are broader. Additionally, the hole created by the catheter could be made larger by the blood entering the hole and pushing the tissue halves further apart. Figure 4.6 also shows the fibre bridging between the fibre sheets during dissection, albeit in this case following manual peeling after the penetration experiment. During the catheter dissection tests these fibre bridges will stretch. The

corresponding accumulation of elastic energy and subsequent release as fibres break is the likely source of the fluctuating profiles seen in figure 4.4.

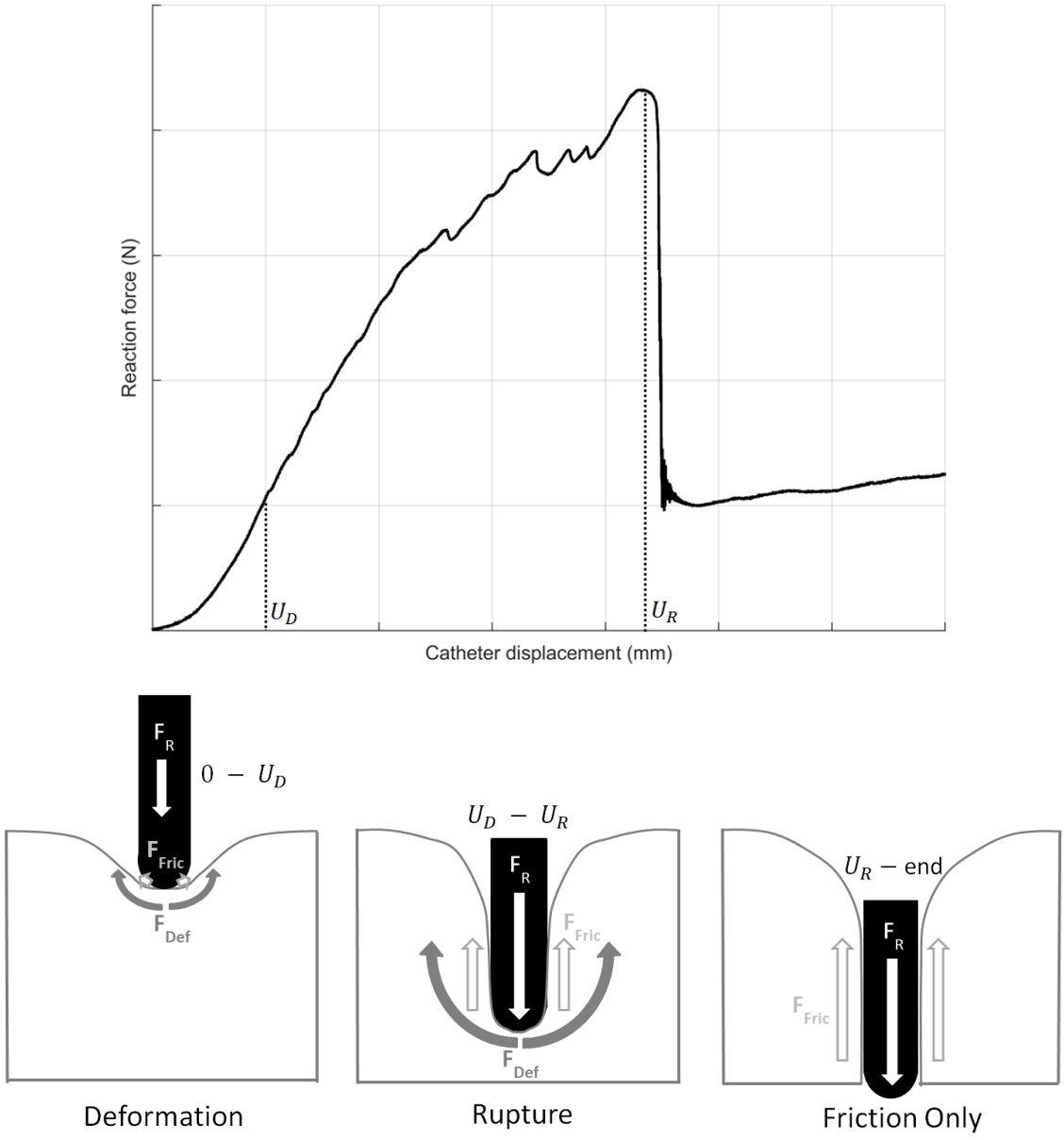

Figure 4.5: Top: The average reaction force-displacement profile from penetration experiments, annotated to indicate the three key stages of the penetration process. Stage 1 (0 to U_D): deformation of the tissue prior to penetration; stage 2 (U_D to U_R): progressive rupture and penetration of the tissue; and stage 3 (U_R and beyond): complete through penetration of the specimen, so that only frictional forces, between catheter shaft and tissue, are acting. The bottom row illustrates the relevant forces acting in each of these stages. While U_R can be clearly seen both physically and on the experimental curve its meaning is clear. However, U_D is difficult to observe and was identified purely from the experimental curve. Therefore U_D is purely illustrative to aid in demonstrating the transition from deformation to rupture.

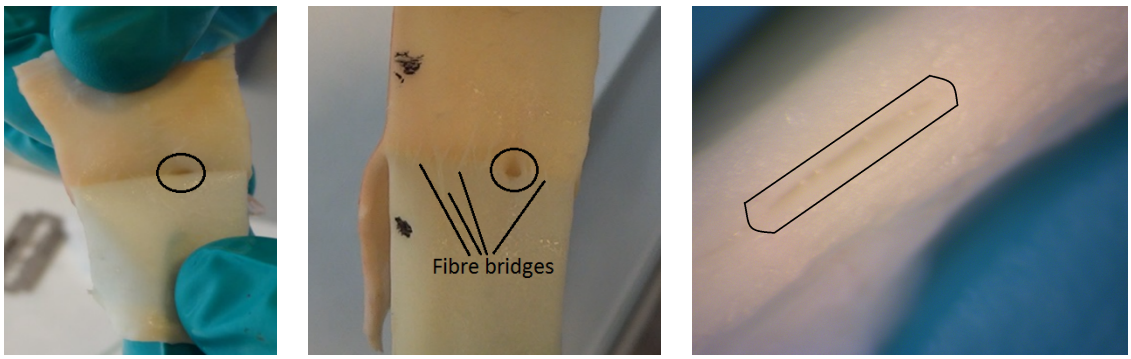

Figure 4.6: Arterial wall after perforation by the catheter, at various depths. Left: the dissection front of the initially peeled halves. The hole is indicated and is localised to the catheter path. Middle: a sample manually peeled after the experiment to show progression of the catheter-created hole. Damage by the catheter is still localised to its path through the tissue. Black marks on the left of the tissue indicate the point of initial manual dissection before the experiment. Fibre brides between the two tongues have been identified. Right: a low-power microscope image of the hole at the end of the tissue after the catheter has perforated through (after U_R in figure 4.5). The hole lies within the centre of the tissue and is again localised to the catheter path.

4.3 Numerical modelling using cohesive zones

Motivated by its excellent performance in simulating arterial peeling configurations [59, 60], and by the encouraging results of its application to other tissue puncture scenarios [62, 63], CZ formalism formed the basis of the models developed here for simulating the CID experimental configuration.

4.3.1 FE model

The CID process was simulated using the following finite element model created in MSC MARC 2014 and shown in figure 4.7. The model consists of 31075 8-node hybrid-formulation full-integration hexahedral elements and 21000 8-node CZ elements. A non-linear implicit solver was used to solve the model. Symmetry boundary conditions were applied to the nodes on the XY plane and XZ plane. XZ plane symmetry on the CZ elements was enforced according to figure 4.8 and setting G_c to half its true value, this was validated in prior experiments. A high density mesh was used in the contact region to improve model stability; this was joined to the low density mesh by tie restraints. The catheter was assumed to be rigid and a geometric contact body was used to model it. Half symmetry was employed for the catheter, rather than quarter symmetry in the rest of the model, to verify that the bottom nodes of the CZ elements displaced correctly in the Y direction. Mesh convergence analysis was conducted, for material properties that gave a converged solution solution (see section 4.4.2, below), to ensure a mesh independent solution. Both geometric and constitutive non-linearities were included.

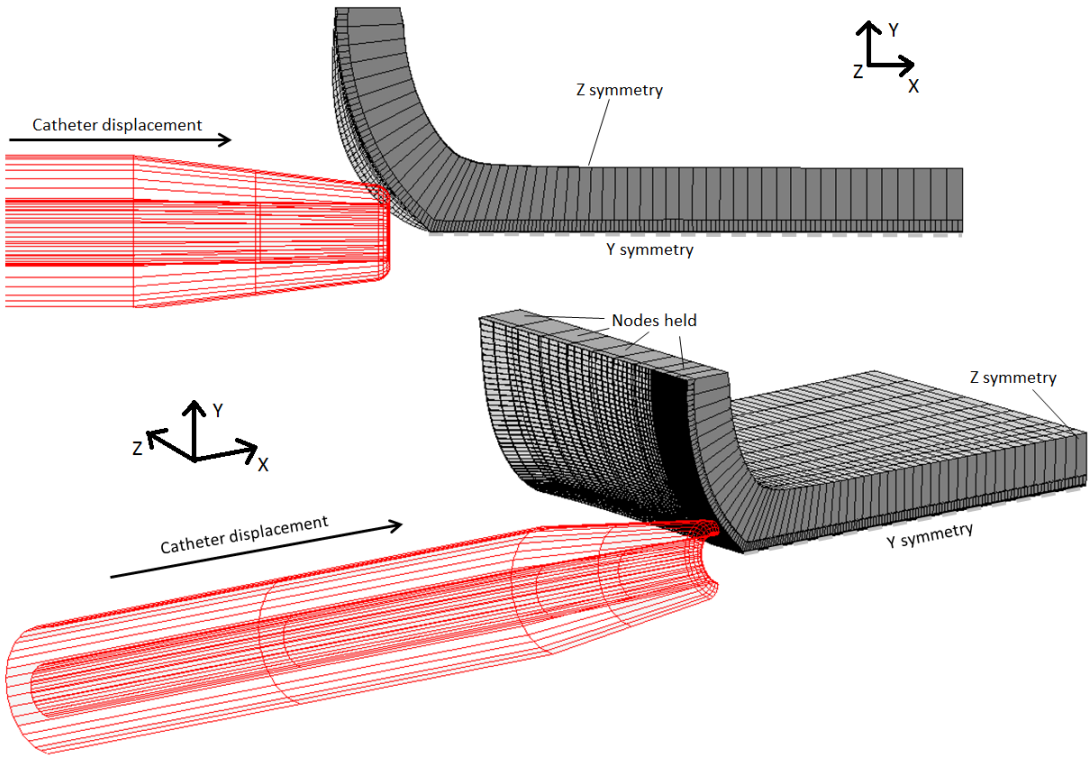

Figure 4.7: Model immediately prior to catheter insertion. The tissue is depicted in grey, and the catheter in red. Boundary conditions were applied as indicated. All other surfaces remained free. Exploiting symmetry, only 1/4 of the specimen was modelled explicitly. Symmetry planes perpendicular to Y and Z axes are correspondingly labelled.

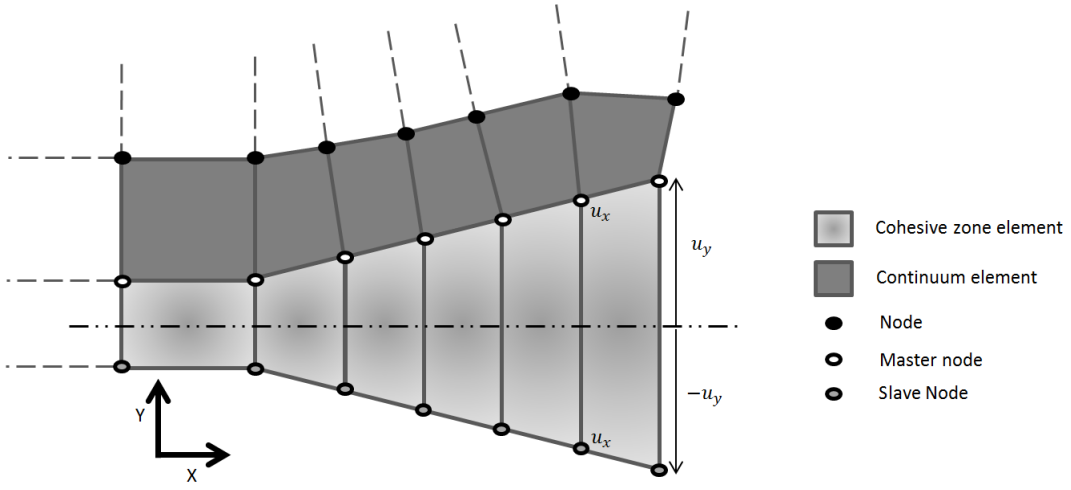

Figure 4.8: 2D illustration of nodal configuration in cohesive zone elements to ensure Y symmetry. Bottom nodes of cohesive zone are tied with the opposite top node such that the X and Z displacement are the same, and the Y displacement is the same but in the opposite direction.

4.3.2 Constitutive model

The GOH model from chapter 2 was again utilised here. However MARC 2014 deploys a modified compressible GOH formulation, which is based on a multiplicative

split of the deformation gradient, according to

$$\mathbf{F} = (J^{1/3}\mathbf{I})\bar{\mathbf{F}}, \tag{4.1}$$

where $(J^{1/3}\mathbf{I})$ is the volumetric (dilational) component and $\bar{\mathbf{F}}$ the isochoric (volume preserving) component. The right Cauchy-Green deformation tensor

$$\mathbf{C} = \mathbf{F}^T\mathbf{F} = J^{2/3}\bar{\mathbf{C}},\ \bar{\mathbf{C}} = \bar{\mathbf{F}}^T\bar{\mathbf{F}}, \tag{4.2}$$

can be similarly split. The GOH strain energy function following this split becomes

$$\Psi(\bar{\mathbf{C}}, \mathbf{H}_i, J) = \bar{\Psi}^m(\bar{\mathbf{C}}) + \sum_{i=1,2} \bar{\Psi}_i^f(\bar{\mathbf{C}}, \mathbf{H}_i(\mathbf{a}_i, \kappa)) + \Psi_{vol}(J), \tag{4.3}$$

where

$$\Psi_{vol}(J) = \frac{9}{2}K(J^{1/3} - 1)^2, \tag{4.4}$$

is the volumetric component, with bulk modulus K. Analogous to the incompressible version the isochoric component of 4.3 is broken down into an isotropic neo-Hookean contribution describing the elastin fibre response

$$\bar{\Psi}^m(\bar{\mathbf{C}}) = \frac{\mu}{2}(\bar{I}_1 - 3), \tag{4.5}$$

with $\bar{I}_1 = \mathrm{tr}\bar{\mathbf{C}}$ the isochoric first invariant and μ the shear modulus, and the anisotropic terms $\bar{\Psi}_i^f(\bar{\mathbf{C}}, \mathbf{H}_i(\mathbf{a}_i, \kappa))$ describing the two families of collagen fibres:

$$\bar{\Psi}_i^f(\bar{\mathbf{C}}, \mathbf{H}_i) = \frac{k_1}{2k_2}[\exp(k_2\bar{E}_i^2) - 1],\ i = 1, 2 \tag{4.6}$$

with

$$\bar{E}_i = \mathbf{H}_i : \bar{\mathbf{C}} - 1, \quad \mathbf{H}_i = \kappa\mathbf{I} + (1 - 3\kappa)(\mathbf{a}_i \otimes \mathbf{a}_i). \tag{4.7}$$

The collagen fibre directions in the reference configuration are defined by unit vectors $\mathbf{a}_1 = [\cos\theta, \sin\theta, 0]$ and $\mathbf{a}_2 = [-\cos\theta, \sin\theta, 0]$, where θ is the angle between the circumferential direction of the artery and the fibre direction (previously shown in figure 2.2). The degree of fibre dispersion is captured by a statistical parameter $\kappa \in [0, \frac{1}{3}]$, where $\kappa = 0$ denotes complete alignment of fibres, while $\kappa = \frac{1}{3}$ implies full dispersion, resulting in isotropy. Additionally, k_1, is a stress-like parameter, k_2, a dimensionless parameter and the second order tensor $\mathbf{H}_i(\mathbf{a}_i, \kappa)$ is a general structural tensor for fibre family i. Finally, $\bar{\mathbf{C}}$ is the isochoric right Cauchy-Green deformation tensor and the scalar parameter $\bar{E}_i$ characterises the isochoric strain in the direction of the mean fibre orientation for the i^{th} fibre family. Like for the incompressible model, the $(1 - 3\kappa)(\mathbf{a}_i \otimes \mathbf{a}_i)$ component of $\mathbf{H}_i$ is active only when $\bar{\mathbf{C}} : (\mathbf{a}_i \otimes \mathbf{a}_i) > 1$.

4.3.3 Cohesive zone elements

Cohesive zone models are based on the idea of a process zone within the material, ahead of the physical crack tip. Material fracture is regarded as a gradual process in which formation of new crack surfaces takes place along an extended virtual crack, and the separation of these surfaces is resisted by cohesive tractions [140]. The traction across the cohesive zone increases with increasing separation until a maximum, after which it irreversibly decreases until it reaches zero. This behaviour is governed by a suitable traction-separation law, as depicted in figure 4.9. The aortic media consists of highly organised repeating lamellae held together by bridging collagen fibres that show a gradual decrease of cohesive force after exceeding a load limit [59]. This behaviour aligns well with the CZ concept and consequently dissection has often been simulated using this method [59, 60, 141, 142]. In this work the cohesive zone formulation in MARC 2014 was utilised. Here an effective traction t and effective opening displacement δ are related by

$$t = \frac{\delta G_c}{\delta_c^2} e^{-\delta/\delta_c}, \tag{4.8}$$

where δ_c is a critical opening displacement, and G_c is the critical energy release rate. Evaluating (4.8) at the critical opening point δ_c yields a corresponding critical traction t_c for the material:

$$t_c = \frac{G_c}{\delta_c \exp(1)}. \tag{4.9}$$

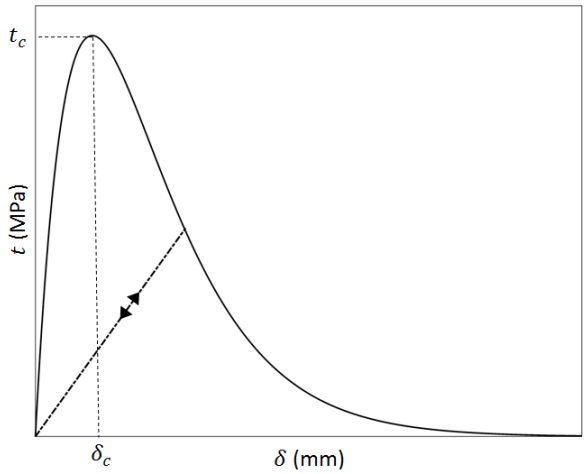

Figure 4.9: Traction t versus separation δ plots for an exponential CZ law [3]. The traction t increases until the critical separation (opening) δ_c. After this t decreases for increasing δ and the cohesive zone is irreversibly damaging. Correspondingly, once δ exceeds δ_c, unloading follows a new path that is different from the initial loading path (dot-dash line).

If there is no mixed-mode behaviour, as assumed here, then δ can be defined as $\delta = \sqrt{\delta_n^2 + \delta_t^2 + \delta_s^2}$ where δ_n is the normal displacement and δ_s and δ_t are the

tangential displacements, all expressed with respect to the local element system. Similarly, t_n, t_s and t_t can be found from t as

$$t_i = t\frac{\partial\delta}{\partial\delta_i} \quad i = n, t, s. \tag{4.10}$$

Constitutive parameters k_1, k_2, μ, and κ assumed the optimised values for control specimens derived in chapter 2 (table 2.4a). Nominal CZ model values were taken to be $G_c = 183.3$ J/m^2 (taken from chapter 3) and $\delta_c = 0.129$ mm [59]. The latter has also been previously used in FE CZ approaches to modelling arterial dissection [59]. G_c and δ_c were used to describe the CZ element behaviour as these are the inputs for the formulation in MARC 2015. CZ parameters were not acquired directly from the experiment due to the complexity of the loading and the tissue deformation being obscured. Furthermore, the chosen parameters should be validated, for example, by calculating t_c and comparing with an experimentally measured value or a value from the literature. However, as mentioned the complex loading prevents this from being calculated from the experiment and as shown later in chapter 5 CZ values are highly dependent on loading applied and thus literature values can not be used. Thus, this is a limitation in the CZ modelling which is partially addressed in chapter 5 by simplifying the geometry driving the dissection. The friction coefficient γ was initially assumed to be 0. The sensitivities of the model prediction to variations in values of key parameters (specifically, k_1, which dominates the elastic response, G_c, which governs the rupture behaviour, and γ, which influences the contact behaviour) were additionally explored.

4.3.4 Results

Figure 4.10 depicts the progressive penetration of the tissue sample by the catheter over the course of the simulation. Figure 4.11, in turn, shows the experimental F_R versus U_{cath} data plotted with model predictions for each combination of parameter values. These combination of values were selected to demonstrate the effect of these key parameters. However, many material parameters resulted in the model not converging. This combined with lengthy model solution times, hindered further investigation of material parameters and is a primary justification for reducing model complexity in chapter 5. The effects of these parameter values are reviewed.

Initial parameter values. Using initial parameter values, it can be seen clearly that the maximum predicted F_R is approximately eight times lower than the experimental value. Through-penetration also occurs after a displacement of approximately half that of the experimental value. Moreover, the predicted curve shows a much flatter profile than does the experimental one. The latter feature, in particular, is likely attributable to the absence of friction, meaning the progressive rupture phase is dominated by the rupture parameters. The drop in reaction force to zero following

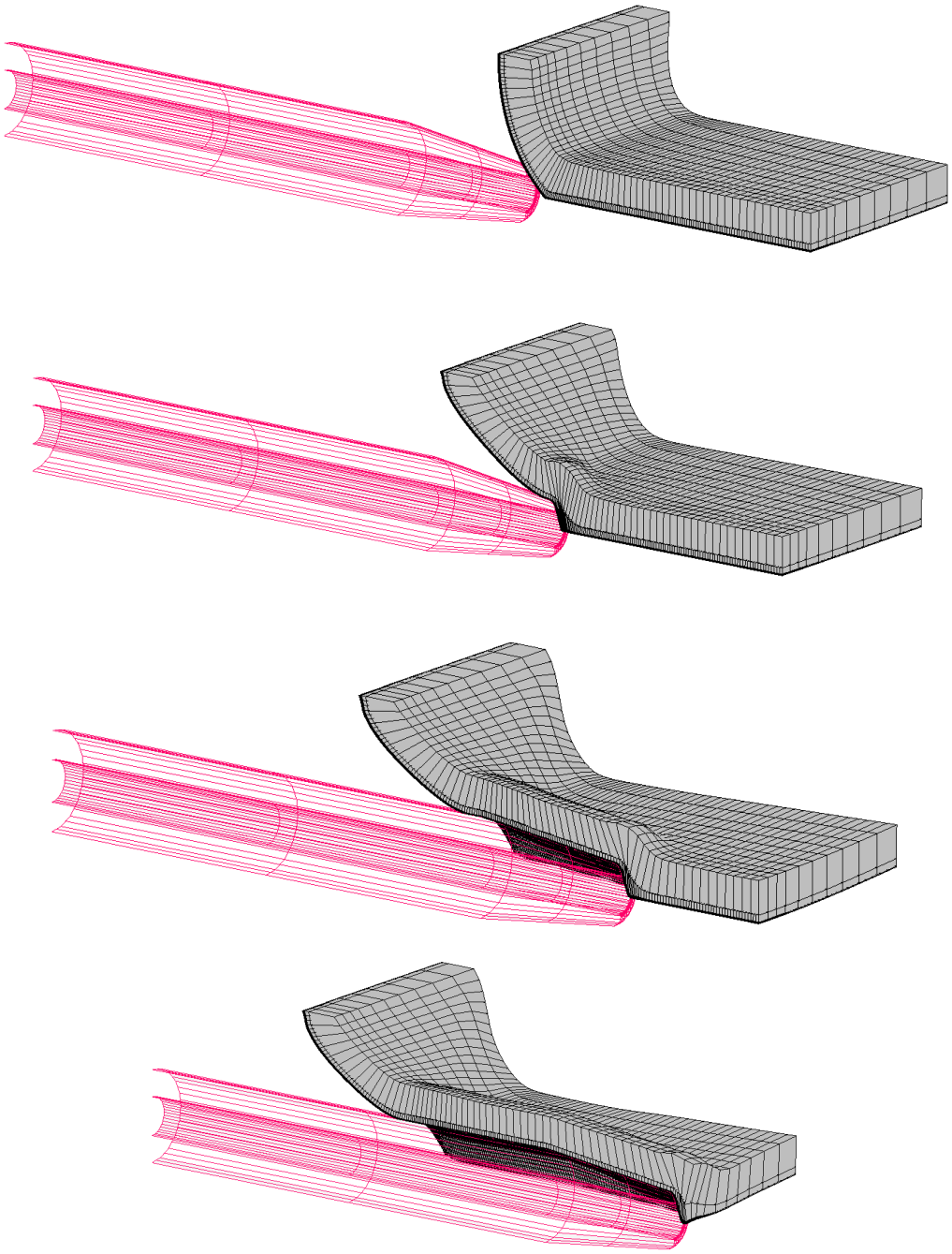

Figure 4.10: Simulation results for initial parameter values at various stages. CZ elements are not rendered, to improve clarity.

through-penetration suggests similarly.

Non-zero friction. A friction coefficient of 0.1 ($\gamma = 0.1$) was used as a representative value by assuming approximately twice the value found in [143]. This was used as it was difficult to estimate γ from the experimental curve. This is because while the frictional force can be easily found from the "friction only" region, the compressive force on the catheter is unknown. FE may be used for this purpose however it is highly likely that the compressive force is dependent on the CZ parameters and the constitutive model parameters. These must be determined from the experimental

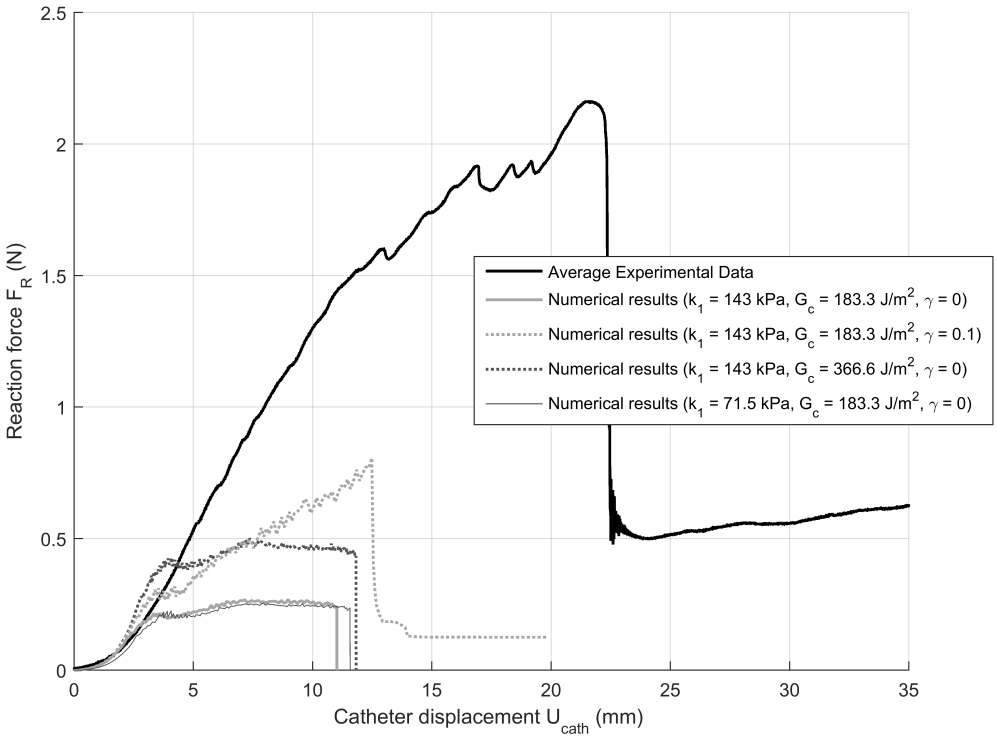

Figure 4.11: Experimental force-displacement data plotted with numerical model results for various combinations of model parameters. Initial parameter values were taken to be $k_1 = 143$ kPa, $G_c = 183.3$ J/m^2, $\gamma = 0$. Subsequently, model sensitivity to each was explored in turn by: 1) setting $\gamma = 0.1$; 2) doubling G_c; and 3) halving k_1.

curve requiring optimisation procedures with high computational cost due to the slow solution time of the model. Finally, if γ is too large then model stability is effected and convergence is difficult to achieve. This is likely because of the higher frictional forces leading to greater residual forces and element distortion.

A non-zero friction indeed produces an increasing reaction force during the rupture phase which is qualitatively similar in profile to the experimental result. A non-zero reaction force following through-penetration is also observed, as expected. The overall force magnitudes, however, remain well below the experimental values. The end displacement, similarly, remains over low. The "friction only" region (following through-penetration) of the experimental curve, however, suggests that frictional effects do not in any case dominate the overall response, contributing around 0.5-0.6 N to the overall peak of approximately 2.2 N. Other mechanisms, and corresponding parameters, must therefore account for a large portion of the difference between the experimental and numerical curves.

Doubling G_c. During the rupture phase, the maximum reaction force is necessarily governed by the force required to rupture the tissue, and correspondingly by the critical energy release rate G_c. Thus, doubling G_c effectively doubles the predicted reaction force, as shown. However, like with γ if G_c is too large then the model

becomes unstable and does not converge. For instance, utilising parameters from chapter 5 does not give model convergence. This is likely because a higher G_c requires greater force to open the CZ elements and greater residual forces and element distortion.

Halving k_1. The material stiffness appears to have only a small effect on the overall response, as illustrated by the halving of k_1. The peak reaction force is virtually unchanged. Only the maximum displacement is extended slightly. The effect of k_1 on model convergence is not as clear as with γ and G_c and must be carefully selected to ensure model stability.

Recapitulation. The salient features of the foregoing are that 1) tissue stiffness influences reaction force very little; 2) friction leads to increasing reaction force during rupture, and non-zero reaction force following through-penetration; and 3) critical energy release rate governs the overall force magnitude. It could be speculated, therefore, that optimising the latter two parameters, in particular, might lead to good agreement between experiment and model. However, pursuing this approach in practice quickly leads to parameter values that are difficult to accept from a physical point of view and difficulties with model stability, quickly leading to convergence problems. The friction coefficient employed above, for example, was already over twice the value reported for artery wall on steel [143], and apparently still well below the requisite value. Similarly, the maximum G_c value employed was double that obtained in independent tests on very similar tissue (chapter 3), but still produced a reaction force well below the experimental magnitude. The physical fidelity of an underlying formulation which apparently requires such inflated parameter values must correspondingly be questioned. In the next section, therefore, a more sophisticated CZ formulation was employed in an attempt to achieve good association between numerical and experimental data while obtaining model convergence.

4.4 Numerical modelling using a large opening displacement CZ formulation

4.4.1 Formulation

As described in section 4.3.3, a key element of the CZ formulation is computation of the opening displacements δ and corresponding tractions t, and their respective normal and tangential components. These are achieved by defining a local reference system for each CZ element, which is generally either the mid-line of the element, or its top or bottom edge, and computing opening displacement components accordingly. This approach is used in MARC, ABAQUS, and most other commercial FE packages. When crack opening displacements are small, as is the case in brittle fracture of stiff materials, the choice of coordinate system is immaterial. However, Van den Bosch et

al. [144] showed that for large opening displacements, as encountered in rupture of highly deformable materials, as here, such formulations do not produce consistent or unique displacement and traction magnitudes, leading in turn to substantial errors in the calculation of energy dissipation in the system. The same deficiency also leads to errors in the evaluation of integrals of tractions over the element domains when displacements are large. Thus, while the formulations of underlying bulk elements are indeed robust under large deformations, being founded on valid, geometrically nonlinear continuum theories, standard CZ FE formulations may be deficient for large opening displacements. Correspondingly, it was speculated that the behaviour of the initial model described above was attributable to this cause, and the large-displacement CZ formulation presented by Van den Bosch et al. was explored instead.

Identifying the use of local bases as the cause of the difficulties, Van den Bosch et al. [144] developed a formulation in which opening and traction vectors are instead resolved globally. Correspondingly, no distinction is made between normal and tangential directions with respect to the element. Defining traction $\mathbf{t} = t\mathbf{e}$ and separation $\boldsymbol{\delta} = \delta\mathbf{e}$ vectors, where $\mathbf{e}$ is a unit vector along the line between associated opposing points of the interface, magnitudes t and δ are then evaluated according to 4.8, as before. Tractions are formulated as first Piola-Kirchhoff tractions, allowing, for example, CZ initial lengths to be used unambiguously in integral evaluations. A MARC user subroutine implementation of this formulation, developed by Marco Van den Bosch and previously used, for example, in analysis of delamination in flexible electronic circuits [144], was deployed within the CID model, and the analysis was repeated. Additionally, as stated later in section 5.3.2, convergence was achieved with this formulation in the simplified wedge scenario and not for the small strain formulation lending further justification for this approach.

An alternative approach that captures behaviour of intermittent fibres is to utilise multiscale methods where the CZ model is split into micro and macro descriptions. At the macro-scale the interface (with predefined geometry) is modelled with cohesive zone elements of which the traction–separation response is obtained from the underlying micromechanical model. However, this adds a further level of computational complexity and may also have the same problems as traditional CZ formulations, identified in chapter 5, when contact drives the crack propagation.

4.4.2 Numerical performance

Using the large displacement formulation, a simulation of the *complete* penetration process could not be achieved: convergence failed after a penetration of approx. 1 mm - attributable to various numerical difficulties, such as mesh distortion, as described below. Nonetheless, the model revealed a number of more fundamental issues with this approach to penetration modelling, associated with constitutive

behaviour and the fidelity of the contact interaction within the rupture zone. These are explored below.

Constitutive behaviour. Figure 4.12 shows the model at the last converged time step. A patch of elements in the vicinity of the catheter tip exhibit expansion that does not match the expected behaviour for this loading. This behaviour can also be seen with the small displacement CZ formulation in figure 4.10, however, as the element distortion is relatively small in that case, the expansion is minimal and does not impact model convergence. While the GOH strain energy potential has been employed extensively in artery models, and behaves well in most physiological conditions, the phenomenon just described has in fact been identified previously as a deficiency of the model under certain conditions [70]. Specifically, when fibre angle with respect to the loading direction $\theta \in [30°, 60°]$, as here, the rotation of the fibres with loading leads to unphysical expansion of the element perpendicular to the fibre plane.

That this is indeed the origin of the effect observed here is demonstrated by switching to a simpler neo-Hookean formulation (corresponding, in fact, to the Ψ_m component of 4.3), which leads to the result in figure 4.12 (bottom). The non-physical element expansion no longer appears. While the constitutive response of the model tissue in this case clearly will differ from that of the real tissue, it enables the overall model convergence to be explored further.

Element distortion in regions of contact. Switching to a neo-Hookean constitutive model, and using a physiologically reasonable value for the shear modulus $\mu = 0.4$ MPa [145, 146, 147], still does not lead to convergence across the entire penetration process. In addition, varying μ by an order of magnitude does not yield an improvement in model convergence. The major cause of this appears to be excessive element distortion adjacent to the catheter tip, as highlighted in figure 4.13. This distortion is partly a consequence of the relatively complex geometry of the catheter tip and the rupture surface with which it interacts, and of the resulting contact area between the two. Additionally, it is practically difficult to verify that the interaction between the contact body and continuum elements indeed reflects the experimental conditions, since the catheter tip is concealed within the tissue.

Catheter penetration of CZ elements. Finally, and arguably most pressingly, the catheter appears to interact with the CZ elements in a non-physical manner. Specifically, since the CZ element leading edges do not themselves support contact (contact is rather handled by a layer of elements on the surface of the bulk tissue elements), the catheter is able to penetrate the CZ elements when they are only partially damaged - i.e. prior to their physical dissection (rupture). As the catheter progresses, these penetrated elements are indeed further opened, so that eventually they *can* achieve their rupture displacement. But, the transient behaviour nonetheless is non-physical. This can be further visualised with the aid of figure 4.14, which

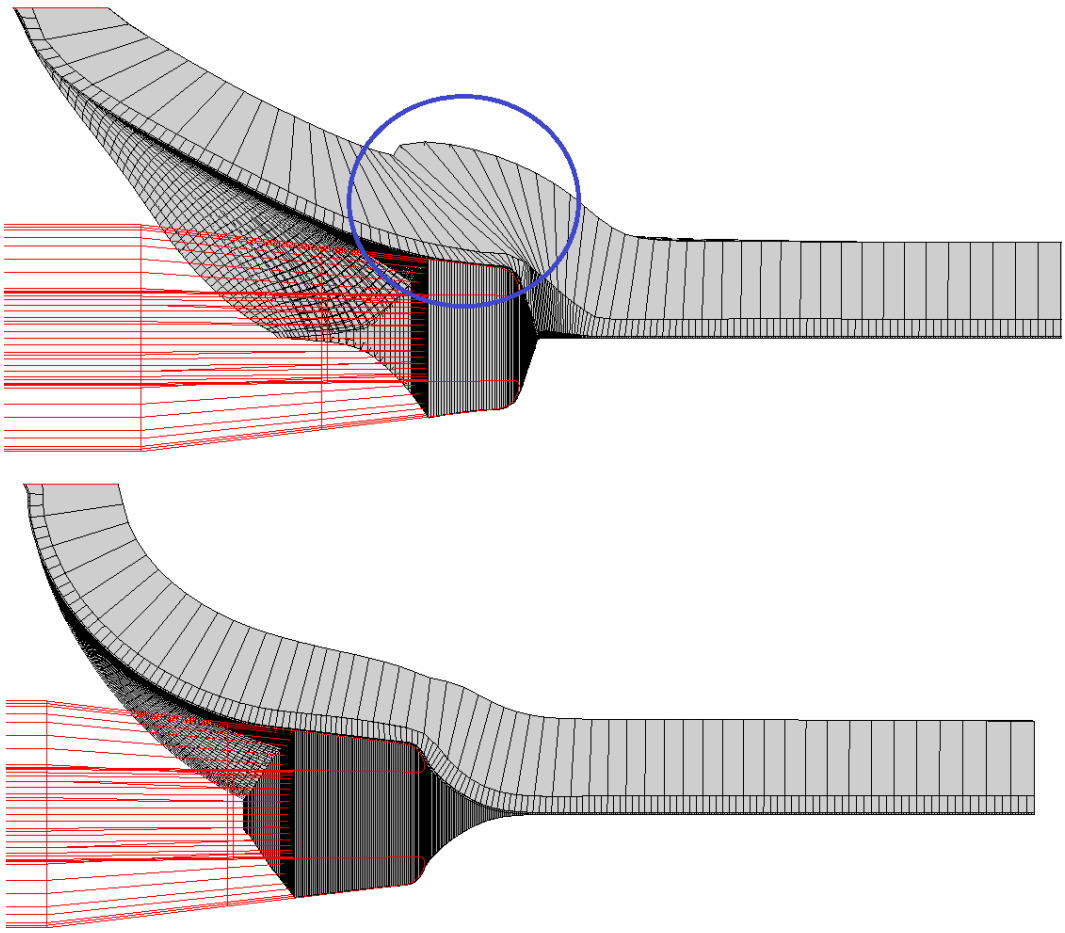

Figure 4.12: Results for GOH constitutive model with fitted parameters from chapter 2 (top) compared to those of an isotropic constitutive model (bottom). A large expansion of elements (circled) can be seen above the catheter contact body tip resulting in a profile that does not align with the expected response to the loading applied.

depicts the damage levels sustained by a series of CZ elements in a peeling model, and in which only the first, CZ0, has fully ruptured. In the CID model, if the catheter diameter is sufficiently small, nothing prevents it from penetrating some of the partially damaged elements CZ1-CZ5.

At least two consequences of this behaviour can be immediately deduced. Firstly, the geometry of the rupturing tissue at the "crack" tip, immediately ahead of the contacting catheter tip, is likely quite different from that of the real tissue. Given the importance of this geometry from the point of view of the catheter-tissue contact behaviour, and as regards in turn the crack tip mechanical environment and the rupture behaviour itself, the effect needs to be better understood.

Secondly, the traction-separation behaviour of the elements (figure 4.14) is directly linked to the work associated with the rupture process: the area beneath the traction-separation curve equals the energy dissipated during damage and subsequent rupture, and the parameters of the curve are tuned in turn to match experimental measurements of the tissues' critical energy release rate. Thus, if the catheter

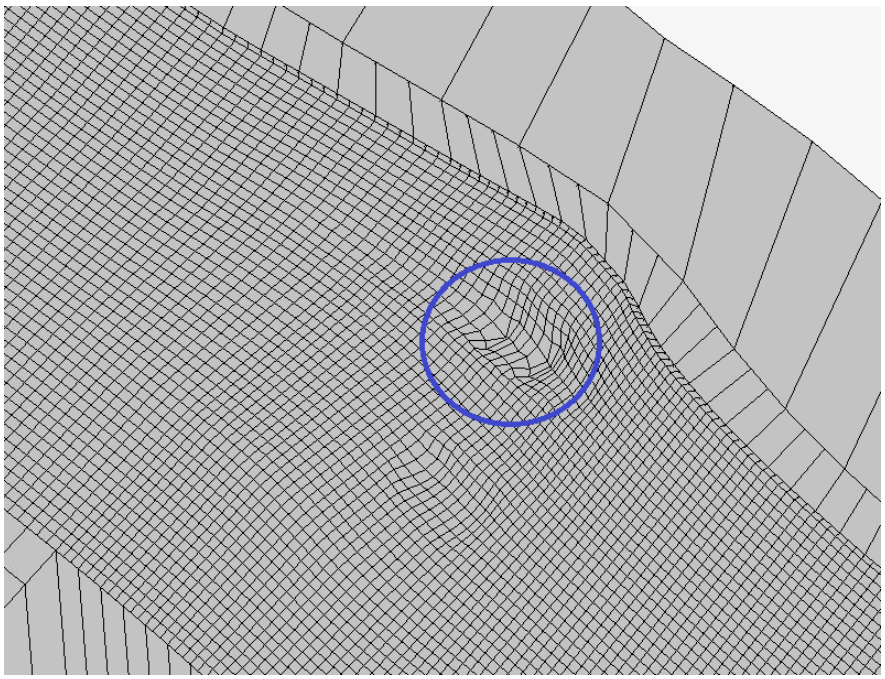

Figure 4.13: Element distortion at contact with catheter, contact body and CZ elements have been removed from image for clarity. Elements are highly distorted possibly leading to poor model convergence.

diameter, which determines the extent of the CZ opening, is smaller than some threshold value (i.e. if the elements actually *never* rupture), the elements will "expend" less energy than they should, and the reaction force on the catheter may be correspondingly lower. As noted by Oldfield et al. [63], this effect may in principle be minimised by choosing a very small critical opening displacement δ_c (for a given G_c). However, this also leads to even more severe numerical instability, and therefore appears practicable only up to a point. A clearer understanding of the effect of δ_c on both convergence behaviour and energy dissipation when simulating soft tissue penetration with CZ models is therefore required.

4.5 Conclusions

Two key points emerge from the analysis in the previous section:

1. Element distortion resulting from the complex interaction between the tissue and catheter contributes to difficulties in achieving convergence across the complete dissection simulation. The fidelity of the interaction is also doubtful, for several reasons. Verifying this interaction with respect to the experimental conditions involves obvious practical difficulties using the present configuration.

2. The penetration of the CZ elements by the catheter is clearly non-physical, yet appears unavoidable with the current CZ element formulation: the penetration may be minimised, but never eliminated. Further investigation is needed to understand the nature of this limitation and whether it is indeed acceptable.

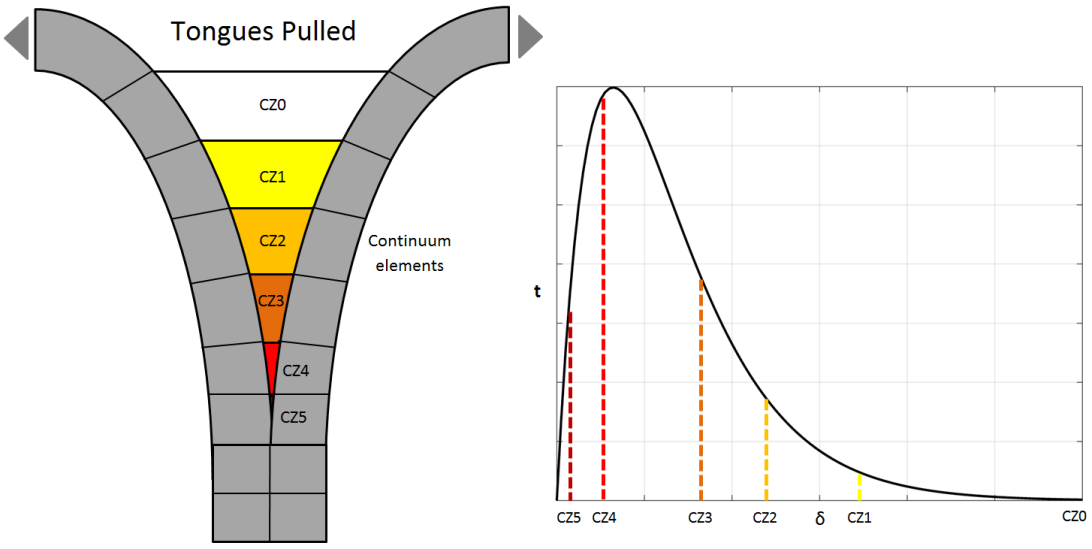

Figure 4.14: Schematic of cohesive zone damage with increasing separation. CZ0 - CZ5 are cohesive zone elements with decreasing separation and damage. Left. Simplified mesh of a controlled peeling scenario with separation increasing from burgundy CZ5 element to white CZ0 element. Right. Associated traction-separation law with status of each CZ element labelled.

To further explore these points, therefore, in the following chapter a simplified dissection configuration is conceived, which removes much of the geometric complexity of the system, while retaining the key feature of tissue rupture driven by a relatively stiff external body. The catheter is replaced by a planar wedge with a rounded leading edge, which affords both a greatly simplified model geometry (in fact, a 2D plane strain approximation is possible), and more direct assessment of the contact conditions. Additionally, this simplification results in a far lower solution time for the FE model allowing the effect of various model properties (such as material parameters and mesh densities) on model convergence to be investigated more thoroughly. Elastic material parameters could also be fit to the experimental data in a relatively short amount of time unlike with the current 3D model where the optimisation procedure would take over a month to complete. The outcome of this is that with further time the results and observations from the proceeding chapter would be utilised to improve convergence in this work. Finally, future work will investigate whether an explicit solver will give a converged solution. This is because compared to an implicit solver, an explicit solver handles non-linearities such as contact with relative ease and may alleviate the convergence issues. Hernández and Peña utilised an explicit solver to successfully model deep perforation of the vena cava using CZ elements [138]. The similarities between this work and that by Hernández and Peña lends confidence that explicit methods may yield a converged solution for this problem.

Chapter 5

Simulation of arterial dissection by a planar penetrating external body using cohesive zone modelling

5.1 Introduction

Percutaneous coronary intervention (PCI) is a common treatment for atherosclerotic coronary arteries that has showed increasing prevalence in the UK over the last 20 years [148]. In this procedure, a guide wire is fed to the region of interest, followed by a catheter which travels along it. During this part of the procedure both the catheter and guide wire can make contact with and damage the blood vessel wall to varying extents. The most benign scenario involves simple rubbing against the endothelial layer, the complications of which can include platelet aggregation and thrombus formation. An example of more catastrophic damage is dissection: the separation of blood vessel layers.

In the previous chapter, some complexities associated with simulating catheter-induced dissection of arterial tissues were elucidated. Promising experimental results were obtained however, numerical analysis proved difficult. Some common difficulties associated with soft tissue models (viz. large element distortions and nonlinear constitutive responses) played a role in hindering a converged solution. But, the interaction between tissues and catheter in the vicinity of the cohesive zone, and in particular the apparently unphysical penetration of "intact" (i.e. not actually ruptured) CZ elements by the rigid contact body, was identified as perhaps the major source of numerical instability. This in turn raised doubt about the fidelity of the geometry of the ruptured tissues themselves in the vicinity of the "crack tip" with respect to the real experiment, which is difficult to resolve with the existing experimental configuration. The complexity of the catheter tip geometry further exacerbates this issue. Compared with other successfully simulated dissection scenarios, such as simulations of peel test experiments, the salient feature, and confounding factor, in the present case is the presence of an external body (catheter) driving the dissection. To further explore the viability of CZ elements in such scenarios, therefore, it was proposed, first, to study a mechanically simpler dissection problem that nonetheless retains the key feature of interaction between rupturing tissues and a relatively stiff external body. To this end, in this chapter, dissection of aortic tissues by means of a planar, rigid wedge, with a rounded leading edge, is investigated. The simpler geometry of the contacting bodies in this configuration means the fidelity of the model with respect to experimental conditions may be ensured with more confidence. The scenario may also be formulated as a plane strain problem, further simplifying analysis. The performance of the CZ approach to rupture modelling was studied in this context.

A series of wedge-induced dissection experiments was first conducted (section 5.2) to obtain data with which to validate subsequent models. A FE model of the experimental configuration, employing a CZ description of the rupture process was then developed (section 5.3). Next, a novel parameter estimation procedure was formulated, based on simplified FE models of the various experiment phases

(section 5.4). Finally, the CZ model predictions were compared with experimental observations (section 5.5). The remainder of the chapter is organised under these headings, and concludes with a discussion of the viability and limitations of CZ formulations in such scenarios.

Figure 5.1: Aluminium wedge used to drive dissection, the rounded edge can be seen in the left of the image.

5.2 Wedge dissection tests

5.2.1 Experimental configuration

Ex vivo dissection of samples of porcine aorta by means of a rigid wedge was conducted using the apparatus illustrated in figure 5.2. Partially dissected tissue samples were clamped between the two towers, as shown, and an aluminium wedge was driven between them, forcing their dissection. The wedge can be seen in figure 5.1. The dimensions were: length: 95 mm length, width: 40 mm, thickness: 2.5 mm. The thickness was chosen to approximate the diameter of an endovascular catheter. The front edge of the wedge that propagates the dissection was rounded.

5.2.2 Specimen preparation

Tissue samples were tested no more than 24 hours after the slaughter of the animal and were stored in a refrigerator in the interim. As in previous chapters samples were taken from the upper thoracic aorta proximal to the heart to have sufficient thickness. However, arteries further from the heart have different peeling properties to those closer, see table 3.4. This variation between samples is likely present even with samples from relatively similar locations along the arterial tree and may explain variation between samples seen later. The tissue was prepared by removing excess connective tissue and cutting axially such that the vessel wall opened into a rectangular section. This was cut into 40 mm by 20 mm specimens and washed

three times in saline solution. Each sample was partially dissected by creating a small incision with a scalpel and then manually pulling apart the newly created tongues, allowing enough free tissue on either side of the tear to be held by the testing apparatus (figure 5.2). The un-dissected sample length (distance between tear opening and end of the sample) was approximately 10 mm. This was chosen to provide sufficient tissue to dissect, allowing a plateau region to develop in the force-displacement curve, while ensuring wedge displacement, before full separation of the tissue halves, was not so large that the wedge reached the base of the holding apparatus. All samples were partially dissected immediately prior to the test and were again placed in saline solution to moisten before being placed in the holding apparatus. During dissection, the tear was kept in the middle of the media. The tissue was initially dissected and mounted such that the wedge would progress in the vessel axial direction. Reaction forces on the wedge were measured using a 20 N load cell as the wedge was displaced at 1 mm/s, and until the tissue was completely dissected. If there was an error the run was stopped and the data were discarded. Examples of errors include the tissue slipping from the clamp or the tissue tearing irregularly. Results for 11 specimens were recorded in this way.

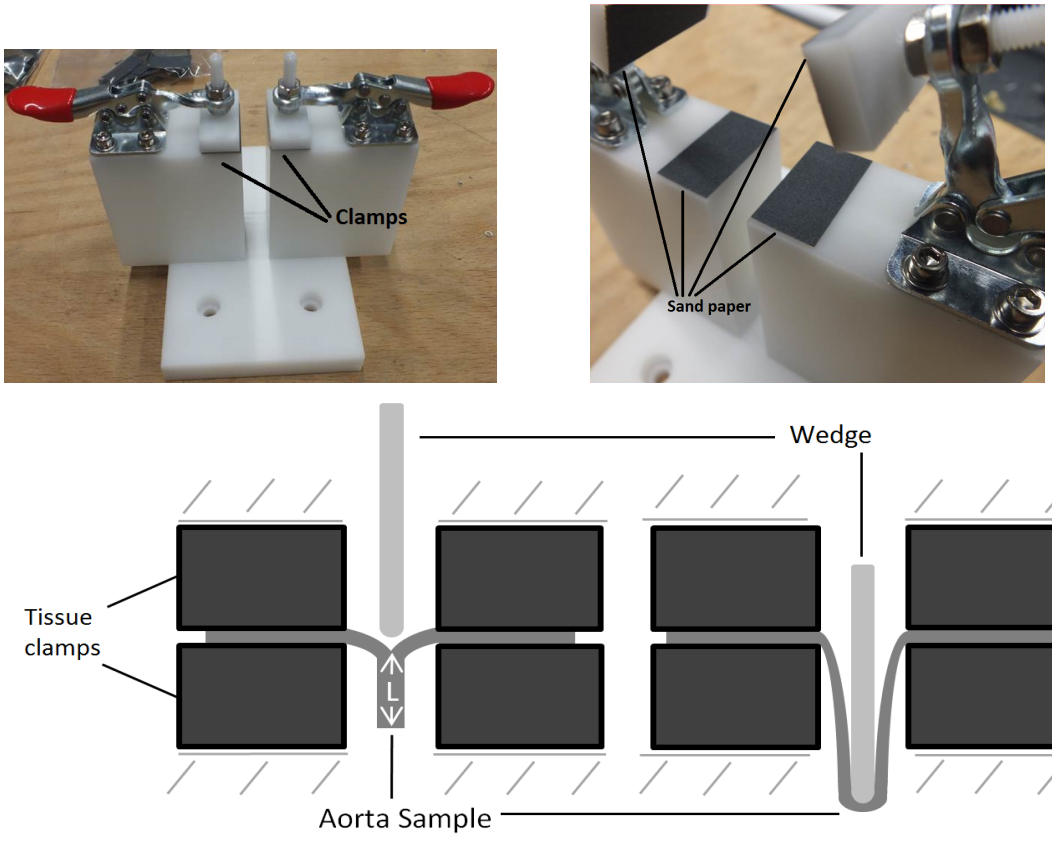

Figure 5.2: Top. Apparatus for holding tissue in place. Clamps hold the tissue tongues and the tissue to be dissected lies in the gap between the two towers. Sand paper was used to prevent slippage. Bottom. 2D schematic of wedge dissection test before loading is applied (left) and during the test (right). The set-up extends out from the page. L is the initial tissue length (10 mm).

5.2.3 Results

The resulting force displacement plot is presented in figure 5.3. All curves initially (up to displacement U_I) show the classic increasing stiffness characteristic of fibrous tissues [139], and which results from unfolding and subsequent stretching of collagen and elastin fibres. This is followed by a levelling off, as fracture begins (displacement U_I to U_T), and then a sporadic plateau region as fracture continues (displacement U_T to U_P). Finally there is a drop, either sudden or gradual, depending on the extent of fibre bridging, as the wedge fully separates the tissue halves. These features are identified in figure 5.3.

Raw experimental curves were averaged, as shown in figure 5.3, and the latter values were used in subsequent analyses.

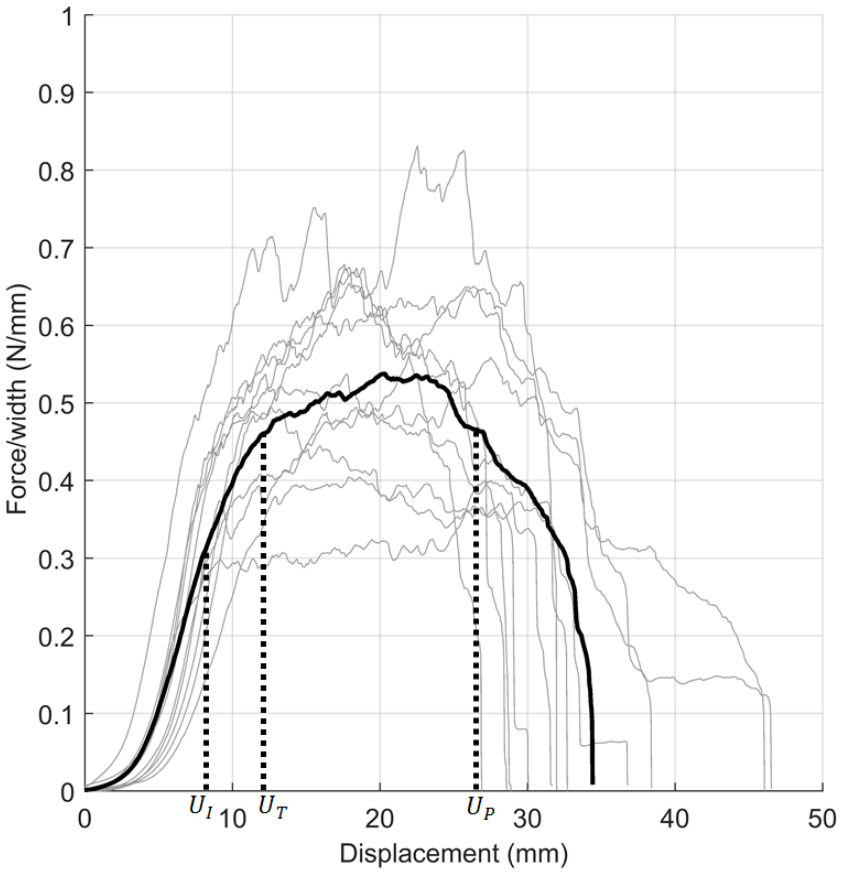

Figure 5.3: Experimentally measured reaction force/width versus wedge displacement for the 11 specimens tested. Raw experimental curves (grey) are overlaid with averaged curve (black). Also detailed on the average plot are the four identified stages in the wedge propagated dissection process: initial stretching (0 to U_I), before tissue begins to split; transition (U_I to U_T), where damage is initiating, identified by a decrease in the curve gradient; plateau region (U_T to U_P), wherein tissue is splitting and dissection is propagating; tissue splitting and dissection propagation; separation (U_P to end), characterised by a relatively sudden drop in reaction force, as the tissue tongues separate completely. The suddenness of the latter phase depends on the density and strength of the remaining bridging fibres between the tissue tongues.

5.3 Computational modelling of wedge-induced dissection

The wedge-induced dissection process was simulated using a CZ-based FE model, created within MSC MARC 2015. One half of the sample was modelled, reflecting symmetry about the X-axis, as described previously in chapter 4 (figure 4.8). A schematic of the model, associated dimensions, and boundary conditions is shown in figure 5.4. The model consisted of 12030 4-node quadrilateral elements and 1920 4-node CZ elements and the solution was performed with a non-linear implicit solver. As the wedge was assumed rigid, it was modelled by a geometric contact body and plane strain conditions were enforced. Fine and coarse regions of the mesh were connected by nodal ties. Mesh convergence analyses were conducted for all simulations. The model was assumed frictionless because no behaviours associated with high friction (e.g. stick slip and sudden jolts due to release of tissue held by frictional forces) were observed during the dissection experiments (section 5.2.1), when viewed under a low magnification stereo microscope. Finally, all models assumed symmetry along the dissection path. However, while the dissection propagated in the centre of the tissue, arterial dissection is a stochastic process that will result in asymmetric tearing. This was partially rectified by using average data such that it is hypothesised that the mean dissection path will be in the centre of the tissue.

5.3.1 Elastic tissue modelling

Tissue elastic response was modelled using an Ogden strain energy potential Ψ [3, 149]. Trial fits suggested that a two-term formulation was adequate to achieve good agreement with experimental results:

$$\Psi = \sum_{p=1}^{2} \frac{\mu_p}{\alpha_p}(\bar{\lambda}_1^{\alpha_p} + \bar{\lambda}_2^{\alpha_p} + \bar{\lambda}_3^{\alpha_p} - 3) + \frac{9}{2}K(J^{1/3} - 1)^2, \tag{5.1}$$

where μ_p are shear moduli and α_p are dimensionless constants such that the initial shear modulus $\mu = \frac{1}{2}\sum_{p=1}^{2} \mu_p\alpha_p$. $\bar{\lambda}_1, \bar{\lambda}_2, \bar{\lambda}_3$ are the isochoric, volume preserving, principal stretches, J is the Jacobian, and K is the bulk modulus. K was assigned a value of 10^9 kPa, representing near incompressibility.

5.3.2 Cohesive zone formulation

This model uses the same cohesive zone formulation as in section 4.4.1. Both large strain and small strain models were tested, however, for the parameters found in the latter sections, convergence was achieved with the large strain formulation and not

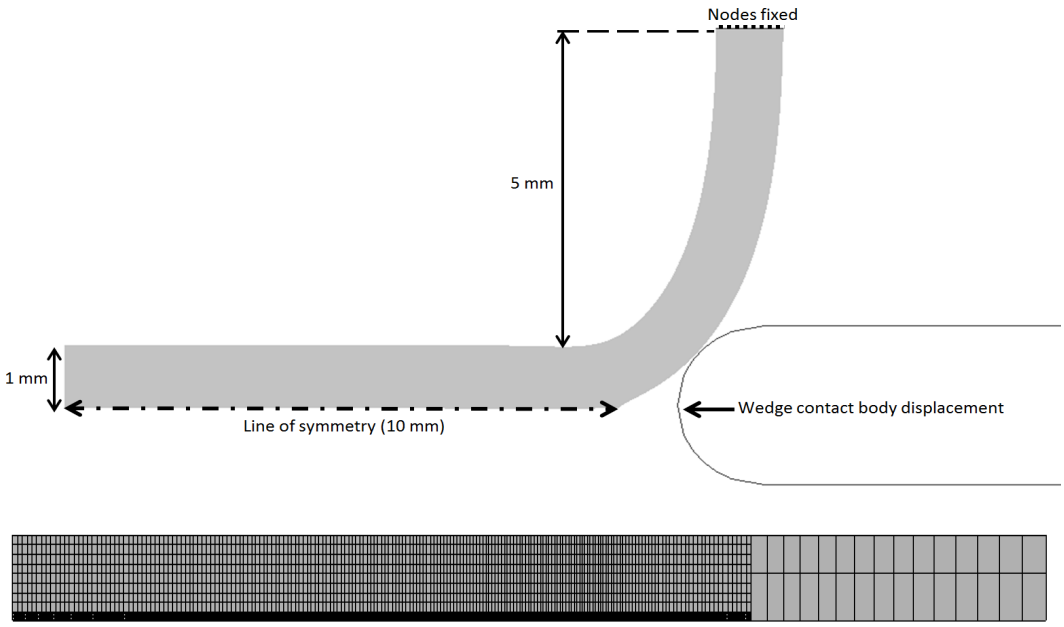

Figure 5.4: Top. Wedge dissection FE model with CZ elements immediately before force displacement data were recorded. The tissue strip was initially horizontal. The nodes indicated with a dotted line were first displaced into the position indicated, to represent the conditions at the start of the test. CZ elements are of zero thickness and their location is indicated by the dot-dash line. The wedge contact body displacement direction is indicated and the contact body extends out to the right of the image. Bottom. Initial model configuration, illustrating the fine and coarse meshes, which were bonded by means of nodal ties.

for the native small strain formulation. Thus, briefly, a large strain formulation was utilised where, unlike small strain formulations, the opening and traction vectors are resolved globally rather than with respect to a local basis, thus no distinction is made between normal and tangential directions. The traction vector $\mathbf{t} = t\mathbf{e}$ and separation vector $\boldsymbol{\delta} = \delta\mathbf{e}$, where $\mathbf{e}$ is a unit vector along the line between associated opposing points of the interface, are related by

$$t = \frac{\delta G_c}{\delta_c^2} e^{-\delta/\delta_c}, \tag{5.2}$$

where δ_c is a critical opening displacement displacement, and G_c is the critical energy release rate. Evaluating (5.2) at the critical opening point δ_c yields a corresponding critical traction t_c for the material:

$$t_c = \frac{G_c}{\delta_c \exp(1)}. \tag{5.3}$$

G_c can be acquired from the plateau region of the experimental force displacement curve (U_T to U_P). δ_c (or t_c) can be found from either the transition region (U_I to U_T) or from local deformations [150]. The ramifications of the parameter selection

in this study are discussed in section 5.5.

5.4 Model parameter estimation

5.4.1 Elastic tissue parameters

The elastic parameters (μ_p, α_p) of the tissue are identified from the experimental data by an inverse procedure. Figure 5.3 illustrates the main stages identified during wedge-driven dissection. The MATLAB optimisation toolbox was utilised to fit the constitutive response to data in relevant regions of the overall force-displacement profile; specifically, the initial elastic deformation stage (up to displacement U_I), and the estimated point of separation (U_P). Two simplified FE models, corresponding to the initial and separation portions of the tests were constructed to enable estimation of corresponding reaction forces (figure 5.5). The latter point (U_P) was included in the curve fitting as initial results showed that multiple parameter sets produced equally strong fits to the initial stretching region (0 - U_I). Therefore, including U_P restricted the candidate solutions and ensured model elastic behaviour had good association with experimental data up to U_P as well as in the initial stretching region. However, it must be noted that both U_I and U_P have been selected through inspection by observing the curve magnitude, gradient and surrounding behaviour of the curve at a given point. Therefore, they may not represent the actual points of transition and separation on the average data. In particular, the fibrous breaking around U_P renders it difficult to select a point at which the tissue tongues have begun to separate. Additionally, all calculations are performed on average data and thus the individual behaviour of the tissue in each test is not accounted for. As such, the separation in the average data is a combination of all separation behaviour in each test adding further difficulty in identifying U_P.

Models for initial and separation stretch phases

In the initial stretching phase, the two clamped tissue tongues are stretched as a result of the downward displacement of the wedge. The finite element models of this are based upon schematics A and B in figure 5.5 and the mesh can be seen in figure 5.6. The contact body is displaced in the -X direction to a value of U_I. The wedge-tissue interface is assumed frictionless.

At U_P the wedge load is completely supported by the stretching of the two clamped tissue tongues resulting from the downward displacement of the wedge. Their un-stretched length is L_P + (initial tongue length), where L_P is the length of tissue dissected by the wedge at U_P. Therefore, their summed reaction forces should equal the corresponding reaction force on the wedge measured in the experiments. However, L_P is not known and thus has to be approximated using upper and lower

values. The upper bound assumes that at U_P the tissue has completely separated and thus $L_P^1 = L$. The lower bound assumes that the minimum amount of tissue has been dissected at U_P. This is calculated assuming a linear relationship between U_P and L_P such that

$$L_P^2 = \frac{L(U_P - U_T)}{U_{max} - U_T}, \tag{5.4}$$

where U_{max} is the maximum value of displacement in the chosen data. For the average data in figure 5.3 L_P^2 =6.61 mm. The second FE model, simulating the experimental configuration at this point, is shown in figure 5.5 (C and D) for $L_P = L_P^1 = L$ and the mesh can be seen in figure 5.6. The contact body is displaced in the -X direction to a value of U_P. Again, the contact was assumed frictionless.

Curve fitting

The constitutive parameters $(\mu_1, \alpha_1, \mu_2, \alpha_2)$ were then fit to the average experimental force-displacement curve. This process was formulated as the optimisation problem

$$\mathbf{x} = \arg\min_{\mathbf{x}} \left\{ w_1 ||\mathbf{F}^{exp} - \mathbf{F}^{comp}||_2 + w_2 (F_{sep}^{exp} - F_{max}^{comp}) \right\}, \tag{5.5}$$

where $\mathbf{x}$ is the vector of tissue model parameters and $||\bullet||_2$ denotes 2-norm. $\mathbf{F}^{exp}$ is a vector of experimental reaction forces on the wedge in the initial stretching region (up to U_I) and $\mathbf{F}^{comp}$ is a corresponding vector of model-computed reaction forces (figure 5.5). F_{sep}^{exp} is the mean experimental force just prior to separation (displacement U_P) and F_{max}^{comp} is the maximum force within the "separation" FE model (figure 5.5). Finally, w_1 and w_2 are weighting parameters, manually tuned to achieve best fit to the initial elastic region whilst ensuring the force at separation closely matches the experimental value. The fitting was performed by the least squares non-linear optimiser within MATLAB. Upper and lower bounds were applied to reduce optimisation time and to prevent implausible material parameters from being selected. The optimisation procedure was performed over multiple, randomly assigned, initial guesses and the best fit was selected. This prevents the optimum solution being dependent on the starting parameters and increases the likelihood of finding the global minimum within the search space [86]. The fittings were performed for L_P^1 and L_P^2 separately yielding two sets of constitutive parameters.

The fitted curves, overlaid on the experimental data, are shown in figure 5.7 for L_P^1 and L_P^2. A good fit to each initial region can be seen and the peak of each $W_{elastic}$ area plot is close to the force/width at separation in the average experimental data. The optimised constitutive parameters for L_P^1 and L_P^2 are presented in table 5.1.

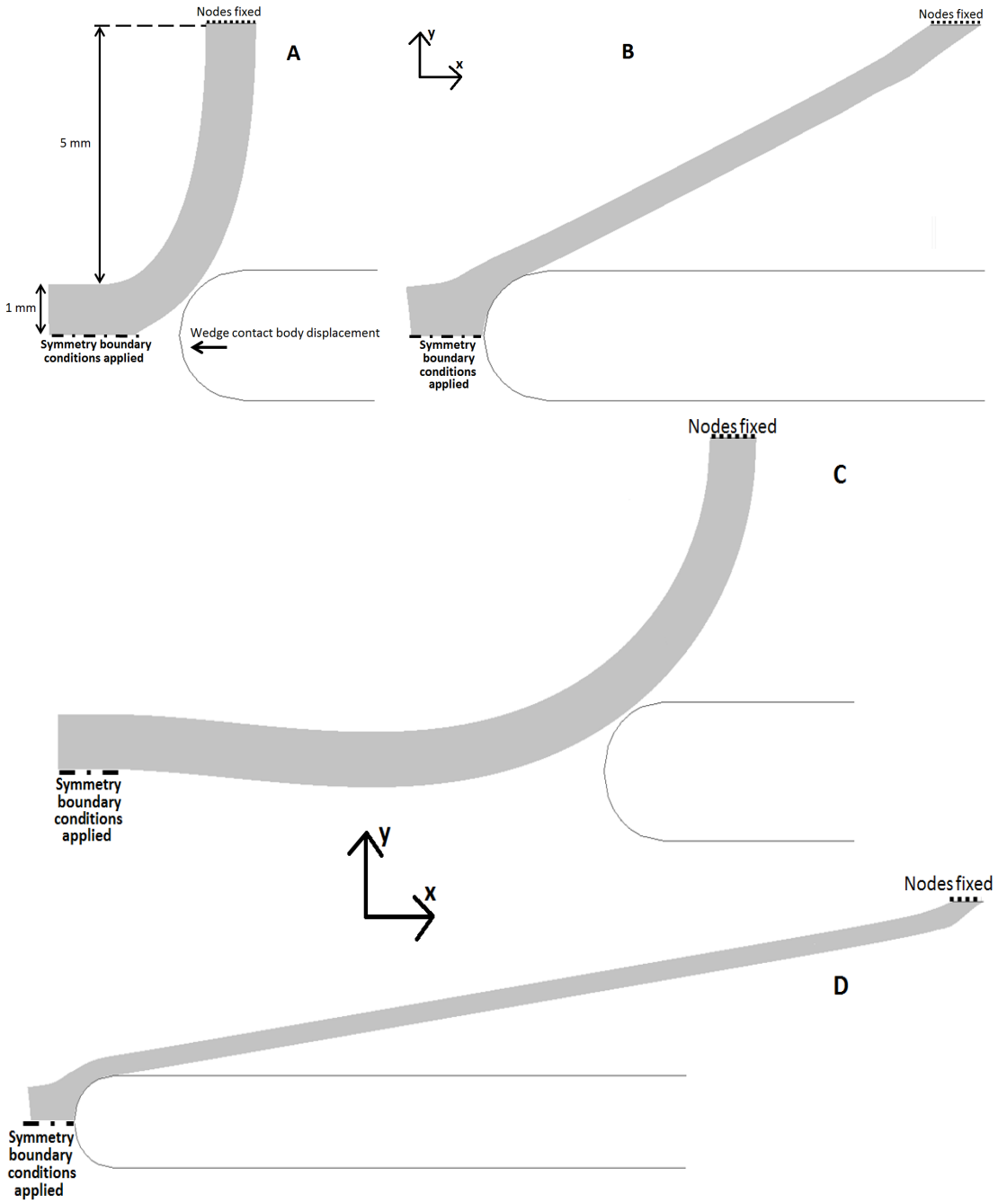

Figure 5.5: Schematics of the wedge dissection test in the initial stretching phase and at the end of the plateau region, identified in figure identified in figure 5.3 (for $L_P = L_P^1 = L$). Symmetry boundary conditions were imposed along the dot-dash line, the wedge contact body displacement direction is indicated and the contact body extends out to the right of the image. A: the model immediately prior to contact initiating. As for the complete dissection model (figure 5.3), the initially straight tissue strip is first displaced into the configuration shown, to represent conditions at the start of the test. B: the model at the end of the simulation, after displacing the wedge by U_I. C: the model immediately prior to contact initiating, and after displacing the indicated nodes (dotted line) into the starting test configuration. D: the model at the end of the simulation, after displacing the wedge by U_P.

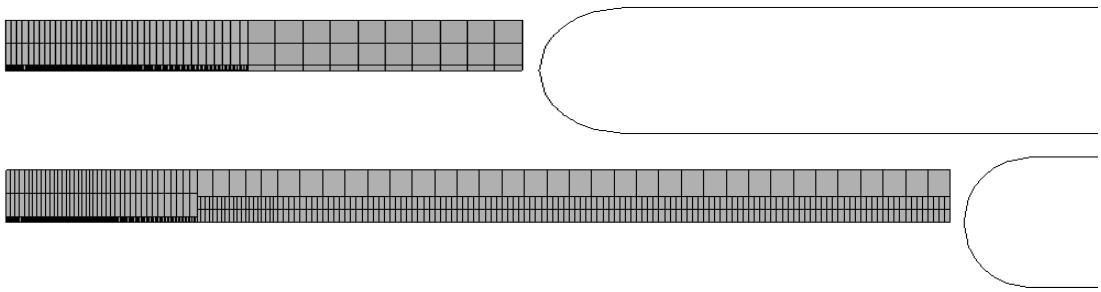

Figure 5.6: FE Meshes of the wedge dissection test in the initial stretching phase (top) and at the end of the plateau region (bottom), identified in figure identified in figure 5.3 (for $L_P = L_P^1 = L$).

Table 5.1: Dissection energy (G_c), critical opening displacement δ_c and fitted 2-term Ogden strain energy function parameters calculated for L_P^1 and L_P^2. Dissection energies are compared to the mean ± standard deviation from chapter 3.

	Wedge driven dissection		Chapter 3
	1	2	
G_c (J/m^2)	737.5	803.2	183.3 ± 64.2
δ_c (mm)	0.417	0.417	-
μ_1 (kPa)	0.12	6.19	-
α_1 (mm)	8.60	2.60	-
μ_2 (kPa)	13.69	21.27	-
α_2 (mm)	5.41	4.04	-

5.4.2 Critical energy release rate

To compute the critical energy release rate G_c associated with dissection of the tissue, the expression from [46, 48], developed for analysis of peel test data, was adapted to give

$$G_c = \frac{\Delta U}{\Delta a} = \frac{(W_{ext} - W_{elastic})}{L_P}, \tag{5.6}$$

where ΔU is the energy expended per unit width and Δa the crack length, at an arbitrary point during the fracture process. Evaluating at U_P in the experimental procedure gives $\Delta U = W_{ext} - W_{elastic}$ and $\Delta a = L_P$. W_{ext} is the external work per unit width done on the system, $W_{elastic} = 1/2 \int_\Omega \mathbf{P} : \mathbf{F}\ d\Omega$ (where Ω is the model domain, $\mathbf{P}$ the first Piola-Kirchhoff stress tensor and $\mathbf{F}$ the deformation gradient tensor) is the work expended by stretching the tissue up to the point of complete separation of the tissue layers (per unit width). W_{ext} is equated with the area beneath the force displacement curve up to the displacement U_P. $W_{elastic}$ is more complicated to compute, given the nonlinearity of the tissue mechanical response and the non-homogeneity of the deformation. In this study, it was estimated using finite element analysis.

$W_{elastic}$ is assumed as the total strain energy in the "separation" FE models. However, as L_P has a lower and upper value, $W_{elastic}$ also has two different values depending on L_P in the geometry of the "separation" FE models ($W_{elastic}^1$ and

$W^2_{elastic}$). Thus, G_c also has values for L^1_P and L^2_P

$$G^i_c = \frac{(W_{ext} - W^i_{elastic})}{L^i_P} \qquad i = 1, 2, \tag{5.7}$$

as represented in figure 5.7. The corresponding dissection energy values are given in table 5.1 alongside values from chapter 3 for peel testing of the same tissue type type, and with similar specimen geometries.

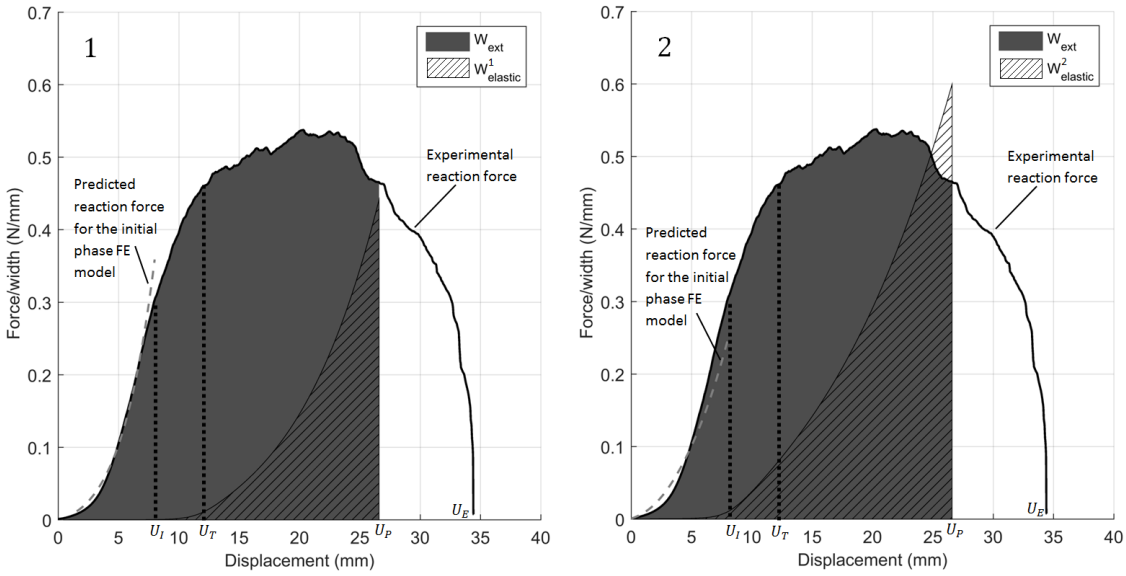

Figure 5.7: Reaction forces and estimated energies for L^1_P and L^2_P, identified by the respective numbering. The solid black curve shows the average measured wedge reaction force/width versus displacement; the grey dashed curve shows the model-predicted response during the initial stretching phase, using optimised Ogden constitutive parameters; the hashed area corresponds to the elastic energy $W_{elastic}$ stored in the stretched tissue just prior to separation; finally, the grey shaded area corresponds to W_{ext}. U_I, U_T, U_P and U_E are again identified for clarity.

Comparing G^1_c and G^2_c, it can be seen that $G^2_c > G^1_c$. This is because while $W^2_{elastic}$ is far greater than $W^1_{elastic}$ ($W^1_{elastic} = 2.35$ J/m and $W^2_{elastic} = 4.41$ J/m), L^2_P is far smaller than L^1_P and L has a greater influence on G_c.

When comparing G^1_c and G^2_c to the dissection energy values found for the control values in chapter 3, G^1_c and G^2_c are both approximately four times higher. One reason for this difference is that frictional energy dissipation was assumed negligible in the wedge tests, whereas its contribution to W_{ext} cannot be zero in practice. However, it is speculated this contribution alone cannot fully account for the greater G_c in the wedge configuration, given the absence of obvious friction-associated behaviour in the experiments, as mentioned. Additionally in chapter 3, $W_{elastic}$ was calculated by assuming a linear constitutive response (based on the presentation in [46]), while here the material behaviour was captured using a more realistic hyperelastic constitutive model. Thus, $W_{elastic}$ is unlikely to be the same for each method. Thus it is suggested, however, that the dominant reason for the discrepancy is the difference in the loading

patterns experienced by the rupturing tissues in each configuration. As mentioned, in peel tests, rupture is predominantly mode 1, while in the present wedge-driven scenario mixed model separation occurs from the complex interaction between wedge and tissue. The corresponding G_c values can thus be expected to differ significantly.

5.5 Dissection model results and discussion

The deformed CZ-based model configuration partway through the analysis is shown in figure 5.9. The behaviour reflects the experimental observations where the tissue is stretched away from the wedge once it has separated from the other half. Additionally, figure 5.8 shows a close-up of the crack tip demonstrating the non-uniform mixed-mode fracture behaviour.

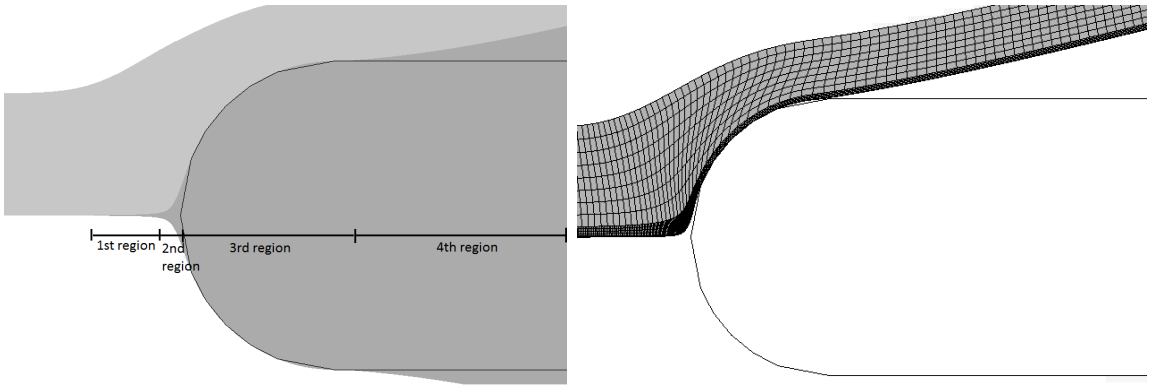

Figure 5.8: FE model from figure 5.9 zoomed in at crack tip with and without mesh. Left. The 4 stages of the crack progression are identified. The first region there is a more traditional crack opening. In the second region this is lost as the tissue begins to deform around the contact body. Next, the tissue contorts around the contact body (region 3) and finally separates from the contact body (region 4). Right. The visible mesh of the model to demonstrate the deformation. Individual elements close to the wedge are too fine to be seen. For similar regions the mesh is clearer if the CZ elements are not shown.

The experimental results are compared with the results of the numerical model for the calculated value of G_c^1 and G_c^2 (table 5.1) in figure 5.10. It can be seen that there is a good agreement between the experimental and numerical data. This lends confidence to the proposed approach for finding G_c and in the possibility of extending the approach to other types of damage by an external body, such as needle penetration or cutting with a sharper object such as a scalpel. Additionally, the result was verified by calculating G_c^1, according to 5.7, from the associated CZ model result. There was good association between the calculated numerical and experimental W_{ext}, $W_{elastic}^1$, and G_c^1, lending further confidence to the proposed approach.

However, care must be taken when selecting δ_c for problems in which a contact body acts on the cohesive zone elements. For this study $\delta_c = 2.5/6$ mm (where 2.5 mm is the wedge thickness), this is because at $\delta = 6\delta_c$ the cohesive zone has

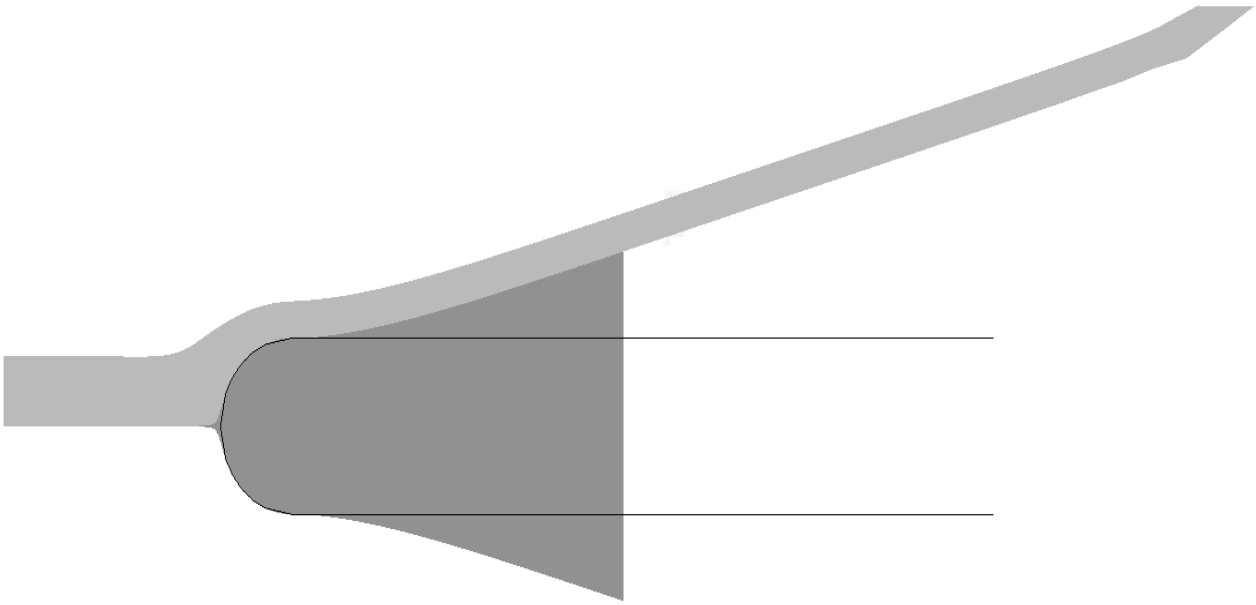

Figure 5.9: FE model midway through the analysis. The middle black area is the region occupied by CZ elements, which have been separated by the action of the wedge.

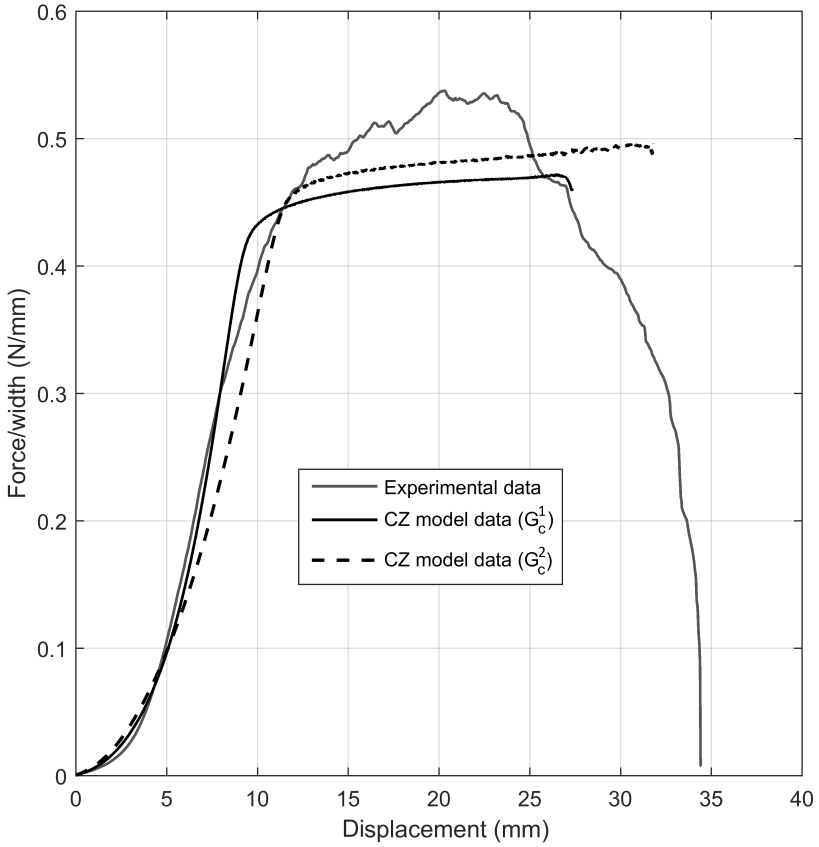

Figure 5.10: Force displacement plot of the average experimental data with force displacement response of the cohesive zone model for G_c^1 and G_c^2 in table 5.1

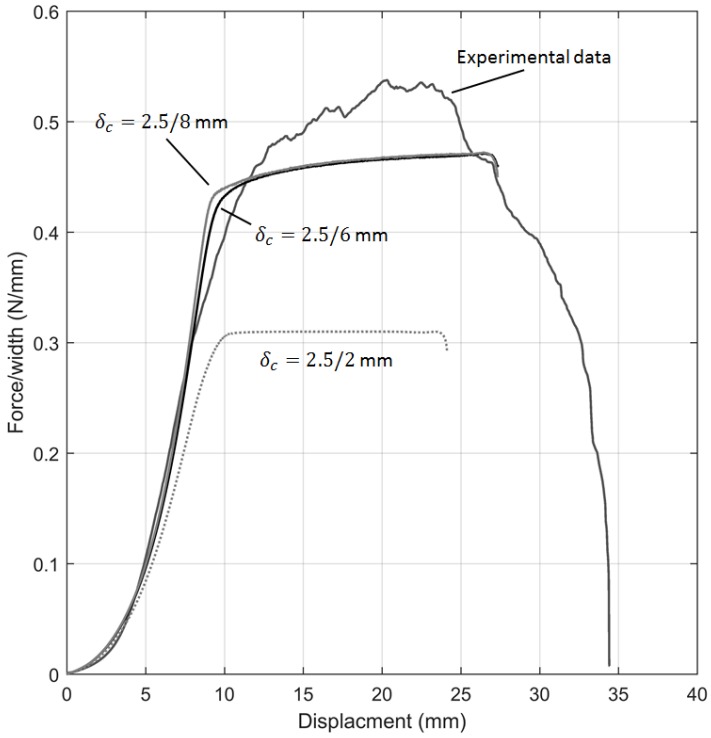

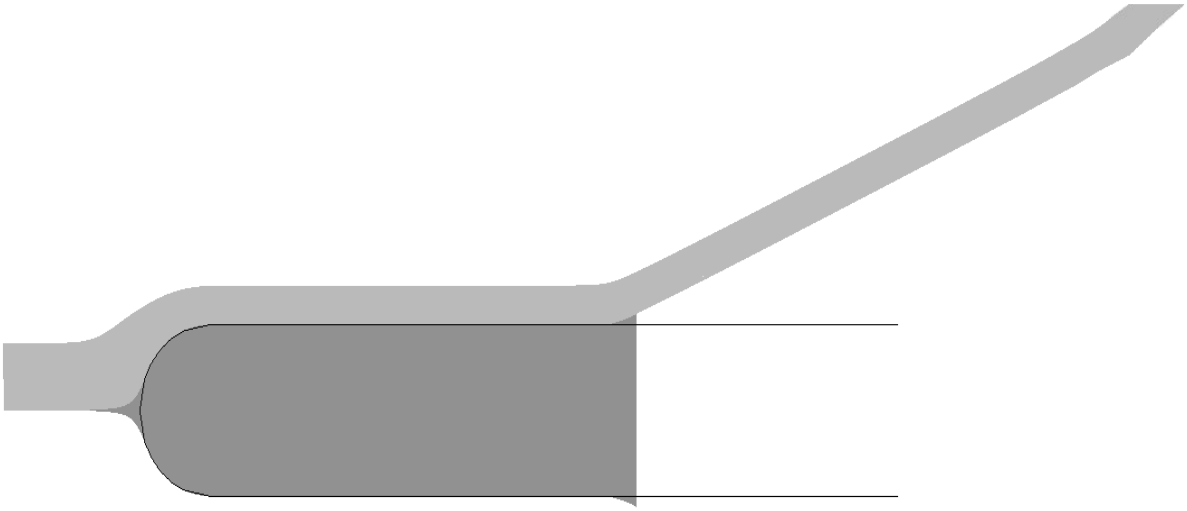

Figure 5.11: Illustration of the effect of δ_c on the force/width vs displacement behaviour of the cohesive zone models for G_c^1. Top: force/width vs displacement for $\delta_c = 2.5/6$ mm, $\delta_c = 2.5/8$ mm and $\delta_c = 2.5/2$ mm alongside the average experimental data. Bottom: finite element cohesive model with $\delta_c = 2.5/2$ mm. The cohesive zone elements (dark grey) hug around the contact body due to the remaining traction.

damaged to the extent that t can be considered effectively zero. In figure 5.11 it can be seen that $\delta_c = 2.5/8$ mm has little effect on the force displacement response. However, if the contact body thickness is less than $6\delta_c$ then the estimated plateau force would decrease despite the fact that G_c is unchanged (figure 5.11). The reason is that in this scenario, the wedge contact body is able to penetrate cohesive zone elements without opening them to their full damage level (i.e. without completely separating the two tissue halves). The resulting model configuration is shown in

figure 5.11. The energy associated with this penetration is correspondingly less than would be expected for a given value of G_c, and the estimated reaction force during fracture is lower. A possible solution is to modify the approach of Pagani et al [151]. Therein, directional cohesive zone elements are deployed with an additional string element between the corresponding crack surfaces, representing bridging fibres. A node midway along this string element, at the contact point with the contact body, ensures the contact body cannot penetrate the cohesive element unopposed.

5.6 Conclusions

The aim of this study was to assess the validity of CZ elements for modelling rupture of soft tissues driven by stiff external bodies. This was motivated by the need to model processes of catheter-induced dissection of the aortic wall, a previously little studied complication of catheter cardiovascular intervention.

An experimental set-up was developed in which an aluminium wedge of 2.5 mm thickness was displaced between an initially dissected aortic wall to dissect the remaining tissue, while the force displacement response was recorded. The results of this experiment showed qualitative similarities to results from controlled peel testing, though with greater variability between samples and a less distinct plateau region during dissection propagation.

Upper and lower values for the critical energy release rate (G_c^1 and G_c^2) were then calculated using a novel experimental-computational approach utilising the FE method with the optimisation toolbox within MATLAB. G_c values so derived were found to be 3-4 times greater than those obtained from peel test experiments on similar test specimens in chapter 3. It can be speculated that this is mostly a consequence of differences in material resistance to fracture (as quantified by G_c, in this case) in the different fracture modes present in each test configuration.

G_c was used in a cohesive zone FE model of the experimental procedure. It was found that the model-computed force displacement response corresponded well with the experimental data, giving confidence in the use of CZ elements for modelling cutting and perforation of soft tissues. However, care must be taken when selecting the critical opening/traction (δ_c/t_c) to ensure the energy of the CZ elements is expended in a physically consistent way.

Finally, further understanding of the problems encountered in chapter 4 can be achieved through extending the cohesive FE model from section 5.3 to a full three dimensional model allowing closer comparison.

Chapter 6

Conclusions

6.1 Outcomes

This thesis has focussed on the implementation and evaluation of means for characterising blood vessel damage. This was pursued in the context of two specific objectives: providing a means of creating a diseased tissue model from healthy porcine aorta; and evaluating means for numerical modelling of catheter induced dissection. These objectives were achieved through the use of finite element methods, and new and existing mechanical testing methods. The corresponding outcomes are now listed and evaluated with respect to existing work:

A means of altering arterial wall elastic and failure properties through enzyme and chemical treatment assessed via uniaxial testing (chapter 2) and controlled peel testing (chapter 3)

In this work enzyme and chemical treatments were used to alter the mechanical response of healthy porcine aorta with the aim to emulate diseased tissue mechanical properties. Previous studies had employed similar methods and utilised various mechanical testing procedures to evaluate the associated changes. Uniaxial tensile testing has been performed following elastase and collagenase treatment to investigate whether collagen is solely responsible for the softening behaviour of arterial walls [39]. They found that removing collagen removed the softening behaviour of tissue whilst removing elastin resulted in continuous softening behaviour. Additionally, [40] evaluated the uniaxial mechanical response of the elastin or collagen fibres in isolation from one another by applying the same enzyme treatments to aortic wall. They observed that completely removing collagen resulted in a linear mechanical response that like before had no softening behaviour. While removal of all elastin resulted in a non-linear anisotropic response that again showed continuous softening.

Biaxial testing has also been utilised to evaluate the changes in mechanical response. Chow et al. investigated the changes in mechanical behaviour of arterial wall following progressive elastase treatment [41]. Distinct mechanical responses were identified for each level of tissue degradation with tissue initially becoming more compliant but then stiffening until full elastin loss where tissue is far stiffer than the controls. Gundiah et al. also performed biaxial testing but following elastase and collagenase treatment at two different levels of degradation [42]. Collagenase treated samples showed a decreased non-linearity compared to controls whereas elastin treatment resulted in significantly stiffer tissue response.

Finally pressure-inflation testing had also been performed following enzyme treatment. Kochova et al. applied collagenase and elastase treatments and found that the former altered the stiffness of the arterial wall and while the latter altered the wall geometry it did not effect the mechanical response [43]. In another study elastase treatment resulted in the tissue being more ductile at low strains and stiffer at high strains [44].

Compared to these works the key novelty in chapter 2 was testing samples to the point of failure following enzyme treatment. Only one previous study had tested tissue to failure and only after collagenase treatment [45]. They found that tissue tensile strength was reduced following collagenase treatment, similar to this study. However, no previous work has shown the apparent strengthening behaviour seen following elastase treatment in chapter 2. The results of Chow et al. show similar increases in extensibility but did not test beyond physiological stretches. Additionally, in this work tissue cross-linking was also considered via glutaraldehyde treatment. This produced no significant effect on the failure properties despite clear changes in appearance and handling properties.

Controlled peel testing was performed to investigate the effect of the enzyme and chemical treatments on the arterial dissection behaviour. While the dissection behaviour had been investigated by both peel testing and liquid infusion tests [46, 47, 48, 49], no work has investigated the effect of removing and cross-linking constituent proteins on the dissection response. Comparing G_c between treated and control tissue in chapter 3, it can be seen that applying collagenase solution to porcine thoracic aorta made the tissue less resistant to peeling in both axial and circumferential directions. However, anisotropy in the critical energy release rate was increased compared to control samples. Elastase treatment had a negligible effect on the tissue response to controlled peel testing. From these it may be inferred that collagen plays a more important role in resisting this loading mechanism. Glutaraldehyde treatment increased resistance to peeling in both directions, but more so in the circumferential direction. Anisotropy in the response was correspondingly reduced. Thus, cross-linking accompanying this treatment appears to impart greater resistance to peeling in circumferential direction.

Therefore it can seen that these treatments alter the wall elastic and failure properties. However the extent to which this occurs is influenced by not only the loading type but loading direction also.

Further understanding of the contribution of constituent proteins to artery wall response under loading both in the elastic and damage regimes (chapters 2 and 3).

The arterial wall mechanical response is derived from the elastin and collagen mechanical properties and the associated interplay between these protein fibre bundles. It is generally accepted that in the two stage mechanical response seen in many soft tissues, the initial compliance at low strain is a result of the elastin stretching [10]. The collagen fibres are initially crimped and unfurl as the tissue is stretched until the collagen fibres are straightened. The tissue stiffening at high strains is then a result of the stiffer collagen fibres bearing the load. However the nature of this interplay and how it is effected by disease is not yet clear.

Ageing has been shown to cause a loss of medial elastin followed by an increase in the stiffer collagen fibres, further stiffened by additional cross-linking, to compensate [28, 29, 30, 31]. This results in the elastin-collagen interaction altering and the stiffer collagen fibres being recruited at smaller deformations, leading to an observed stiffening of the arterial wall. Whilst in aneurysm formation, the characteristic ballooning is also widely attributed to loss of elastin and a resulting loss of stiffness in the artery [32, 33]. In atherosclerosis, changes in elastin and collagen structure again weaken the medial and intimal layers [34, 35, 36]. Genetic diseases such as Marfan syndrome can also have large effects on collagen and elastin fibres leading to greatly reduced stiffness and toughness in blood vessel walls [37]. These changes are often complex and multifaceted. Correspondingly, alterations such as the loss of elastin may increase or decrease stiffness depending on a variety of co-factors.

Collagen and elastin have been removed completely from the arterial wall in [40] by enzyme treatment and it was found that completely removing collagen resulted in a linear mechanical response that had no softening behaviour. While removal of all elastin resulted in a non-linear anisotropic response that again showed continuous softening. In addition, partial removal of elastin leads to elastomer-like behaviour in [41] while full elastin removal showed increased stiffness compared to controls.

In this work the results from uniaxial tensile testing of elastase treated samples appear to show that elastin removal initiates some form of compensatory mechanism within the arterial wall such that it ruptures at higher strains despite the loading profile being the same as control samples. How this is reflected in the collagen-elastin interplay requires investigation. Additionally, the peel test results imply that collagen radial bridges between lamellae play a more important role in preventing arterial dissection. Collagenase treated samples had significantly lower G_c than controls while elastase treatment samples showed no change. Finally, cross-linking from glutaraldehyde treatment has a more significant effect on peeling response than uniaxial tensile response. This implies that the cross-links formed in the axial and circumferential directions were not significant to alter wall mechanical properties in these directions. However, in the the inter-lamellae space where there are only small fibre bridges present, these additional cross-links may play a more important role.

Insights into arterial wall dissection response. Specifically, for controlled peeling of artery samples with constituent proteins removed (chapter 3) or when an external body drives the dissection (presented in chapter 5).

Arterial dissection is most commonly investigated *ex vivo* by liquid infusion tests such as those performed in [47] or controlled peel testing first performed in [46]. Controlled peel tests clearly represent a simplification of *in vivo* loading regimes, and it could be argued that liquid infusion experiments more closely resemble blood flow-driven dissection, at least. However, in the latter configuration, while the

separation of vessel layers would remain predominantly mode 1, there is likely an ambiguous mixture of rupture modes involved in any particular experiment. It is correspondingly difficult to extract meaningful and repeatable measures of tissue strength by this means. Peeling, by contrast, involves pure mode 1 rupture, and the physical meaning of the derived energy release rate G_c is correspondingly clear. The rupture process, being driven by displacements of opposing tissue flaps, is also easier to control, further improving repeatability. Therefore, as a means of quantifying resistance to dissection (i.e. separation of tissue layers), and of reliably assessing the effect on this of the different treatments, peeling tests were adopted in this work.

Comparing G_c from chapter 3 with the previous studies, it can be seen that it is on the whole far larger in this study. This is likely because testing in this study was performed at room temperature in open air and at a far higher testing speed than the previous peel tests. The latter in particular has been shown to increase G_c by approximately 30%. As mentioned in a previous paragraph, collagenase treated samples have a significantly lower calculated G_c than control samples while elastase treated samples showed no significant differences. Controlled peel testing of aneurysm tissue in [58] showed that aneurysm tissue dissected more easily than healthy tissue which is most like that of the collagenase digested tissue reported here. However, aneurysms are more strongly associated with elastin loss, which was found in chapter 3 to have negligible effect on controlled peel testing of arterial samples.

The calculated G_c in chapter 5 is approximately four times greater than in chapter 3. One reason for this difference is that frictional energy dissipation was assumed negligible in the wedge tests, whereas its contribution to W_{ext} cannot be zero in practice. However, a previous study [143] has identified a friction coefficient of 0.046 between steel and artery wall, thus it is unlikely that this contribution alone cannot fully account for the greater G_c in the wedge configuration. Moreover, the tissue was well hydrated throughout the experiments and no obvious friction-associated behaviours were observed. Additionally in chapter 3, $W_{elastic}$ was calculated by assuming a linear constitutive response (based on the presentation in [46]), while here the material behaviour was captured using a more realistic hyperelastic constitutive model. Thus, the $W_{elastic}$ contribution is unlikely to be the same for each method. However, it is likely that the dominant reason for the discrepancy is the difference in the loading patterns experienced by the rupturing tissues in each configuration. This follows from the consideration that the (highly heterogeneous) tissue's overall fracture behaviour will be governed by the microstructural arrangement and tissue's overall fracture behaviour will be governed by the microstructural arrangement and behaviour of its constituents (collagen/elastin fibres, ground substance, etc.). The latter may include both inherent constituent fracture energies and dissipative processes active within the so-called process zone of the fracture. If these phenomena were modelled explicitly ([152], in the context of metal-elastomer separation), different

specimen loading regimes (as between peel tests and the current wedge configuration) would naturally lead to different overall fracture behaviour, since the corresponding constituent-level loads would similarly differ. In the adopted CZ approach, these microscale processes are effectively ignored, considering the tissue macroscopically and with fracture behaviour governed by a single fracture energy parameter Gc. Gc, in other words, lumps the effects of the microscale processes. Correspondingly, different loading configurations can be expected to manifest as different values for Gc in such a formulation, as observed here.

Identification of possible mechanisms during the propagation of a CID, a previously poorly understood complication, through a new experimental method and finite element analysis. This can be seen in chapters 4 and 5.

Catheter induced dissections (CIDs) are a rare but commonly fatal complication of intravascular catheterisation. Data on CID occurrence is sparse, however, major complications such as coronary artery dissection that extends to the aortic root has been reported to occur in 9 out of 43143 cardiac catheterisations (approximately 0.02%) [50]. However, this increased to 0.2% if patients were undergoing treatment for myocardial infarction. Another study [51] found the same type of dissection in 15 of 12031 percutaneous coronary intervention (PCI) procedures (approximately 0.12%). Data for this type of dissection are most prevalent because of its high mortality rate, however for coronary artery dissection alone, or CID of other arteries, data are sparser. In addition, it is difficult to provide context for these figures in terms of total complications, as CID are often included as part of other categories such as vascular trauma [52]. However, in [53] the overall complication rate for PCI was estimated at 2.7% for the period 2003-2006, from which it may be loosely inferred that coronary CID extending to the aortic root occurs in 5% of PCI procedures. Furthermore, the mortality rate is relatively high: 67% of deaths from coronary catheterisation procedures reported in [54] were from CID of the coronary arteries, while [55] reported that 25% of aortic CIDs that require surgical intervention lead to death of the patient.

Unfortunately it is difficult to ascertain how CIDs are initiated or propagated. This is because, commonly, catheterisation procedures are observed via three dimensional rotational angiography, and the dissection can only be detected by its effect on the blood flow. Thus, visualising the blood vessel wall and the damage to it is very difficult. Furthermore, the spatial resolution of such imaging modalities is relatively low, meaning it is difficult to identify the dissection until its effect on the blood flow is pronounced. As a result there is little information in the literature on mechanisms by which CIDs in arteries are initiated or propagated. Therefore, means by which a CID is propagated can only be speculated. In chapter 4 a scenario was

postulated in which the dissection has been initiated (the means by which were left for future investigations) and the catheter is positioned at the dissection front. The endovascular surgeon operating the catheter feels resistance to their attempts to guide the catheter to its destination as the catheter pushes against the dissection front. Assuming it is a bend in the vessel, they apply force to the catheter to propel it around this assumed bend. This inadvertently pushes the catheter into the created dissection front, driving the catheter between the layers of the media, and opening the dissection further. A corresponding experimental configuration was then devised to explore this scenario.

Arterial dissection by other mechanisms has been well investigated by both *ex vivo* testing in a laboratory, and simulations with the finite element (FE) method. The first *ex vivo* arterial wall dissection was performed via liquid infusion into the artery media [47, 49, 56]. This was aimed at replicating blood flow-driven propagation of the dissection. Later, controlled peeling of the media was employed to gain further understanding of the force displacement behaviour, and in particular its anisotropy [46, 48]. This methodology was then utilised on diseased arteries and aneurysms to assess disease-associated changes [57, 58].

FE-based computational models of these controlled peeling experiments have been proposed. In each case, a so-called cohesive zone (CZ) formulation has been used to model evolution of the tissue rupture, which enabled the effect of collagen fibre bridging during dissection to be emulated. Gasser et al. used a cohesive law within the extended FE method to simulate the controlled peeling (dissection) experiments of Sommer et al. [59, 46]. Later, an anisotropic cohesive law was applied by Ferrara and Pandolfi that accounted for the anisotropic behaviour seen in Sommer et al.'s peel tests [60]. However, no work has been performed to investigate arterial perforation or dissection by an external body either experimentally or computationally.

Experimental results in chapter 4 showed three distinct stages: deformation of the tissue prior to penetration; progressive rupture and penetration of the tissue; and complete through penetration of the specimen, so that only frictional forces, between catheter shaft and tissue, are acting. This is similar to the behaviour seen in [63] for needle insertion in bovine gelatine except that in that study there is a build up of force that is released once the gelatine is initially perforated. While in this work there is a smooth transition when perforation begins. Additionally, frictional forces contribute more to the total force in their study. However, like in [63] the damage was localised to the catheter dissection path. Although this may have been because of the pointed shape of the catheter and the idealised conditions that were present in chapter 4. It may be that *in vivo*, where the arterial wall is cylindrical, rather than flat, the path taken by the catheter and the resulting dissection are both broader. Additionally, the hole created by the catheter could be made larger by the blood entering the hole and pushing the tissue halves further apart.

In chapter 5 the experimental results show four stages. Deformation of tissue prior to damage; transition from elastic to damage regimes; a plateau region where damage is continually occurring; and separation as the tissue halves are completely separated. These identified features of the experimental curves are closer to that seen for controlled peel testing (chapter 3) than in the catheter dissections in chapter 4. It can therefore be speculated that this approach bears closer resemblance to peel testing than the catheter dissection tests. However, the profile of the plateau regions is significantly more erratic than those obtained from controlled peel testing and showed greater variation in magnitude between samples, like the catheter dissections in chapter 4. This is a key difference between dissection during controlled peeling and contact driven dissection. The individual fibre bridges may undergo different fracture behaviour under different loading mechanisms. A possible mechanism by which this may occur is that in controlled peeling the same amount of fibres break per 1 mm^2 of tissue dissected (assuming the same fibre bridge density across the tissue) and a relative smooth force displacement profile is recorded. However when an external body drives the dissection, the fibre bridges have to deform around this body. This may lead to fibre bridges breaking less uniformly and a more jerky force displacement profile.

An experimental-computational approach for calculating the fracture energy during perforation of soft tissues. This was proposed in chapter 5.

In chapter 5 dissection of arterial layers driven by an external body, i.e. a catheter, was of interest. Comparable configurations exist during, for example, needle insertion and cutting, and the CZ approach has been used by various authors to model these processes. Needle insertion into muscle tissue has been investigated with parameters extracted from experimental data [61], however, no validation against experimental results was presented in turn. This was partially addressed by Forsell and Gasser when modelling cardiac tissue penetration and failure as a result of perforation by a pacemaker wire [62]. However, it was not clear how the governing critical energy release rate (G_c) was calculated from the experimental data, making it difficult to assess the fidelity of their FE model with respect to the latter. Finally, Oldfield et al. utilised an experimental-computational approach to estimate G_c during needle insertion into a gelatine soft tissue phantom [63]. This approach yielded good agreement between experimental and computational force-displacement profiles at four different insertion rates and was more comprehensive than the previous studies mentioned. However, gelatine is a homogeneous isotropic material that does not exhibit the stochastic breaking of fibres/fibrils seen in perforation and damage of most soft tissues [64], and so it is still unclear how well the CZ formalism carries over to real soft tissues in this context.

The methods from [46] for calculating G_c for experimental data from controlled peel testing were applied to experimental data of dissection driven by an external body in chapter 5. G_c calculated from this approach had been previously applied in a FE CZ model of arterial dissection and showed a good correspondence [59]. By utilising FE models that emulated conditions at certain points of the experiment and the MATLAB optimisation toolbox, G_c was estimated from the experimental data. Furthermore, when placed in an FE model, it was found that the experimental data lay within the model-computed force displacement responses, giving confidence in the approach. Additionally, the result was verified by calculating G_c, from the associated CZ model result. Good agreement between predicted and experimental W_{ext}, $W_{elastic}$, and G_c values was again observed, lending further confidence to the approach.

Limitations in the application of cohesive zone models when a contact body drives the crack propagation. These were identified in chapter 5.

As mentioned previously, CZ models have been used to mimic both arterial dissection and soft tissue perforation [59, 60, 62, 61]. However, in [63] it was identified that when modelling needle penetration of gelatine with CZ elements, the needle penetrated "intact" CZ elements leading to a physically intangible situation. They identified that this penetration was particularly sensitive to δ_c, the CZ critical opening, and that penetration by the probe can be minimised by reducing δ_c but at the expense of numerical stability. In chapter 5, it was found that for the scenario investigated, a value of $\delta_c = 2.5/6$ mm (i.e. 1/6 of the 2.5 mm wedge thickness) was sufficient to damage the CZ elements to the extent that t, the traction, was effectively zero. Further reducing δ_c (while maintaining G_c) had little effect on the force-displacement response, as demonstrated by the result of using $\delta_c = 2.5/8$ mm. However, if δ_c was enlarged such that the contact body thickness was $< 6\delta_c$, the predicted plateau force noticeably decreases, despite use of the same G_c value. The reason is that in this scenario, the wedge contact body was able to penetrate CZ elements without opening them to their full damage level (i.e. without completely separating the two tissue halves). For the model in chapter 5, this resulted in the continuum elements hugging around the contact body as a result of the relatively high remaining traction within the CZ elements. The energy associated with this penetration was correspondingly less than would be expected for a given value of G_c, and the estimated reaction force during fracture was lower. Clearly, this penetration of "un-ruptured" elements was non-physical. A possible solution is to adopt the approach of Pagani et al [151]. Therein, directional CZ elements are deployed with an additional string element between the corresponding crack surfaces, representing bridging fibres. A node midway along this string element, at the contact point with the contact body, ensures the contact body cannot penetrate the CZ element unopposed.

6.2 Limitations and future work

Experimental and computational analyses are essential tools in the improvement of endovascular device technologies. While computational approaches are being used more frequently, experimental approaches are still necessary to define the problem, validate the models, or to form part of combined approaches such as in chapter 5. For all approaches, increased knowledge of arterial wall mechanics in elastic and failure regimes is required to allow underlying mechanisms to be identified and to more closely mimic in vivo conditions. This work has provided greater understanding of arterial failure both computationally and experimentally, however further work is required to translate these developments into impact on medical device design.

As mentioned in the Introduction, disease processes are complex and multifaceted, and simple enzymatic digestion provides only an approximation of the various chemical, physical and cellular processes taking place within the arterial wall during, for example, aneurysm formation. Therein loss of elastin, and the accompanying increase in wall compliance, stimulates cellular mechanotransduction and, in turn, complex remodelling of collagen components [16]. Wall mechanics in atherosclerosis are yet more complex due to the presence of the athersclerotic plaque which, despite efforts to capture its mechanical properties, is exceedingly difficult to incorporate into healthy arteries *ex vivo* with many studies opting to induce the process *in vivo* [115, 116]. The physiological complexity of real disease processes notwithstanding, the aim of the work in chapters 2 and 3 was to produce a physical model of diseased arteries that effectively emulates the accompanying changes in their mechanical properties only. However, as mentioned in section 2.4.3, judicious combination of any or all of these treatments could in principle be used to effect the changes observed in a particular disease.

Further physiological relevance could have been achieved in chapter 2 with biaxial loading, which more closely reflects the *in vivo* loading conditions [110, 8, 111]. However, there are practical difficulties associated with using biaxial testing at high loads present in this study [94], and doing so may yield poor estimates of stress [112, 113]. Thus it is ill-suited to investigation of failure behaviour.

The GOH constitutive model was chosen due to its wide use for capturing arterial wall mechanics. In chapter 2 only the media response (assumed to be dominant) was investigated; the adventitia was removed and the intima thickness was small enough to be considered negligible. Despite using this relatively thin layer of tissue, a gradient of enzyme penetration must persist, meaning superficial regions will be more digested than interior ones. A constitutive model that incorporates different layers may accordingly enable the depth-dependence of mechanical properties that must accompany this gradient to be captured.

Additionally, while the GOH formulation has been shown to model well the tissue response in physiological strain ranges, the exponential fibre term may not be suitable

outside this range, where it appears the collagen fibres transition from exponential to more linear behaviour [114]. A modified strain energy function that emulates the GOH response for moderate strains, but approaches linearity nearer to failure strains may thus be more widely applicable. Finally the applicability of the GOH model to arterial wall that has undergone enzymatic digestion has not been established; enzyme treatment may drastically alter fibre properties such that the underlying assumptions of the model may no longer be valid; and further investigation of this matter is required.

In chapter 3 it was assumed that the effect of smooth muscle cell bridges, between the lamellae, on the tissue response to controlled peeling was small, compared with those of collagen and elastin. Nevertheless it has been shown that smooth muscle cells do play a role in arterial dissection *in vivo* [134, 135]. A dedicated investigation into the effect of removing smooth muscle cell contribution (for example by means described in [136]) in controlled peeling conditions would help to clarify their role.

In chapters 2 and 3 to ensure complete removal of the adventitia an incision was made midway through the arterial through-thickness. This involved removing more tissue than was likely necessary and removal of the adventitia could not be certain. This may have effected the variation in mechanical properties between samples as more adventitia may be remaining on some samples than others where it was completely removed. Imaging techniques such as histology would aid in verifying whether this technique did indeed fully remove the adventitia and should be utilised in future studies [94].

The loading rate in chapter 3 applied to the samples is greater than that applied in previous studies. Tong et al. investigated the effect of peeling rate on the tissue response [57]. They found approximately 30% difference in F between samples tested at 1 mm/min and 1 mm/s, a significantly smaller difference than between the findings here and results from other studies. This suggests speed alone does not account for the discrepancy, and variation between samples may play a greater role. Additionally, it is likely that different loading speeds will effect the gradient of the elastic regions of the curves and the magnitude of the plateau region in chapter 5. The numerical results should therefore be understood to represent the behaviour at 1 mm/s. However, there is no apparent reason to expect that such rate-sensitivity would qualitatively change the results, only the involved magnitudes. Finally, the loading speeds and environmental conditions (tissue hydration, for example) were very similar to the experiments in chapters 3 and 5, and therefore there is confidence in at least excluding viscous effects as the reason for the differences in G_c values.

In previous studies, mechanical testing of arterial walls have been performed within a saline bath, whilst in these studies testing was conducted at room temperature and in open air. For uniaxial tensile testing in chapter 2, it was explained that this was to allow for accurate recording of sample stretch. But methods similar to those

employed by Loree et al. with a saline drip at 37°C may yield results with more physiological relevance [109]. This approach could also be applied to controlled peel testing (chapter 3) and the CID investigations (chapters 4 and 5). However, since all tests were performed under the same conditions the internal comparisons made in this work are still valid.

Mechanical tests, by themselves, do not allow changes in the arterial wall microstructure to be observed directly, even if some overall changes may be inferred from their results. In chapter 3 example images were acquired with multiphoton microscopy, and in the axial-circumferential plane, to enable qualitative assessment of structural changes. But, more detailed and systematic visual analysis using these modalities [137], or perhaps histology [48] or electron microscopy [131], would enable microstructural changes to be assessed conclusively. This may elucidate the link between elastin/collagen radial fibre bridging and gross mechanical properties for the disease emulation work, and provide further information on the underlying mechanisms in CID.

In chapters 3, 4 and 5, where dissection of the vessel wall was performed, the samples were tested as flat rectangular pieces, while *in vivo*, the vessel is tubular and held in a pre-stressed state that is partially released by cutting the vessel open to lay it flat. The effect of this difference on the dissection propagation and on measured values such as the F and G_c are unknown, as previous work, either peel testing or liquid infusion testing, also involved flat samples. If dissection behaviour of the artery wall could be investigated in its *in vivo* condition, the effect of flattening the tissue could be clarified.

While the propagation of CIDs was investigated in chapters 4 and 5, the mechanisms by which it is initiated are still unknown. This may be a result of the guide-wire initiating the dissection and the catheter following to exacerbate damage or contact of the catheter tip with the vessel wall causing the wall to be cut away and detached. Furthermore the controlled conditions in this work only partially reflect the complexity present *in vivo*, and removes the effects of blood flow, disease-associated tissue degradation, surrounding tissues, and the differing response of a tube compared to flattened tissue.

Achieving convergence of finite element models with large deformations and high residual forces, such as in chapter 4, is challenging. Refining the mesh further to densities similar to 5 may improve convergence but at the cost of increasing computational time. Remeshing algorithms could also be used to refine the mesh where needed but again this requires more computations. An alternative approach is to utilise explicit methods as, compared to implicit methods, explicit methods handle non-linearities, such as contact, with relative ease. Additionally, smoothed finite element methods may help to ameliorate such numerical difficulties as these formulations allow for greater element distortion without convergence problems

[153]. The extended finite element method may also be used to model dissection propagation in place of cohesive zone elements. By enriching shape functions, strong discontinuities can be modelled and traction separation laws can be used to govern crack behaviour. This approach may reduce convergence issues and can also be configured so that the dissection does not have to propagate along a predetermined path. Alternatively, advances in cohesive zone elements like those proposed by Pagani and Perego, would allow the perforation to be modelled with greater accuracy [151]. Therein, directional cohesive zone elements are deployed with an additional string element between the corresponding crack surfaces, representing bridging fibres. A node midway along this string element, at the contact point with the contact body, ensures the contact body cannot penetrate the cohesive element unopposed.

Before utilising the model presented in chapter 4 in medical device design, model convergence and close association between numerical and experimental data must be achieved. Following this the robustness of the model must be investigated including altering material and fracture properties, catheter geometries, and tissue geometry. Finally, the proposed scenario can be extended to be more similar to *in vivo* conditions providing greater confidence in the observations on catheter design drawn from the model.

References

[1] M. R. Villarreal, Arterial System (2009).
URL https://commons.wikimedia.org/wiki/File:Arterial_System_en.svg

[2] Medical gallery of Blausen Medical (2014). doi:10.15347/wjm/2014.010.

[3] MSC Software Corporation, MARC 2014 Volume A: Theory and User Information (2014).

[4] Student, The Probable Error of a Mean, Biometrika (1908) 1–25.

[5] GBD 2013 Mortality and Causes of Death Collaborators, Global, regional, and national age-sex specific all-cause and cause-specific mortality for 240 causes of death, 1990-2013: A systematic analysis for the Global Burden of Disease Study 2013, The Lancet 385 (9963) (2015) 117–171. doi:10.1016/S0140-6736(14)61682-2.

[6] S. Allender, P. Scarborough, V. Peto, M. Rayner, J. Leal, R. Luengo-Fernandez, A. Gray, European cardiovascular disease statistics, European Heart Network.
URL http://hdl.handle.net/10536/DRO/DU:30020501

[7] P. A. Heidenreich, J. G. Trogdon, O. A. Khavjou, J. Butler, K. Dracup, M. D. Ezekowitz, E. A. Finkelstein, Y. Hong, S. C. Johnston, A. Khera, D. M. Lloyd-Jones, S. A. Nelson, G. Nichol, D. Orenstein, P. W. F. Wilson, Y. J. Woo, Forecasting the future of cardiovascular disease in the United States: A policy statement from the American Heart Association, Circulation 123 (8) (2011) 933–944. doi:10.1161/CIR.0b013e31820a55f5.

[8] J. D. Humphrey, Cardiovascular Solid Mechanics: Cells, Tissues, and Organs, Springer-Verlag, Berlin, 2002.

[9] S. Glagov, R. Vito, D. P. Giddens, C. K. Zarins, Micro-architecture and composition of artery walls: relationship to location, diameter and the distribution of mechanical stress., Journal of Hypertension. 10 (6) (1992) 101–4. doi:10.1097/00004872-199208001-00026.

[10] D. P. Sokolis, E. M. Kefaloyannis, M. Kouloukoussa, E. Marinos, H. Boudoulas, P. E. Karayannacos, A structural basis for the aortic stress–strain relation in uniaxial tension, Journal of Biomechanics 39 (9) (2006) 1651–1662. doi:10.1016/j.jbiomech.2005.05.003.

[11] T. Boulesteix, A.-M. Pena, N. Pagès, G. Godeau, M.-P. Sauviat, E. Beaurepaire, M.-C. Schanne-Klein, Micrometer scale Ex Vivo multiphoton imaging of unstained arterial wall structure, Cytometry Part A 69A (1) (2006) 20–26. doi:10.1002/cyto.a.20196.

[12] S. S. Martin, M. J. Blaha, R. Blankstein, A. Agatston, J. J. Rivera, S. S. Virani, P. Ouyang, S. R. Jones, R. S. Blumenthal, M. J. Budoff, K. Nasir, Dyslipidemia, coronary artery calcium, and incident atherosclerotic cardiovascular disease: Implications for statin therapy from the multi-ethnic study of atherosclerosis, Circulation 129 (1) (2014) 77–86. doi:10.1161/CIRCULATIONAHA.113.003625.

[13] M. Aikawa, P. Libby, The vulnerable atherosclerotic plaque: Pathogenesis and therapeutic approach, Cardiovascular Pathology 13 (3) (2004) 125–138. doi:10.1016/S1054-8807(04)00004-3.

[14] M. H. M. Vlak, A. Algra, R. Brandenburg, G. J. E. Rinkel, Prevalence of unruptured intracranial aneurysms, with emphasis on sex, age, comorbidity, country, and time period: A systematic review and meta-analysis, The Lancet Neurology 10 (7) (2011) 626–636. doi:10.1016/S1474-4422(11)70109-0.

[15] M. J. H. Wermer, I. C. Van Der Schaaf, A. Algra, G. J. E. Rinkel, Risk of rupture of unruptured intracranial aneurysms in relation to patient and aneurysm characteristics: An updated meta-analysis, Stroke 38 (4) (2007) 1404–1410. doi:10.1161/01.STR.0000260955.51401.cd.

[16] J. C. Lasheras, The Biomechanics of Arterial Aneurysms, Annual Review of Fluid Mechanics 39 (1) (2007) 293–319. doi:10.1146/annurev.fluid.39.050905.110128.

[17] M. T. Bhatti, K. R. Peters, C. Firment, R. A. Mericle, Delayed exacerbation of third nerve palsy due to aneurysmal regrowth after endovascular coil embolization, Journal of Neuro-Ophthalmology 24 (1) (2004) 3–10. doi:10.1097/00041327-200403000-00002.

[18] W. S. Weintraub, E. M. Mahoney, Z. Zhang, H. Chu, J. Hutton, M. Buxton, J. Booth, F. Nugara, R. H. Stables, P. Dooley, J. Collinson, M. Stuteville, N. Delahunty, A. Wright, M. D. Flather, E. De Cock, One year comparison of costs of coronary surgery versus percutaneous coronary intervention in the stent or surgery trial., Heart (British Cardiac Society) 90 (7) (2004) 782–8. doi:10.1136/hrt.2003.015057.

[19] J. R. Langabeer, T. D. Henry, D. J. Kereiakes, J. Dellifraine, J. Emert, Z. Wang, L. Stuart, R. King, W. Segrest, P. Moyer, J. G. Jollis, Growth in percutaneous coronary intervention capacity relative to population and disease prevalence., Journal of the American Heart Association 2 (6) (2013) e000370. doi:10.1161/JAHA.113.000370.

[20] S. Reitsma, D. W. Slaaf, H. Vink, M. A. M. J. van Zandvoort, M. G. A. oude Egbrink, The endothelial glycocalyx: composition, functions, and visualization., Pflügers Archiv European Journal of Physiology 454 (3) (2007) 345–59. doi:10.1007/s00424-007-0212-8.

[21] D.-A. Jia, Y.-J. Zhou, D.-M. Shi, Y.-Y. Liu, J.-L. Wang, X.-L. Liu, Z.-J. Wang, S.-W. Yang, H.-L. Ge, B. Hu, Z.-X. Yan, Y. Chen, F. Gao, Incidence and predictors of radial artery spasm during transradial coronary angiography and intervention., Chinese Medical Journal 123 (7) (2010) 843–7.

[22] M. A. Mamas, A. Alonso, L. Neyses, Extensive catheter-induced aortic dissection., The Canadian Journal of Cardiology 24 (2) (2008) 9–10.

[23] A. Srivastava, M. Bradley, M. Kelly, Bilateral Carotid Artery Dissection after High Impact Road Traffic Accident, Journal of Radiology Case Reports 2 (5) (2008) 23–28. doi:10.3941/jrcr.v2i5.37.

[24] H. Wolinsky, S. Glagov, A Lamellar Unit of Aortic Medial Structure and Function in Mammals, Circulation Research 20 (1) (1967) 99–111. doi:10.1161/01.RES.20.1.99.

[25] J. M. Clark, S. Glagov, Transmural organization of the arterial media. The lamellar unit revisited., Arteriosclerosis 5 (1) (1985) 19–34. doi:10.1161/01.ATV.5.1.19.

[26] A. Schriefl, G. Zeindlinger, D. M. Pierce, P. Regitnig, G. A. Holzapfel, Determination of the layer-specific distributed collagen fibre orientations in human thoracic and abdominal aortas and common iliac arteries, Journal of The Royal Society Interface 9 (71) (2012) 1275–1286. doi:10.1098/rsif.2011.0727.

[27] N. F. MacLean, N. L. Dudek, M. R. Roach, The role of radial elastic properties in the development of aortic dissections., Journal of Vascular Surgery 29 (4) (1999) 703–10. doi:10.1016/S0741-5214(99)70317-4.

[28] D. M. Basalyga, D. T. Simionescu, W. Xiong, B. T. Baxter, B. C. Starcher, N. R. Vyavahare, Elastin degradation and calcification in an abdominal aorta injury model: role of matrix metalloproteinases., Circulation 110 (22) (2004) 3480–7. doi:10.1161/01.CIR.0000148367.08413.E9.

[29] S. E. Greenwald, Ageing of the conduit arteries., The Journal of Pathology 211 (2) (2007) 157–72. doi:10.1002/path.2101.

[30] A. Y. Lee, B. Han, S. D. Lamm, C. A. Fierro, H.-C. Han, Effects of elastin degradation and surrounding matrix support on artery stability., American Journal of Physiology. Heart and Circulatory Physiology 302 (4) (2012) 873–84. doi:10.1152/ajpheart.00463.2011.

[31] M. J. Sherratt, Tissue elasticity and the ageing elastic fibre., Age 31 (4) (2009) 305–25. doi:10.1007/s11357-009-9103-6.

[32] A. Daugherty, L. a. Cassis, Mouse models of abdominal aortic aneurysms., Arteriosclerosis, Thrombosis, and Vascular Biology 24 (3) (2004) 429–34. doi:10.1161/01.ATV.0000118013.72016.ea.

[33] J. Ferruzzi, D. A. Vorp, J. D. Humphrey, On constitutive descriptors of the biaxial mechanical behaviour of human abdominal aorta and aneurysms., Journal of the Royal Society, Interface / the Royal Society 8 (56) (2011) 435–450. doi:10.1098/rsif.2010.0299.

[34] M. J. Barnes, Collagens in Atherosclerosis, Collagen and Related Research 5 (1) (1985) 65–97. doi:10.1016/S0174-173X(85)80048-0.

[35] B. J. Whipp, H. B. Rossiter, S. A. Ward, Exertional oxygen uptake kinetics: a stamen of stamina?, Biochemical Society Transactions 30 (2) (2002) 237–247. doi:10.1042/bst0300237.

[36] Y. Seyama, H. Wachi, Atherosclerosis and matrix dystrophy., Journal of Atherosclerosis and Thrombosis 11 (5) (2004) 236–245. doi:10.5551/jat.11.236.

[37] C. M. Kielty, Elastic fibres in health and disease., Expert Reviews in Molecular Medicine 8 (19) (2006) 1–23. doi:10.1017/S146239940600007X.

[38] R. J. Wityk, C. Zanferrari, S. Oppenheimer, Neurovascular Complications of Marfan Syndrome, Stroke (2002) 680–684doi:10.1161/hs0302.103816.

[39] H. Weisbecker, C. Viertler, D. M. Pierce, G. A. Holzapfel, The role of elastin and collagen in the softening behavior of the human thoracic aortic media., Journal of Biomechanics 46 (11) (2013) 1859–65. doi:10.1016/j.jbiomech.2013.04.025.

[40] A. J. Schriefl, T. Schmidt, D. Balzani, G. Sommer, G. A. Holzapfel, Selective enzymatic removal of elastin and collagen from human abdominal aortas: Uniaxial mechanical response and constitutive modeling, Acta Biomaterialia 17 (2015) 125–136. doi:10.1016/j.actbio.2015.01.003.

[41] M.-J. Chow, J. R. Mondonedo, V. M. Johnson, Y. Zhang, Progressive structural and biomechanical changes in elastin degraded aorta., Biomechanics and Modeling in Mechanobiology 12 (2) (2013) 361–72. doi:10.1007/s10237-012-0404-9.

[42] N. Gundiah, A. R. Babu, L. A. Pruitt, Effects of elastase and collagenase on the nonlinearity and anisotropy of porcine aorta., Physiological Measurement 34 (12) (2013) 1657–73. doi:10.1088/0967-3334/34/12/1657.

[43] P. Kochová, J. Kuncová, J. Svíglerová, R. Cimrman, M. Miklíková, V. Liška, Z. Tonar, The contribution of vascular smooth muscle, elastin and collagen on the passive mechanics of porcine carotid arteries., Physiological Measurement 33 (8) (2012) 1335–51. doi:10.1088/0967-3334/33/8/1335.

[44] E. Fonck, G. Prod'hom, S. Roy, L. Augsburger, D. A. Rüfenacht, N. Stergiopulos, Effect of elastin degradation on carotid wall mechanics as assessed by a constituent-based biomechanical model., American Journal of Physiology. Heart and Circulatory Physiology 292 (6) (2007) 2754–63. doi:10.1152/ajpheart.01108.2006.

[45] L. Dadgar, Y. Marois, X. Deng, R. Guidoin, Arterial wall mechanical characteristics after treatment in collagenase: An in vitro aneurysm model, Clinical and Investigative Medicine 20 (1) (1997) 25–34.

[46] G. Sommer, T. C. Gasser, P. Regitnig, M. Auer, G. A. Holzapfel, Dissection properties of the human aortic media: an experimental study., Journal of Biomechanical Engineering 130 (2) (2008) 021007. doi:10.1115/1.2898733.

[47] W. Carson, M. R. Roach, The strength of the aortic media and its role in the propagation of aortic dissection, Journal of Biomechanics 3 (6) (1990) 579–588. doi:10.1016/0021-9290(90)90050-D.

[48] J. Tong, G. Sommer, P. Regitnig, G. A. Holzapfel, Dissection properties and mechanical strength of tissue components in human carotid bifurcations., Annals of Biomedical Engineering 39 (6) (2011) 1703–19. doi:10.1007/s10439-011-0264-y.

[49] M. R. Roach, S. H. Song, Variations in strength of the porcine aorta as a function of location, Clinical and Investigative Medicine 17 (4) (1994) 308–318.

[50] D. W. Dunning, J. K. Kahn, E. T. Hawkins, W. W. O'Neill, Iatrogenic coronary artery dissections extending into and involving the aortic root., Catheterization and Cardiovascular Interventions 51 (4) (2000) 387–93.

[51] S. Gómez-Moreno, M. Sabaté, P. Jiménez-Quevedo, P. Vázquez, F. Alfonso, D. J. Angiolillo, R. Hernández-Antolín, R. Moreno, C. Bañuelos, J. Escaned,

C. Macaya, Iatrogenic dissection of the ascending aorta following heart catheterisation: incidence, management and outcome., EuroIntervention 2 (2) (2006) 197–202.

[52] K. H. Dellimore, S. E. Franklin, A. R. Helyer, A Review of Catheter Related Complications During Minimally Invasive Transcatheter Cardiovascular Intervention with Implications for Catheter Design, Cardiovascular Engineering and Technology 5 (3) (2014) 217–232. doi:10.1007/s13239-014-0183-9.

[53] I. Stathopoulos, M. Jimenez, G. Panagopoulos, E. J. Kwak, M. Losquadro, H. Cohen, S. Iyer, C. Ruiz, G. Roubin, K. Garratt, The decline in PCI complication rate: 2003-2006 versus 1999-2002, Hellenic Journal of Cardiology 50 (5) (2009) 379–387.
URL http://www.ncbi.nlm.nih.gov/pubmed/19767279

[54] D. Jain, V. Kurowski, H. A. Katus, G. Richardt, Catheter-induced dissection of the left main coronary artery, the nemesis of an invasive cardiologist A case report and review of the literature., Zeitschrift für Kardiologie 91 (10) (2002) 840–5. doi:10.1007/s00392-002-0823-1.

[55] M. Fiddler, S. A. Avadhani, J. D. Marmur, Guide Catheter-Induced Aortic Dissection Complicated by Pericardial Effusion with Pulsus Paradoxus: A Case Report of Successful Medical Management, Case Reports in Medicine 2015 (2015) 1–6. doi:10.1155/2015/480242.

[56] I. M. Tiessen, M. R. Roach, Factors in the initiation and propagation of aortic dissections in human autopsy aortas., Journal of Biomechanical Engineering 115 (1) (1993) 123–125.

[57] J. Tong, T. Cohnert, P. Regitnig, J. Kohlbacher, R. Birner-Gruenberger, A. J. Schriefl, G. Sommer, G. A. Holzapfel, Variations of dissection properties and mass fractions with thrombus age in human abdominal aortic aneurysms., Journal of Biomechanics 47 (1) (2014) 14–23. doi:10.1016/j.jbiomech.2013.10.027.

[58] S. Pasta, J. A. Phillippi, T. G. Gleason, D. A. Vorp, Effect of aneurysm on the mechanical dissection properties of the human ascending thoracic aorta., The Journal of Thoracic and Cardiovascular Surgery 143 (2) (2012) 460–7. doi:10.1016/j.jtcvs.2011.07.058.

[59] T. C. Gasser, G. A. Holzapfel, Modeling the propagation of arterial dissection, European Journal of Mechanics - A/Solids 25 (4) (2006) 617–633. doi:10.1016/j.euromechsol.2006.05.004.

[60] A. Ferrara, A. Pandolfi, A numerical study of arterial media dissection processes, International Journal of Fracture 166 (1-2) (2010) 21–33. doi:10.1007/s10704-010-9480-y.

[61] S. Misra, K. B. Reed, A. S. Douglas, K. T. Ramesh, A. M. Okamura, Needle-Tissue Interaction Forces for Bevel-Tip Steerable Needles., Proceedings of the 2nd Biennial IEEE/RAS-EMBS International Conference on Biomedical Robotics and Biomechatronics (2008) 224–231doi:10.1109/BIOROB.2008.4762872.

[62] C. Forsell, T. C. Gasser, Numerical simulation of the failure of ventricular tissue due to deep penetration: the impact of constitutive properties., Journal of Biomechanics 44 (1) (2011) 45–51. doi:10.1016/j.jbiomech.2010.08.022.

[63] M. Oldfield, D. Dini, G. Giordano, F. Rodriguez y Baena, Detailed finite element modelling of deep needle insertions into a soft tissue phantom using a cohesive approach, Computer Methods in Biomechanics and Biomedical Engineering 16 (5) (2013) 530–543. doi:10.1080/10255842.2011.628448.

[64] R. A. Tomlinson, Z. A. Taylor, Photoelastic materials and methods for tissue biomechanics applications, Optical Engineering 54 (8) (2015) 81208. doi:10.1117/1.OE.54.8.081208.

[65] C. Noble, N. Smulders, N. H. Green, R. Lewis, M. J. Carré, S. E. Franklin, S. MacNeil, Z. A. Taylor, Creating a model of diseased artery damage and failure from healthy porcine aorta, Journal of the Mechanical Behavior of Biomedical Materials 60 (2016) 378–393. doi:10.1016/j.jmbbm.2016.02.018.

[66] C. Noble, N. Smulders, R. Lewis, M. J. Carré, S. E. Franklin, S. MacNeil, Z. A. Taylor, Controlled peel testing of a model tissue for diseased aorta, Journal of Biomechanics 49 (15) (2016) 3667–3675. doi:10.1016/j.jbiomech.2016.09.040.

[67] C. Noble, O. van der Sluis, R. M. Voncken, O. Burke, S. E. Franklin, R. Lewis, Z. A. Taylor, Simulation of arterial dissection by a penetrating external body using cohesive zone modelling, Journal of the Mechanical Behavior of Biomedical Materials (Submitted).

[68] P. F. Gratzer, J. M. Lee, Altered mechanical properties in aortic elastic tissue using glutaraldehyde/solvent solutions of various dielectric constant., Journal of Biomedical Materials Research 37 (4) (1997) 497–507.

[69] M. Sawabe, Vascular aging: from molecular mechanism to clinical significance., Geriatrics and Gerontology International 10 Suppl 1 (2010) 213–20. doi:10.1111/j.1447-0594.2010.00603.x.

[70] T. C. Gasser, R. W. Ogden, G. A. Holzapfel, Hyperelastic modelling of arterial layers with distributed collagen fibre orientations., Journal of the Royal Society, Interface / the Royal Society 3 (6) (2006) 15–35. doi:10.1098/rsif.2005.0073.

[71] B. Calvo, E. Peña, M. A. Martinez, M. Doblaré, An uncoupled directional damage model for fibred biological soft tissues. Formulation and computational aspects, International Journal for Numerical Methods in Engineering 69 (10) (2007) 2036–2057. doi:10.1002/nme.1825.

[72] V. Alastrué, J. Rodríguez, B. Calvo, M. Doblaré, Structural damage models for fibrous biological soft tissues, International Journal of Solids and Structures 44 (18-19) (2007) 5894–5911. doi:10.1016/j.ijsolstr.2007.02.004.

[73] H. W. Haslach, L. N. Leahy, P. Fathi, J. M. Barrett, A. E. Heyes, T. A. Dumsha, E. L. McMahon, Crack Propagation and Its Shear Mechanisms in the Bovine Descending Aorta, Cardiovascular Engineering and Technology 6 (4) (2015) 501–518. doi:10.1007/s13239-015-0245-7.

[74] D. J. Patel, J. S. Janicki, R. N. Vaishnav, J. T. Young, Dynamic Anisotropic Viscoelastic Properties of the Aorta in Living Dogs, Circulation Research 32 (1) (1973) 93–107. doi:10.1161/01.RES.32.1.93.

[75] M. D. Dooldeniya, A. N. Warrens, Xenotransplantation: where are we today?, Journal of the Royal Society of Medicine 96 (3) (2003) 111–7.

[76] G. A. Holzapfel, Determination of material models for arterial walls from uniaxial extension tests and histological structure., Journal of Theoretical Biology 238 (2) (2006) 290–302. doi:10.1016/j.jtbi.2005.05.006.

[77] M. T. Walsh, E. M. Cunnane, J. J. Mulvihill, A. C. Akyildiz, F. J. H. Gijsen, G. A. Holzapfel, Uniaxial tensile testing approaches for characterisation of atherosclerotic plaques, Journal of Biomechanics 47 (4) (2014) 793–804. doi:10.1016/j.jbiomech.2014.01.017.

[78] R. H. Cox, Passive mechanics and connective tissue composition of canine arteries., The American Journal of Physiology 234 (5) (1978) H533–H541.

[79] G. A. Holzapfel, T. C. Gasser, R. W. Ogden, A new constitutive framework for arterial wall mechanics and a comparative study of material models, Journal of Elasticity 61 (1-3) (2000) 1–48. doi:10.1023/A:1010835316564.

[80] H. Weisbecker, D. M. Pierce, P. Regitnig, G. A. Holzapfel, Layer-specific damage experiments and modeling of human thoracic and abdominal aortas with non-atherosclerotic intimal thickening., Journal of the Mechanical Behavior of Biomedical Materials 12 (2012) 93–106. doi:10.1016/j.jmbbm.2012.03.012.

[81] G. A. Holzapfel, Nonlinear solid mechanics: a continuum approach for engineering, Vol. 24, John Wiley & Sons, Ltd., 2000.

[82] J. Simo, On a fully three-dimensional finite-strain viscoelastic damage model: Formulation and computational aspects, Computer Methods in Applied Mechanics and Engineering 60 (2) (1987) 153–173. doi:10.1016/0045-7825(87)90107-1.

[83] E. Peña, B. Calvo, M. A. Martínez, M. Doblaré, On finite-strain damage of viscoelastic-fibred materials. Application to soft biological tissues, International Journal for Numerical Methods in Engineering 74 (7) (2008) 1198–1218. doi:10.1002/nme.2212.

[84] D. Robertson, D. Cook, Unrealistic statistics: How average constitutive coefficients can produce non-physical results, Journal of the Mechanical Behavior of Biomedical Materials 40 (2014) 234–239. doi:10.1016/j.jmbbm.2014.09.006.

[85] J. Kennedy, R. Eberhart, Particle swarm optimization, Neural Networks, 1995. Proceedings., IEEE International Conference on 4 (1995) 1942–1948. doi:10.1109/ICNN.1995.488968.

[86] R. W. Ogden, G. Saccomandi, I. Sgura, Fitting hyperelastic models to experimental data, Computational Mechanics 34 (6) (2004) 484–502. doi:10.1007/s00466-004-0593-y.

[87] H. Fehervary, M. Smoljkić, J. Vander Sloten, N. Famaey, Planar biaxial testing of soft biological tissue using rakes: A critical analysis of protocol and fitting process, Journal of the Mechanical Behavior of Biomedical Materials 61 (2016) 135–151. doi:10.1016/j.jmbbm.2016.01.011.

[88] G. A. Holzapfel, R. W. Ogden, Constitutive modelling of arteries, Proceedings of the Royal Society A: Mathematical, Physical and Engineering Sciences 466 (2118) (2010) 1551–1597. doi:10.1098/rspa.2010.0058.

[89] Y. C. Fung, K. Fronek, P. Patitucci, Pseudoelasticity of arteries and the choice of its mathematical expression., The American Journal of Physiology 237 (5) (1979) H620–H631.

[90] B. D. Stemper, N. Yoganandan, M. R. Stineman, T. A. Gennarelli, J. L. Baisden, F. A. Pintar, Mechanics of Fresh, Refrigerated, and Frozen Arterial Tissue, Journal of Surgical Research 139 (2) (2007) 236–242. doi:10.1016/j.jss.2006.09.001.

[91] B. D. Stemper, N. Yoganandan, F. A. Pintar, Mechanics of arterial subfailure with increasing loading rate, Journal of Biomechanics 40 (8) (2007) 1806–1812. doi:10.1016/j.jbiomech.2006.07.005.

[92] D. Mohan, J. W. Melvin, Failure properties of passive human aortic tissue. I–uniaxial tension tests., Journal of Biomechanics 15 (11) (1982) 887–902. doi:10.1016/0021-9290(83)90044-1.

[93] R. Collins, W. C. Hu, Dynamic deformation experiments on aortic tissue., Journal of Biomechanics 5 (4) (1972) 333–337. doi:10.1016/0021-9290(72)90062-0.

[94] J. A. Peña, M. A. Martínez, E. Peña, Layer-specific residual deformations and uniaxial and biaxial mechanical properties of thoracic porcine aorta, Journal of the Mechanical Behavior of Biomedical Materials 50 (2015) 55–69. doi:10.1016/j.jmbbm.2015.05.024.

[95] H. D. Intengan, G. Thibault, J. S. Li, E. L. Schiffrin, Resistance artery mechanics, structure, and extracellular components in spontaneously hypertensive rats : effects of angiotensin receptor antagonism and converting enzyme inhibition., Circulation 100 (22) (1999) 2267–2275. doi:10.1161/01.CIR.100.22.2267.

[96] P. B. Dobrin, T. R. Canfield, Elastase, collagenase, and the biaxial elastic properties of dog carotid artery., The American Journal of Physiology 247 (1 Pt 2) (1984) H124–H131.

[97] P. B. Dobrin, W. C. Gley, Elastase, collagenase and the radial elastic properties of arteries., Experientia 41 (8) (1985) 1040–1042. doi:10.1007/BF01952132.

[98] M. J. Collins, J. F. Eberth, E. Wilson, J. D. Humphrey, Acute mechanical effects of elastase on the infrarenal mouse aorta: implications for models of aneurysms., Journal of Biomechanics 45 (4) (2012) 660–5. doi:10.1016/j.jbiomech.2011.12.013.

[99] P. Lacolley, P. Boutouyrie, M. Glukhova, J.-M. Daniel Lamaziere, P.-F. Plouin, P. Bruneval, P. Vuong, P. Corvol, S. Laurent, Disruption of the elastin gene in adult Williams syndrome is accompanied by a paradoxical reduction in arterial stiffness., Clinical Science 103 (1) (2002) 21–29. doi:10.1042/CS20010287.

[100] S. Avrameas, Coupling of enzymes to proteins with glutaraldehyde. Use of the conjugates for the detection of antigens and antibodies., Immunochemistry 6 (1) (1969) 43–52. doi:10.1016/0019-2791(69)90177-3.

[101] S. Avrameas, T. Ternynck, The cross-linking of proteins with glutaraldehyde and its use for the preparation of immunoadsorbents., Immunochemistry 6 (1) (1969) 53–66. doi:10.1016/0019-2791(69)90178-5.

[102] E. M. McDowell, B. F. Trump, Histologic fixatives suitable for diagnostic light and electron microscopy., Archives of Pathology & Laboratory Medicine 100 (8) (1976) 405–414.

[103] G. J. L'Italien, J. Megerman, J. E. Hasson, A. E. Meyer, R. E. Baier, W. M. Abbott, Compliance changes in glutaraldehyde-treated arteries., The Journal of Surgical Research 41 (2) (1986) 182–188. doi:10.1016/0022-4804(86)90023-5.

[104] H. W. Sung, C. S. Hsu, Y. S. Lee, Physical properties of a porcine internal thoracic artery fixed with an epoxy compound, Biomaterials 17 (24) (1996) 2357–2365. doi:10.1016/S0142-9612(96)00081-6.

[105] C. M. He, M. R. Roach, The composition and mechanical properties of abdominal aortic aneurysms, Journal of Vascular Surgery 20 (1) (1994) 6–13. doi:10.1016/0741-5214(94)90169-4.

[106] M. L. Raghavan, M. M. Hanaoka, J. A. Kratzberg, M. de Lourdes Higuchi, E. S. da Silva, Biomechanical failure properties and microstructural content of ruptured and unruptured abdominal aortic aneurysms., Journal of Biomechanics 44 (13) (2011) 2501–7. doi:10.1016/j.jbiomech.2011.06.004.

[107] G. A. Holzapfel, G. Sommer, P. Regitnig, Anisotropic mechanical properties of tissue components in human atherosclerotic plaques., Journal of Biomechanical Engineering 126 (5) (2004) 657–665. doi:10.1115/1.1800557.

[108] Z. Teng, D. Tang, J. Zheng, P. K. Woodard, A. H. Hoffman, An experimental study on the ultimate strength of the adventitia and media of human atherosclerotic carotid arteries in circumferential and axial directions, Journal of Biomechanics 42 (15) (2009) 2535–2539. doi:10.1016/j.jbiomech.2009.07.009.

[109] H. M. Loree, A. J. Grodzinsky, S. Y. Park, L. J. Gibson, R. T. Lee, Static circumferential tangential modulus of human atherosclerotic tissue, Journal of Biomechanics 27 (2) (1994) 195–204. doi:10.1016/0021-9290(94)90209-7.

[110] M. S. Sacks, Biaxial mechanical evaluation of planar biological materials, Journal of Elasticity 61 (1-3) (2000) 199–246. doi:10.1023/A:1010917028671.

[111] J. P. Vande Geest, M. S. Sacks, D. A. Vorp, Age dependency of the biaxial biomechanical behavior of human abdominal aorta., Journal of Biomechanical Engineering 126 (6) (2004) 815–822. doi:10.1115/1.1824121.

[112] W. Sun, M. S. Sacks, M. J. Scott, Effects of boundary conditions on the estimation of the planar biaxial mechanical properties of soft tissues., Journal of Biomechanical Engineering 127 (4) (2005) 709–715. doi:10.1115/1.1933931.

[113] S. D. Waldman, J. Michael Lee, Boundary conditions during biaxial testing of planar connective tissues. Part 1: Dynamic behavior, Journal of Materials Science: Materials in Medicine 13 (10) (2002) 933–938. doi:10.1023/A:1019896210320.

[114] E. A. Stephen, A. Venkatasubramaniam, T. A. Good, L. D. T. Topoleski, The effect of glycation on arterial microstructure and mechanical response., Journal of Biomedical Materials Research. Part A 102 (8) (2014) 2565–72. doi:10.1002/jbm.a.34927.

[115] K. Hayashi, Y. Imai, Tensile property of atheromatous plaque and an analysis of stress in atherosclerotic wall, Journal of Biomechanics 30 (6) (1997) 573–579. doi:10.1016/S0021-9290(96)00185-6.

[116] G. S. Getz, C. A. Reardon, Animal Models of Atherosclerosis, Arteriosclerosis, Thrombosis, and Vascular Biology 32 (5) (2012) 1104–1115. doi:10.1161/ATVBAHA.111.237693.Animal.

[117] C. E. Anagnostopoulos, M. J. Prabhakar, C. F. Kittle, Aortic dissections and dissecting aneurysms, The American Journal of Cardiology 30 (3) (1972) 263–273. doi:10.1016/0002-9149(72)90070-7.

[118] D. M. Milewicz, H. Dietz, C. Miller, Treatment of Aortic Disease in Patients With Marfan Syndrome, Circulation 111 (11) (2005) e150–e157. doi:10.1161/01.CIR.0000155243.70456.F4.

[119] D. Ulbricht, N. J. Diederich, T. Hermanns-Lê, R. J. Metz, F. Macian, G. E. Piérard, Cervical artery dissection: An atypical presentation with Ehlers-Danlos-like collagen pathology?, Neurology 63 (9) (2004) 1708–1710. doi:10.1212/01.WNL.0000142970.09454.30.

[120] J. Z. Goldfinger, J. L. Halperin, M. L. Marin, A. S. Stewart, K. A. Eagle, V. Fuster, Thoracic Aortic Aneurysm and Dissection, Journal of the American College of Cardiology 64 (16) (2014) 1725–1739. doi:10.1016/j.jacc.2014.08.025.

[121] J. Bonnet, M. Aumailley, D. Thomas, Y. Grosgogeat, J. P. Broustet, H. Bricaud, Spontaneous coronary artery dissection: case report and evidence for a defect in collagen metabolism., European Heart Journal 7 (10) (1986) 904–9.

[122] H. P. Adams Jr., C. A. Aschenbrener, N. F. Kassell, L. Ansbacher, S. H. Cornell, Intracranial hemorrhage produced by spontaneous dissecting intracranial aneurysm, Archives of Neurology 39 (12) (1982) 773–776.

[123] L. de Figueiredo Borges, R. G. Jaldin, R. R. Dias, N. A. G. Stolf, J.-B. Michel, P. S. Gutierrez, Collagen is reduced and disrupted in human aneurysms and dissections of ascending aorta, Human Pathology 39 (3) (2008) 437–443. doi:10.1016/j.humpath.2007.08.003.

[124] G. Sommer, S. Sherifova, P. J. Oberwalder, O. E. Dapunt, P. A. Ursomanno, A. DeAnda, B. E. Griffith, G. A. Holzapfel, Mechanical strength of aneurysmatic

and dissected human thoracic aortas at different shear loading modes, Journal of Biomechanicsdoi:10.1016/j.jbiomech.2016.02.042.

[125] A. E. Hirst, V. J. Johns, Experimental Disection of Media of Aorta by Pressure: Its Relation to Spontanous Dissecting Aneurysm, Circulation Research 10 (1962) 897–903.

[126] S. Pal, A. Tsamis, S. Pasta, A. D'Amore, T. G. Gleason, D. A. Vorp, S. Maiti, A mechanistic model on the role of "radially-running" collagen fibers on dissection properties of human ascending thoracic aorta, Journal of Biomechanics 47 (5) (2014) 981–988. doi:10.1016/j.jbiomech.2014.01.005.

[127] C. van Baardwijk, M. R. Roach, Factors in the propagation of aortic dissections in canine thoracic aortas, Journal of Biomechanics 20 (1) (1987) 67–73. doi:10.1016/0021-9290(87)90268-5.

[128] S. Zeinali-Davarani, M.-J. Chow, R. Turcotte, Y. Zhang, Characterization of biaxial mechanical behavior of porcine aorta under gradual elastin degradation., Annals of Biomedical Engineering 41 (7) (2013) 1528–38. doi:10.1007/s10439-012-0733-y.

[129] Y. Wang, J. A. Johnson, F. G. Spinale, M. A. Sutton, S. M. Lessner, Quantitative Measurement of Dissection Resistance in Intimal and Medial Layers of Human Coronary Arteries., Experimental Mechanics 54 (4) (2014) 677–683. doi:10.1007/s11340-013-9836-0.

[130] K. P. Dingemans, P. Teeling, J. H. Lagendijk, A. E. Becker, Extracellular matrix of the human aortic media: An ultrastructural histochemical and immunohistochemical study of the adult aortic media, The Anatomical Record 258 (1) (2000) 1–14.

[131] M. K. O'Connell, S. Murthy, S. Phan, C. Xu, J. Buchanan, R. Spilker, R. L. Dalman, C. K. Zarins, W. Denk, C. A. Taylor, The three-dimensional micro- and nanostructure of the aortic medial lamellar unit measured using 3D confocal and electron microscopy imaging., Matrix Biology 27 (3) (2008) 171–81. doi:10.1016/j.matbio.2007.10.008.

[132] L. H. H. O. Damink, P. J. Dijkstra, M. J. A. Van Luyn, P. B. Van Wachem, P. Nieuwenhuis, J. Feijen, Glutaraldehyde as a crosslinking agent for collagen-based biomaterials, Journal of Materials Science: Materials in Medicine 6 (8) (1995) 460–472. doi:10.1007/BF00123371.

[133] L. A. Hapach, J. A. VanderBurgh, J. P. Miller, C. A. Reinhart-King, Manipulation of in vitro collagen matrix architecture for scaffolds of improved physiolo-

gical relevance, Physical Biology 12 (6) (2015) 061002. doi:10.1088/1478-3975/12/6/061002.

[134] F. Luo, X.-L. Zhou, J.-J. Li, R.-T. Hui, Inflammatory response is associated with aortic dissection., Ageing Research Reviews 8 (1) (2009) 31–35. doi:10.1016/j.arr.2008.08.001.

[135] D.-C. Guo, H. Pannu, V. Tran-Fadulu, C. L. Papke, R. K. Yu, N. Avidan, S. Bourgeois, A. L. Estrera, H. J. Safi, E. Sparks, D. Amor, L. Ades, V. McConnell, C. E. Willoughby, D. Abuelo, M. Willing, R. A. Lewis, D. H. Kim, S. Scherer, P. P. Tung, C. Ahn, L. M. Buja, C. S. Raman, S. S. Shete, D. M. Milewicz, Mutations in smooth muscle alpha-actin (ACTA2) lead to thoracic aortic aneurysms and dissections., Nature Genetics 39 (12) (2007) 1488–1493. doi:10.1038/ng.2007.6.

[136] G. Marano, M. Grigioni, S. Palazzesi, A. U. Ferrari, Endothelin and mechanical properties of the carotid artery in Wistar-Kyoto and spontaneously hypertensive rats., Cardiovascular Research 41 (3) (1999) 701–7.

[137] A. Tsamis, J. A. Phillippi, R. G. Koch, S. Pasta, A. D'Amore, S. C. Watkins, W. R. Wagner, T. G. Gleason, D. A. Vorp, Fiber micro-architecture in the longitudinal-radial and circumferential-radial planes of ascending thoracic aortic aneurysm media, Journal of Biomechanics 46 (16) (2013) 2787–2794. doi:10.1016/j.jbiomech.2013.09.003.

[138] Q. Hernández, E. Peña, Failure properties of vena cava tissue due to deep penetration during filter insertion, Biomechanics and Modeling in Mechanobiology 15 (4) (2016) 845–856. doi:10.1007/s10237-015-0728-3.

[139] Y. C. Fung, Biomechanics : mechanical properties of living tissues, Springer-Verlag, New York, 1981.

[140] R. de Borst, M. A. Crisfield, J. J. Remmers, C. V. Verhoosel, Non-linear Finite Element Analysis of Solids and Structures, John Wiley & Sons, Ltd., 2012. doi:10.1002/9781118375938.

[141] A. Ferrara, A. Pandolfi, Numerical modelling of fracture in human arteries., Computer Methods in Biomechanics and Biomedical Engineering 11 (5) (2008) 553–67. doi:10.1080/10255840701771743.

[142] T. C. Gasser, G. A. Holzapfel, Modeling plaque fissuring and dissection during balloon angioplasty intervention., Annals of Biomedical Engineering 35 (5) (2007) 711–23. doi:10.1007/s10439-007-9258-1.

[143] K. Takashima, R. Shimomura, T. Kitou, H. Terada, K. Yoshinaka, K. Ikeuchi, Contact and friction between catheter and blood vessel, Tribology International 40 (2) (2007) 319–328. doi:10.1016/j.triboint.2005.10.010.

[144] M. J. van den Bosch, P. J. G. Schreurs, M. G. D. Geers, On the development of a 3D cohesive zone element in the presence of large deformations, Computational Mechanics 42 (2) (2007) 171–180. doi:10.1007/s00466-007-0184-8.

[145] S. X. Deng, J. Tomioka, J. C. Debes, Y. C. Fung, New experiments on shear modulus of elasticity of arteries., The American Journal of Physiology 266 (1 Pt 2) (1994) 1–10. doi:10.1186/1471-2350-12-51.

[146] M. Couade, M. Pernot, C. Prada, E. Messas, J. Emmerich, P. Bruneval, A. Criton, M. Fink, M. Tanter, Quantitative assessment of arterial wall biomechanical properties using shear wave imaging., Ultrasound in Medicine & Biology 36 (10) (2010) 1662–76. doi:10.1016/j.ultrasmedbio.2010.07.004.

[147] E. Messas, M. Pernot, M. Couade, Arterial wall elasticity: State of the art and future prospects, Diagnostic and Interventional Imaging 94 (5) (2013) 561–569. doi:10.1016/j.diii.2013.01.025.

[148] P. F. Ludman, L. Gavalova, National Audit of Percutaneous Coronary Interventions Annual Report (2014).
URL `http://www.ucl.ac.uk/nicor/audits/adultpercutaneous/documents/2014-an`

[149] R. W. Ogden, Large Deformation Isotropic Elasticity: On the Correlation of Theory and Experiment for Compressible Rubberlike Solids, Proceedings of the Royal Society of London A: Mathematical, Physical and Engineering Sciences 328 (1575) (1972) 567–583. doi:10.1098/rspa.1972.0096.

[150] O. van der Sluis, Y. Y. Hsu, P. H. M. Timmermans, M. Gonzalez, J. P. M. Hoefnagels, Stretching-induced interconnect delamination in stretchable electronic circuits, Journal of Physics D: Applied Physics 44 (3) (2011) 034008. doi:10.1088/0022-3727/44/3/034008.

[151] M. Pagani, U. Perego, Explicit dynamics simulation of blade cutting of thin elastoplastic shells using "directional" cohesive elements in solid-shell finite element models, Computer Methods in Applied Mechanics and Engineering 285 (2015) 515–541. doi:10.1016/j.cma.2014.11.027.

[152] B. G. Vossen, O. van der Sluis, P. J. G. Schreurs, M. G. D. Geers, High toughness fibrillating metal-elastomer interfaces: On the role of discrete fibrils within the fracture process zone, Engineering Fracture Mechanics 164 (2016) 93–105. doi:10.1016/j.engfracmech.2016.05.019.
URL `http://dx.doi.org/10.1016/j.engfracmech.2016.05.019`

[153] G. R. Liu, T. T. Nguyen, Smoothed Finite Element Methods, CRC Press, 2010.